Numerical investigation of uncertainties in experiments for flame structure analysis and particle synthesis

Von der Fakultät für Ingenieurwissenschaften, Abteilung Maschinenbau und Verfahrenstechnik

der

Universität Duisburg-Essen

zur Erlangung des akademischen Grades

eines

Doktors der Ingenieurwissenschaften

Dr.-Ing.

genehmigte Dissertation

von

Lei Deng
aus
Anhui, China

Gutachter: Univ.-Prof. Dr.-Ing. Andreas Kempf
Univ.-Prof. Dr. Andreas Kronenburg
Tag der mündlichen Prüfung: 10.03.2017

Acknowledgments

The present work was carried out during my PhD studies at the chair of Fluid Dynamics, Institute for Combustion and Gas Dynamics at the University of Duisburg-Essen.

I would like to thank my supervisor Prof. Dr.-Ing. Andreas Kempf, for offering me the opportunity of a PhD under his supervision and his support throughout my whole PhD study whenever it was required. I am grateful for his always positive attitude towards my research and his encouragement to publish my work, to cooperate with other outstanding researchers over the world and to attend international conferences where I could present my work.

I wish to thank my team leader Dr.-Ing. Irenäus Wlokas for his thoughtful support during my five years at the chair of Fluid Dynamics. The discussions with him and many ideas from him contributed to the success of my work.

Further, I would like to thank all my research partners Dr.-Ing. Sebastian Kluge, Dr.-Ing. Omid Feroughi, Dr. Igor Rahinov and Yasin Karakaya, who provided the measurements for the validation of my simulation results. The productive discussions with them always inspired new ideas in my research work.

My appreciation goes to Prof. Dr. Oleg Korobeinichev, Prof. Dr. Christof Schulz, Prof. Dr. Hai Wang and Prof. Dr. Andreas Kronenburg for encouraging and inviting me to publish my work in international journals.

I would like to thank all my colleagues in the chair of Fluid Dynamics. It was my honor to work with them in such an open, friendly and pleasant environment. Special thanks to Hossein Janbazi, Timo Lipkowicz, Thuong Minh Nguyen, Patrick Wollny, Johannes Sellmann and Nejra Sikalo for proof reading of my thesis.

At last but not least, I wish to thank my wife Feng Shuo, the past eight years with her in Germany was a wonderful journey in my life.

Contents

List of Tables

List of Figures

Nomenclature

Acronyms

AMO	acousto-optic modulator
BD	blended differencing
BSS	burner stabilized stagnation
CD	central differencing
CFD	computational fluid dynamics
CSP	computational singular perturbation
ENO	essentially non-oscillatory
FCT	flux corrected transport
GDE	general dynamics equation
HAB	height above burner
ICLAS	intra-cavity laser absorption spectroscopy
ILDM	intrinsic low-dimensional manifold method
MPI	message passing interface
NVA	normalized variable approach
ODE	ordinary differential equation
PCA	principal component analysis
PISO	pressure implicit with splitting of operators
PMS	particle mass spectrometry
PSDF	particle size distribution function
QSSA	quasi-steady state assumption
SIMPLE	semi-implicit method for pressure linked equations
SMPS	scanning mobility particle sizer
TVD	total variation diminishing
UD	upwind differencing

Greek Symbols

α	thermal diffusivity	m^2/s
β	collision frequency	$1/\mathrm{s}$
$\boldsymbol{n}_f$	face normal	–
χ	chemical symbol	–
χ	size-splitting operator	–
γ	surface free energy	J/m^2
λ	thermal conductivity	$\mathrm{W}\cdot\mathrm{K}/\mathrm{m}$
μ	dynamic viscosity	$\mathrm{Pa}\cdot\mathrm{s}$
ν_r	stoichiometric coefficient	–
Ω_{ij}	collision integral	–
$\overline{\Phi}$	mean value of generic quantity	–
Φ	generic quantity	–
ϕ	correction factor	–
Φ_f	value saved on the surface	–
Φ_M	value saved in the midpoint of cell	–
ρ_p	particle density	kg/m^3
σ_{ij}	mean collision diameter	m
τ	stress tensor	N/m^2
θ	contact angle	$^\circ$

Roman Symbols

β	temperature exponent	–
$\boldsymbol{c}$	particle velocity	m/s
$\boldsymbol{g}$	gravitational acceleration	m/s^2
$\boldsymbol{I}$	identity tensor	–
$\boldsymbol{u}$	velocity vector	m/s
$\boldsymbol{V}$	diffusion velocity	m/s
$\boldsymbol{V}_c$	correction velocity	m/s
$\dot{Q}$	volumetric heat release rate due to external effect	$\mathrm{J}/\mathrm{s}/\mathrm{m}^3$
$\dot{w}$	volumetric reaction rate	$\mathrm{kg}/\mathrm{s}/\mathrm{m}^3$
$\dot{w}_T$	volumetric heat release rate due to combustion	$\mathrm{J}/\mathrm{s}/\mathrm{m}^3$
ρ	density	kg/m^3

τ_c	chemical time scale	s
τ_f	flow time scale	s
τ_s	characteristic time	s
A	frequency factor	1/s
A	total parameter surface area concentration	1/m
a	surface area	m^2
a_0	monomer surface area	m^2
a_s	minimum aggregate surface area	m^2
C_c	slip correction factor	–
c_p	specific heat capacity at constant pressure	$J/(kg \cdot K)$
d_a	aggregate diameter	m
d_c	collision diameter	m
D_f	fractal dimension	–
D_p	particle diffusion coefficient	m^2/s
d_p	primary particle diameter	m
D_{ij}	binary diffusion coefficient	m^2/s
D_{mi}	diffusion coefficient	m^2/s
Da	Damköhler number	–
E	activation energy	J/mol
F	mass flux through the face	kg/s
G	Gibbs energy	J
G_f°	Gibbs energy of formation under standard condition	J
G_v	bulk free energy	J/m^3
h	specific total enthalpy	J/kg
H°	enthalpy of formation	J
h_s	specific sensible enthalpy	J/kg
k_B	Boltzmann constant	$m^2kg/s/K$
K_c	equilibrium constant	–
k_f	reaction coefficient for forward reaction of order n	$mol^{1-n}L^{n-1}/s$
K_n	Knudsen number	–
k_r	reaction coefficient for backward reaction of order n	$mol^{1-n}L^{n-1}/s$
l	mean free path of particle	m

m	mass	kg
m_p	particle mass	m
N	total particle number concentration	$1/m^3$
n	total number of particle	–
N_A	Avogadro's number	1/mol
p	pressure	Pa
R	universal gas constant	J/mol/K
r	particle radius	m
r_c	collision radius	m
r_p	particle radius	m
r_s	neck radius	m
S	supersaturation ratio	–
S°	entropy of formation	J/K
T	temperature	K
t	time	s
T_a	activation temperature	K
V	total parameter volume concentration	–
v	partial volume	m^3
v_0	monomer volume	m^3
v_a	aggregate volume	m^3
v_m	molar volume	m^3/mol
W	molecular mass	kg/kmol
X	mole fraction	–
Y	mass fraction	–

Chapter 1

Introduction

Combustion is one of the oldest technologies for human beings to obtain energy in the form of heat. Nowadays, combustion of fossil- and biomass fuels provides nearly 80% of the global energy supply and still will be the main method for conversion of energy in the foreseeable future [1]. Since the fossil fuel resources are limited and the emissions of combustion contribute greatly to environmental pollution, scientists are motivated to study the process of combustion in order to improve the efficiency and to reduce pollutant formation. Beside the aspect of energy conversion, combustion is used in many processes of particulate material synthesis - since ancient times for synthesis of soot for ink pigments [2], nowadays well known as carbon black. In the recent past combustion became an important synthesis route for metal-oxide nanoparticles with a wide range of applications. Materials made via the flame-assisted synthesis route are typically thin solid films from chemical vapor deposition (CVD) [3] or particles of nanosize structure with diameters below 100 nm. Nanomaterials are highly interesting for many applications due to their unique physical and chemical properties. Their melting temperature, optical or magnetic properties and the catalytic efficiency are strongly affected by their size and often differ from properties of the bulk material [4]. The applications of nanoparticles include optical magnetic recording [5], magnetic resonance imaging [6], gas sensors [7], catalysis [8], biolabeling and bioseperation [9, 10]. Furthermore, the particles can be used for creation of bulk devices with desired microscopic structures for optimized physical properties [11]. Gas phase synthesis of particles for technical scales can be realized in flow reactors, where the energy is supplied by wall-heating, plasma-heating or by combustion, while the combustion route is of highest relevance due to its efficiency and robustness. Nanoparticles produced at highly industrial scales are carbon black, titania pigments and fumed silica - all of them from combustion processes, with great purity and at high production rates. The process itself follows always a similar path. The dopant (e.g. compounds of metal) in gaseous or liquid state (in following referred to as precursor) is burned directly or added into the fuel. The high temperature in the flame environment drives the decomposition of the precursor, which is followed by the chemical reaction between the precursor-decomposition products and the flame intermediate species into the vapor of particle monomer molecules. When subsequently the temperature drops, the su-

persaturation causes formation of nuclei or clusters, followed by growth to nanoparticles due to coagulation and coalescence.

The combustion itself is basically a sequence of elementary chemical reactions with heat release by transforming the fuel and oxidizer into combustion products. Knowledge of the involved chemical reactions is essential for modeling of many effects of the combustion, such as flame ignition, flame quenching, pollutant formation and heat release. In all technical flames the thermochemical process is coupled with complex fluid mechanical phenomena, such as turbulence and strong buoyancy, which increase the difficulties in the fundamental study of the reactions. Therefore, laboratory-scale flames and experiments are designed such that the dimensionality of the flow problem is reduced and fluid mechanical effects are minimized. Thus, a widely used experimental setup is the premixed, laminar flat flame [12], stabilized either at the cooled burner matrix (burner stabilized) [13, 14] or a cooled plate placed downstream (stagnation-point stabilized) [15]. The flat flames are operated at atmospheric pressure, or in order to increase the spatial resolution of the measurements, at low-pressures. Well-defined conditions of such flames with respect to the flow field, temperature profile, gas concentration, as well as spatial uniformity are advantages for the measurement and numerical modeling. Concentrations of the combustion intermediates can be measured as a function of height above the burner (HAB), which are the input for the validation and optimization of reaction mechanisms [16]. All these properties of flat flames make them an attractive tool for the investigation of particle producing flames. The lack of a comprehensive understanding of the reaction kinetics in the combustion of nanoparticle precursors is the driving force for laboratory-scale investigations. Premixed flat flames doped with the precursor within a well-controlled reactor provide a variety of adjustable operating conditions in terms of temperature, pressure and precursor concentration and are therefore suitable for the investigation of particle synthesis [17, 18].

The flat flame is assumed to be steady and one-dimensional. The set of conservation equations describing the reacting flow can be reduced into a set of ordinary differential equations and very efficient numerical solution methods can be employed. Unfortunately, the assumption of a one-dimensional, ideal flow is strongly violated by reactor housing, buoyancy and invasive diagnostic techniques. Diagnostic techniques for the combustion characterization can be classified in two groups: optical techniques and probe techniques. Optical techniques are non-intrusive techniques with high temporal and spatial resolution, and can simultaneously measure in many points. Widely used techniques for the measurement of flow field are laser Doppler and particle imaging velocimetry (PIV) [19], whereas temperature and species concentration can be measured by laser-induced fluorescence (LIF) [20] and Rayleigh scattering [21]. However, they are mostly expensive and have difficulties to yield quantitative data. In addition to optical techniques, probe techniques are also extensively used in combustion research. Among them, molecular beam sampling is an attractive technique for the capture of gas samples along the flame centerline. Normally, a molecular beam can be formed by the traveling of the samples through the sampling nozzle and the rapid gas expansion to a low pressure (10^{-3} mbar), thereby quenching the reactions. For the study of flame structure, the molecular beam technique followed by a mass analyzer and a detector is widely used

due to its high sensitivity, great spatial resolution and ability to detect nearly all radicals of the reacting gas simultaneously. However, this technique is intrusive and strongly affects the flame. The probe nozzle, typically a quartz cone with an orifice at the tip, can distort the flame thermodynamically and aerodynamically, resulting in a geometric modification of the flame structure [22, 23]. The same issue arises for the molecular beam technique in combination with particle mass spectrometry in the measurement of clusters at low height above the burner [12]. These effects induced by the sampling nozzle cause the significant deviation of the measurements from the 1-D ideal modeling results. In addition to the probing effect, other thermodynamical and fluid dynamic effects, like buoyancy [24] or heat loss of the flame due to the presence of reactor housing [25] can also influence the measurements and lead to uncertainties in the experimental results.

The present work investigates experiments in laminar, premixed particle producing flames at atmospheric or at low pressure in a reactor. The focus lies on the uncertainties induced by thermodynamic effects, aerodynamic effects and invasive measurement techniques in the experiments. It could be demonstrated that the simulation results are extremely helpful, first to improve the understanding of flow and temperature fields with regards to a variety of experimental setups, second to provide a better interpretation of the measurements under a variety of fluid mechanical effects, and finally to serve as a complementary tool to close the gap between the ideal one dimensional model assumption and the experimental measurements.

This thesis will be structured as follows: chapter 1 presents a brief introduction and motivation of the thesis. Chapter 2 gives a detailed description of the theoretical background of combustion, and a state-of-the-art overview of approaches for the kinetic modeling. Chapter 3 focuses on the gas-phase synthesis of nanoparticles, where the fundamental theory including nucleation, coagulation and coalescence is introduced. Further the population balance equation for the description of particle dynamics is discussed with its simplified form and several modeling approaches. Chapter 4 introduces basics of the numerical simulations in terms of spatial and temporal discretization schemes, pressure-velocity coupling and operator splitting, followed by a short introduction to the software frameworks Openfoam and Cantera. Flame and particle models implemented in this thesis are validated in chapter 5. Further, the robustness and reliability of these models are tested in the simulation of premixed flames, non-premixed flames and zero dimensional particle synthesis. Chapter 6 discusses the configuration of a set of experimental setups, namely the molecular beam mass spectrometry for ambient flames, the flame reactor for the study of flame structure, two reactor systems for the investigation of iron particle synthesis, a stagnation-flame for the measurements of soot particle size and a flame reactor exploring the synthesis process of silicon oxide particles. For each experiment, the potential effects that may cause the bias in the measurements are discussed individually. In chapter 7 the simulation results are shown and discussed. The last chapter draws a conclusion and gives an outlook for the future work.

Chapter 2

Physics of the laminar flame

In this chapter, the theoretical background and modeling of laminar flames is presented. Beginning with the basic conservation equations that determine the flow-, temperature- and species field, formulations of thermochemical and transport properties, i.e. heat capacity, viscosity, thermal conductivity and molecular diffusivity are discussed. In the end, the chemical kinetics for the description of combustion is introduced and its modeling methods are illustrated.

2.1 Conservation equations

Molecular dynamics of fluids are normally not of interest in industrial applications. Hence, the fluid is assumed to be a continuum, and the interactions between the molecules are described by semi-empirical constitutive equations. Only the mean quantities of the flow are considered. Therefore, motion of the fluid can be governed by a set of partial differential equations, resolving the conserved quantities. An isothermal, incompressible flow can be fully described by the conservation equations of mass and momentum. To describe a reactive flow, other additional conservation equations, i.e. of species and of energy, are required.

2.1.1 Conservation of mass

Mass can be neither created nor destroyed. Conservation of mass, also referred to as continuity equation, ensures that the temporal change of density at a point is equal to the convective transport of mass. The equation can be expressed in its differential form:

$$\frac{\partial \rho}{\partial t} + \nabla \cdot (\rho \boldsymbol{u}) = 0 \tag{2.1}$$

where ρ is the density and $\boldsymbol{u}$ the velocity vector of the flow. For constant density, the equation can be simplified to $\nabla \cdot (\boldsymbol{u}) = 0$, a volume continuity equation. Nevertheless, for combustion problems, the density can vary significantly due to strong temperature gradients, despite

the overall low Mach-number and a nearly isobaric pressure field. Equation 2.1 is used in the present study.

2.1.2 Conservation of momentum

Conservation of momentum is derived from Newton's first and second laws: the velocity of a flow remains constant unless external forces act upon the fluid element; the change of momentum of a flow is equal to the sum of the external forces. The balance equation for the momentum in differential form can be written as:

$$\frac{\partial}{\partial t}(\rho \boldsymbol{u}) + \nabla \cdot (\rho \boldsymbol{u}\boldsymbol{u}) = \nabla \cdot \boldsymbol{\tau} - \nabla p + \rho \boldsymbol{g} \tag{2.2}$$

On the left hand side (LHS) of this equation, the local change of momentum in time and the convective transport of momentum is presented. The first term on the right hand side (RHS) accounts for the stress tensor $\boldsymbol{\tau}$ that relates to the deformation of the fluid. The remaining terms on the RHS take account of the pressure gradient ∇p and the volume force $\rho \boldsymbol{g}$ acting on the fluid. For Newtonian fluids, $\boldsymbol{\tau}$ may be expressed as:

$$\boldsymbol{\tau} = \mu(\nabla \boldsymbol{u} + (\nabla \boldsymbol{u})^T - \frac{2}{3}\boldsymbol{I}\nabla \cdot \boldsymbol{u}) \tag{2.3}$$

The dynamic viscosity and the identity tensor are referred to as μ and I, respectively. For incompressible fluids, $\boldsymbol{\tau}$ may be simplified to:

$$\boldsymbol{\tau} = \mu(\nabla \boldsymbol{u} + (\nabla \boldsymbol{u})^T) \tag{2.4}$$

Inserting Equation 2.3 into Equation 2.2 leads to the well-known Navier-Stokes equation:

$$\frac{\partial}{\partial t}(\rho \boldsymbol{u}) + \nabla \cdot (\rho \boldsymbol{u}\boldsymbol{u}) = \nabla \cdot \mu(\nabla \boldsymbol{u} + (\nabla \boldsymbol{u})^T - \frac{2}{3}I\nabla \cdot \boldsymbol{u}) - \nabla p + \rho \boldsymbol{g} \tag{2.5}$$

The Navier-Stokes equations are numerically directly solved without any model. This type of simulation is named resolved laminar simulation.

2.1.3 Conservation of species

Balance equations for species are required for combustion simulations, where production, consumption, and mixing of the species occur at the same time. The species in reactive flow is represented by its mass fraction, defined as a ratio of the partial mass m_i of species i to the total mass of the reactive gas m:

$$Y_i = \frac{m_i}{m} \tag{2.6}$$

Each species in the reactive gas needs to be tracked individually. As shown in Equation 2.7, the balance of species i relates the change of mass fraction Y_i due to local change in time, the transport processes and the source term regarding either production or consumption $\dot{w}_i$:

$$\frac{\partial}{\partial t}(\rho Y_i) + \nabla \cdot (\rho Y_i(\boldsymbol{u} + \boldsymbol{V}_i)) = \dot{w}_i \tag{2.7}$$

The term $\dot{w}_i$ of species i is determined from chemical kinetics. The diffusive velocity of species is denoted by $\boldsymbol{V}_i$, which will be discussed in detail in subsection 2.2.2.

2.1.4 Conservation of energy

The energy in reactive flows can be defined by different quantities, where sensible enthalpy h_s is preferred in this study, as it only depends on the temperature change of the reactive flow. The specific sensible enthalpy of a single species is defined as:

$$h_{si} = h_i - h_i^\circ = \int_{T_0}^{T} (c_{p,i} dT) \tag{2.8}$$

Here, h_i° denotes the formation enthalpy of the species i under standard conditions (1 atm and 273 K); h_i is the specific species enthalpy and $c_{p,i}$ the specific heat capacity of the species i at constant pressure. The sensible enthalpy of the mixture ($h_s = \sum_i h_{si} Y_i$) is calculated as the mass weighted sum of the sensible enthalpies of pure species. The transport equation of sensible enthalpy is written as [26]:

$$\frac{\partial}{\partial t}(\rho h_s) + \nabla \cdot (\rho \boldsymbol{u} h_s) = \frac{Dp}{Dt} + \nabla \cdot (\boldsymbol{\tau} \boldsymbol{u}) + \nabla \cdot (\alpha \nabla h_s) + \nabla (\rho \sum_{i=1}^{N} h_{si} Y_i \boldsymbol{V}_i) + \dot{w}_T + \dot{Q} \tag{2.9}$$

On the LHS of this equation, the accumulation term and the convection term are present. The RHS of the equation states the change of sensible enthalpy in regards to different effects. The first two terms account for the effects of pressure variation due to volume compression and viscous heating, respectively. The third term describes the heat conduction, with α being the thermal diffusivity. The fourth term corresponds to the change of sensible enthalpy due to the diffusion of species with different sensible enthalpies. The remaining terms $\dot{w}_T$ and $\dot{Q}$ are source terms respectively responsible for the heat released or consumed by chemical reactions and external effects, such as radiation. The heat released from combustion $\dot{w}_T$ is determined from chemical kinetics and depends on the species reaction rate $\dot{w}_i$. It is written as:

$$\dot{w}_T = -\sum_{i=1}^{N} h_i^\circ \dot{w}_i \tag{2.10}$$

2.2 Thermochemical and transport properties of the mixture

As introduced in the last section, the thermochemical and transport quantities, i.e. the heat capacity, the viscosity, the thermal conductivity of the gas mixture and the diffusion coefficient of the mixture components are essential for the description of reactive flows. For pure species, the heat capacity, the viscosity and the thermal conductivity can be calculated from the kinetic gas theory [27]. The calculation of transport coefficients can be a major time consuming factor in multi-dimensional simulations. The main strategies to overcome the problem of direct calculation are tabulation and polynomial function fitting. The latter was used in the present work. For the gas mixture, the thermochemical and transport properties are determined from pure species properties and local species concentration. In the following, the heat capacity, the viscosity and the thermal conductivity are introduced by a mixture averaged method and the diffusion coefficient is determined by both mixture averaged- and multicomponent method.

2.2.1 Heat capacity, viscosity and thermal conductivity

In the present work, the heat capacity at constant pressure is calculated from the following equation:

$$c_p = \sum_{i=1}^{N} c_{pi} Y_i \tag{2.11}$$

Here c_{pi} stands for the heat capacity at constant pressure for pure species.

The viscosity is determined from a formula first proposed by Wilke [28] and modified by Bird et al. [29]. This formula is expressed as:

$$\mu = \sum_{i=1}^{N} \frac{X_i \mu_i}{\sum_{j=1}^{N} X_j \phi_{ij}} \tag{2.12}$$

Here

$$\phi_{ij} = \frac{1}{\sqrt{8}} \left(1 + \frac{W_i}{W_j}\right)^{-1/2} \left(1 + \left(\frac{\mu_i}{\mu_j}\right)^{1/2} \left(\frac{W_j}{W_i}\right)^{1/4}\right)^2 \tag{2.13}$$

In the equations above, $X_{(\cdot)}$, $\mu_{(\cdot)}$, and $W_{(\cdot)}$ denote the mole fraction, the pure species viscosity and the molecular mass, respectively. The subscripts refer to the species index.

The thermal conductivity is calculated based on the formula proposed by Mathur and Saxena [30], as a function of the mole fraction X_i and the thermal conductivity λ_i:

$$\lambda = \frac{1}{2} \left(\sum_{i=1}^{N} X_i \lambda_i + \frac{1}{\sum_{i=1}^{N} X_i / \lambda_i} \right) \tag{2.14}$$

The description of the mass diffusion coefficient will be discussed in the following subsection.

2.2.2 Mass diffusion

The species diffusion flux $\rho Y_i \boldsymbol{V}_i$ in Equation 2.7, can be calculated using either the multicomponent or mixture-averaged approaches. The diffusion velocity $\boldsymbol{V}_i$ in the multicomponent method is derived from the Stefan-Maxwell formulation. Neglecting volumetric forces acting on the species and the Soret effect caused by the temperature gradient, the Stefan-Maxwell formula gives:

$$\nabla X_i = \sum_{j=1}^{N} \frac{X_i X_j}{D_{ij}} (\boldsymbol{V}_j - \boldsymbol{V}_i) + (Y_i - X_i) \left(\frac{\nabla p}{p} \right) \tag{2.15}$$

Here, D_{ij} accounts for the binary diffusion coefficient shown in Equation 2.20. The equation above represents a linear system of size N^2, and its mathematical solution is expensive in terms of computational resources. To overcome this issue, the calculation of the diffusion velocity can be simplified using the mixture-averaged approach. First, by assuming only two species in the system and neglecting the pressure gradient, Equation 2.15 is simplified to:

$$\nabla X_1 = \frac{X_1 X_2}{D_{1,2}} (\boldsymbol{V}_2 - \boldsymbol{V}_1) \tag{2.16}$$

Due to the conservation relations $X_1 + X_2 = 1$ and $X_1 V_1 + X_2 V_2 = 0$, Equation 2.16 is simplified as:

$$V_1 X_1 = -D_{12} \nabla X_1 \quad \text{or} \quad V_1 Y_1 = -D_{12} \nabla Y_1 \tag{2.17}$$

which is known as Fick's law [31] with the binary diffusion coefficient D_{12} of species 1 into species 2. For a gas mixture, the diffusion of species i needs to be considered regarding all the other species of the mixture, and Equation 2.17 is transformed to:

$$V_i Y_i = -D_{mi} \nabla Y_i \tag{2.18}$$

Here,

$$D_{mi} = \frac{1 - Y_i}{\sum_{j \neq i} X_j / D_{ji}} \tag{2.19}$$

In this equation, the binary diffusion coefficient is derived from the kinetic gas theory using the Chapman-Enskog theorem:

$$Dji = \frac{1.863 \cdot 10^{-3} \sqrt{T^3 (W_i + W_j)}}{p \sigma_{ij}^2 \Omega_{ij}} \tag{2.20}$$

Here, σ_{ij} is the mean collision diameter and Ω_{ij} the collision integral. Both are dependent on the temperature and change with the species combinations. They are determined by experiments or kinetic theory. The calculation of the temperature dependent binary diffusion coefficients and pure species transport properties can be very time consuming. Usually performed prior to a simulation, these material properties are tabulated or fitted in polynomial expressions.

2.2.3 Global conservation of species

The sum of partial masses must preserve the total mass (Equation 2.1). However, the mixture-averaged approach for the approximation of mass diffusion cannot ensure the conservation. This issue and the solution approaches are discussed in the following section. The sum of all the transport equations for species is:

$$\sum_i^N \frac{\partial}{\partial t}(\rho Y_i) + \sum_i^N \nabla \cdot (\rho Y_i \boldsymbol{u}) = -\sum_i^N \nabla \cdot (\rho Y_i \boldsymbol{V}_i) + \sum_i^N \dot{w}_i \tag{2.21}$$

Based on the fact that the sum of mass fractions must be unity ($\sum_i^N Y_i = 1$), and that all the species have the same convective velocity $\boldsymbol{u}$, the LHS of the equation above can be considered as mass conservation equation, leading to the following expression:

$$\frac{\partial \rho}{\partial t} + \nabla \cdot (\rho \boldsymbol{u}) = -\sum_i^N \nabla \cdot (\rho Y_i \boldsymbol{V}_i) + \sum_i^N \dot{w}_i = 0 \tag{2.22}$$

In the above equation, $\sum_i^N \dot{w}_i$ must be zero, based on mass conservation. The term $\sum_i^N \nabla \cdot (\rho Y_i \boldsymbol{V}_i)$ should be zero, if the diffusion velocity $\boldsymbol{V}_i$ of species i is calculated in the detailed way, namely the multicomponent method. However, the mixture averaged approximation may lead to $\sum_i^N \nabla \cdot (\rho Y_i \boldsymbol{V}_i) = -\sum_i^N \nabla \cdot (\rho D_{mi} \nabla Y_i) \neq 0$. To ensure the conservation of species, two methods are widely used in the numerical simulations.

In the first method, only $N-1$ species are calculated in the transport equation. The remaining species is determined from the equation $Y_N = 1 - \sum_i^{N-1} Y_i$. Therefore, the inconsistency caused by the mixture averaged method is accumulated into the remaining species that is usually chosen as an abundant species (e.g. nitrogen or argon). However, care should be taken for flows that are not highly diluted, where the mass fraction of inert species is not large. Moreover, for reactive flows, the species may diffuse with significantly different velocities. Therefore, the first method can predict species with notable error.

The second method introduces an external term (correction velocity $\boldsymbol{V}_c$) in the diffusion velocity of the species transport equation to enforce $\sum_i^N \nabla \cdot (\rho Y_i \boldsymbol{V}_i)$ to be zero. In this method, the diffusion flux can be expressed as:

$$Y_i \boldsymbol{V}_i = -D_{mi} \nabla Y_i + Y_i \boldsymbol{V}_c \tag{2.23}$$

and $\boldsymbol{V}_c$ is defined as:

$$\boldsymbol{V}_c = \sum_i^N D_{mi} \nabla Y_i \tag{2.24}$$

Finally, substituting Equation 2.23 into Equation 2.7 yields the species transport equation that satisfies the global species conservation:

$$\frac{\partial}{\partial t}(\rho Y_i) + \nabla \cdot (\rho Y_i \boldsymbol{u}) = \nabla \cdot \rho D_{mi} \nabla Y_i - \nabla \cdot (\rho Y_i \boldsymbol{V}_c) + \dot{w}_i \tag{2.25}$$

It should be stressed that in this work, the mentioned two methods are used together, as suggested from the book [26].

2.3 Chemical reaction

The following section will give a brief introduction to the modeling of chemically reacting flows and a range of approaches for modeling reaction kinetics.

2.3.1 Reaction kinetics

Combustion releases heat by converting chemical bond energy into thermal energy. This process can be described by a global irreversible exothermic chemical reaction and be written as:

$$\text{Fuel} + \text{Oxidizer} \longrightarrow \text{Product}$$

Here the fuel and oxidizer burn as a flame into the products. However, in reality the components of the fuel and the oxidizer may not be simply rearranged to form the products. Instead, the molecules of the reactants decompose into smaller molecules or atoms, which are then converted into new species. Therefore a set of elementary reactions forming a reaction mechanism, is required to consider the development of all critical species involved in the combustion process.

A detailed reaction mechanism is complex and depends on the type of fuel. For example, hydrogen flames can be fully described by 8 reactions and less than 30 species, as proposed by Li et al. [32], whereas a detailed mechanism for methane contains over 1000 reactions of more than 100 species [33]. Another example is the complex detailed mechanism developed by De Witt et al. [34] for the simulation of tetra-decane combustion, which is comprised of 479,206 reactions and 19,052 species. Nevertheless, not all species influence the global scheme, and the size of the reaction mechanism can be reduced. For example, if only the thermochemical state of the combustion is relevant (temperature of exhaust gas), the following 4-step mechanism proposed by Jones and Lindstedt [35] is often sufficient for the simulation of a methane flame.

$$\begin{aligned}
2\,CH_4 + O_2 &\longrightarrow 2\,CO + 4\,H_2 \\
CH_4 + H_2O &\longrightarrow CO + 3\,H_2 \\
CO + H_2O &\rightleftharpoons CO_2 + H_2 \\
2\,H_2 + O_2 &\rightleftharpoons 2\,H_2O
\end{aligned}$$

The set of reactions above contains irreversible and reversible reactions, indicated by unidirectional arrow and bidirectional arrow, respectively.

In its abstract form, the set of chemical reactions containing N_r reactions with N species can be written as:

$$\sum_{i=1}^{N} \nu'_{i,r} \chi_i \rightleftharpoons \sum_{i=1}^{N} \nu''_{i,r} \chi_i \quad \text{with} \quad r \in \{1...N_r\} \tag{2.26}$$

where χ_i is the chemical symbol for species i, and for each reaction r, $\nu_r^{'}$ and $\nu_r^{''}$ refer to molar stoichiometric coefficients for reactant and product respectively. The expression of reaction rate (Equation 2.27) depends on the molar concentration of species $[X_i]$, which is the ratio of partial density and molecular weight ($[X_i] = \frac{\rho Y_i}{W_i}$). In addition, the reaction rate is also calculated from reaction coefficients for forward and backward reactions, denoted by $k_{f,r}$ and $k_{b,r}$ respectively.

$$RR_r = k_{f,r} \prod_{i=1}^{N} [X_i]^{\nu_{i,r}^{'}} - k_{b,r} \prod_{i=1}^{N} [X_i]^{\nu_{i,r}^{''}} \tag{2.27}$$

The reaction coefficient for the forward reaction is calculated from an Arrhenius temperature dependency:

$$k_{f,r} = A_r T^{\beta_r} \exp(-E_r / R_r T) \tag{2.28}$$

Here, the frequency factor, the temperature exponent, the activation energy and the universal gas constant for the r-th reaction are referred to as A_r, β_r, E_r and R_r, respectively.

The reverse reaction coefficient is determined from the forward reaction coefficient $k_{f,r}$ and equilibrium constant by the mass action law:

$$k_{b,r} = \frac{k_{f,r}}{K_{c,r}} \tag{2.29}$$

where the equilibrium constant depends on the entropy ΔS_r°, the enthalpy ΔH_r°, the pressure p and the temperature T:

$$K_{c,r} = \exp\left(\frac{\Delta S_r^{\circ}}{R} - \frac{\Delta H_r^{\circ}}{RT}\right) \left(\frac{p}{RT}\right)^{\sum_{i=1}^{N} (\nu_{i,r}^{'} - \nu_{i,r}^{''})} \tag{2.30}$$

The specific amount of consumed or produced species per time unit can be calculated from the corresponding equations.

$$\dot{w}_i = W_i \sum_{r=1}^{N_r} (\nu_{i,r}^{'} - \nu_{i,r}^{''}) RR_r \tag{2.31}$$

2.3.2 Modeling of the reaction kinetics

As introduced in the previous subsection, chemical mechanisms can be described at different levels of complexity for the modeling of reactive flows, depending on the target of the investigation. In general, the modeling of kinetics can be separated in two groups: fast chemistry and finite rate chemistry. The fast chemistry assumes that chemical reactions occur instantaneously and hence are not kinetically controlled [27]. In contrast, the finite rate chemistry implies a kinetically controlled process. To chose the suitable model for

a simulation, the dimensionless parameter Damköhler number can be introduced, which depends on the flow time scale τ_f and the chemical times scale τ_c:

$$Da = \frac{\tau_f}{\tau_c} \tag{2.32}$$

The flow time scale τ_f may be defined in many ways, according to the characteristics of the investigated system. For instance, τ_f can be considered as a characteristic mixing time for a diffusion flame. The interpretation of the Da number is the following: if the chemical time τ_c is much smaller than the flow time τ_f, the Damköhler number tends to infinity, and fast chemistry can be considered. When the chemical time is comparable with the flow time, the Damköhler number becomes near unity, and the finite rate chemistry needs to be accounted for. In the following, fast and finite chemistry approaches are briefly introduced, with the focus on the finite rate chemistry, as it is used in the present work.

Fast chemistry

For fast chemistry, the chemical reactions are limited only by mass diffusion or mixing. This treatment of the chemical reactions is suitable for the description of cases that are limited by diffusion. For example, in turbulent diffusion flames, fuel oxidation and heat release are governed by turbulent transport and mixing. The overall characteristics of such a flame can be sufficiently predicted assuming the fast chemistry. For modeling of fast chemistry, the method of infinitely fast reaction and chemical equilibrium are widely used. They are briefly introduced in the following.

The approach of infinitely fast reaction consists of one or more specified reactions that take place infinitely fast. The definition of 'infinitely fast' means that reactants are converted into products immediately after the mixing of fuel and oxidizer. This process is also known as 'mixed is burned'. Typical models therefore are the Eddy break-up model [36, 37] and the Eddy-Dissipation model [38]. In these two models, the combustion process is described by the turbulent mixing.

The chemical equilibrium approach requires more computationally effort than the infinitely fast reaction approach. By assumption of chemical equilibrium, the concentration of reactants and products do not change with time. This state is achieved when forward reactions proceed with the same rate as reverse reactions. In 1873, Gibbs [39] defined the Gibbs free energy, an important property to assess the chemical equilibrium state. Once the Gibbs free energy attains its minimum value, the chemical equilibrium of the system is obtained. For a gas-phase system with N species, the total Gibbs free energy is defined as:

$$G = \sum_{i=1}^{N} n_i \cdot \left(G^{\circ}_{f,i} + RT \ln \frac{p_k}{p^{\circ}} \right) = \sum_{i=1}^{N} n_i \cdot \left(G^{\circ}_{f,i} + RT \ln X_i \right) \tag{2.33}$$

where n_i stands for the number of moles for species i and $G^{\circ}_{f,i}$ is the energy of formation under the standard condition for species i. Hence the Gibbs free energy at constant temperature and pressure is a function of n_i. Finally, the concentration of species at equilibrium

state is obtained through minimization of Gibbs free energy with the limitation of mass conservation. Such a problem can be solved by several methods [40]; a frequently used one is that of "undetermined Lagrange multipliers" [41]. Although computing the chemical equilibrium is more complex, the assumption of chemical equilibrium and the assumption of the infinitely fast chemistry often yield the similar results for the combustion system. Except for the partial conversion of reactants to products, the effect of chemical equilibrium needs to be accounted for. For a temperature dependent exothermic reaction system, the chemical equilibrium may shift to reactants at high temperature, since the complete consumption of reactants only occurs at relatively low temperature.

Both the infinitely fast chemistry and the chemical equilibrium model can often predict the major species in combustion systems with satisfying accuracy. However, these two models are not suitable for predicting minor species such as carbon monoxide, nitrogen oxides and sulfur oxides.

Finite rate chemistry

Finite rate chemistry models are developed for combustion processes that are kinetically controlled. Based on the degree of the complexity, the finite rate chemistry approaches can be divided into global reactions, reduced mechanisms and detailed mechanisms.

The simplest way to describe finite rate chemistry is by global reaction. Here, the reactions are described by one or several Arrhenius expressions. The global reaction is an attractive method for industrial applications, as it has high computational efficiency if it is combined with the CFD simulations involving the description of complex fluid dynamics. Moreover, this model is applied when the knowledge of detailed chemistry is not available. Nevertheless, it should be stressed that the applications of global reactions are normally constrained within a narrow region of operation conditions (temperature and pressure) for which the global reactions are developed. Errors may arise from using global reactions beyond these conditions.

The detailed reaction mechanism is a collection of elementary reactions, including the rate at which the chemical process proceeds at the molecular level. Typically, the reaction mechanism provides chemical information as a list of species and reactions, where the rate coefficient for each elementary reaction is given. Furthermore, transport coefficients for each species are necessary if the problem addresses transport phenomena. In addition, the thermochemical data (heat capacity, standard enthalpy and entropy) for each species must be given in order to calculate the reverse rate constant from the given forward rate constants. Due to the advances in experimental methods over the past two decades, numerous databases containing thermodynamic data are now available. Interested readers are referred to several important sources, such as thermochemical kinetics from Benson [42], thermochemical data of organic compounds developed by Pedley et al. [43], the Chemkin thermodynamic database given by Kee et al. [44] and the JANAF thermochemical tables from Chase et al. [45]. Although databases have been improved, thermodynamic data for some key species are still not available. Hence many methods are developed to estimate these data. A review of some estimation procedures is given by Senkan [46].

Since the 1980s, the detailed reaction mechanisms have become an important tool for the analysis of combustion and high temperature processes because of the rapid growth of powerful computer resources. Kinetic modeling using detailed reaction mechanisms coupled with simple fluid dynamics shows its advantages in the prediction and understanding of the combustion system under conditions that are dangerous, expensive or difficult to be attained in laboratories. Additionally, due to the fact that detailed reaction mechanisms contain the full set of elementary reactions covering a wide range of operating conditions and combustion phenomena, they are usually used as a reference to validate the simplified chemistry models.

Even though the detailed reaction mechanisms describe the overall chemical processes accurately, the computational cost may become prohibitive for simulations with complex fluid dynamics. For such cases, reduced mechanisms are used. Reduced mechanisms are smaller than detailed mechanisms in the number of species and reactions while they still provide reasonable accuracy under specific conditions.

Over the past three decades, mechanism reduction techniques have been comprehensively developed and investigated [47, 48, 49, 50]. Three groups of widely used reduction techniques are briefly introduced in the following.

In the first group, redundant species and/or reactions that have no contribution to the given modeling target are removed from a detailed mechanism, which in turn leads to a skeletal mechanism that describes the minimum subset of the full mechanism under specific conditions. In order to identify which species and reactions are kinetically important for the modeling, a combination of path flux analysis [51] and sensitivity analysis [52] are commonly used. The reaction path represents atom flux between the species through the elementary reactions, thereby identifying the critical species and the reactions that are responsible for formation and consumption of reactants, intermediates and products. The sensitivity analysis is used to evaluate the change in species concentration induced by the small change in reaction rate. In this way, the reactions which limit the overall process are found. An alternative to eliminate the species and their associated reactions is the genetic algorithm, inspired by the mechanism of evolution and natural genetics. The genetic algorithm identifies a better sub-mechanism based on one or several objective functions in an iterative modeling of the homogenous reactor or one dimensional laminar flame. The number of species and reactions in the sub-mechanism is fixed and specified at the beginning of each step. During the iterative process, the performance of the sub-mechanism is compared with the detailed mechanism and the species in the sub-mechanism are manipulated to gain a better simulation result. After a certain number of iterations, if no further improvement can be found, the best sub-mechanism that represents the detailed mechanism is obtained. A review about mechanism reduction using this algorithm is given by Tomlin et al. [53], Lu et al. [54] and Sikalo et al. [55]. The genetic algorithm works particular well for mechanism optimization, as introduced by Sikalo et al. [56].

The second group of reduction techniques are lumping approaches [57, 58, 59], where similar species and reaction pathways are grouped into sets, thereby reducing the number of variables that need to be tracked. Normally, the species are grouped if they have the similar

thermal and transport properties. In addition, the lumping algorithm can be also used to bundle the species having similar diffusivity. The work of Lu et al. [60] demonstrates that such methods can reduce simulation time, as the calculation of differential species diffusivity is very cpu-time consuming.

The third group of reduction techniques is developed based on the time-scale analysis. One widely used method is the classic quasi-steady state assumption (QSSA) [61], which identifies the "fast" radicals that quickly reach quasi-steady state, where the radical production balances the radical consumption. Hence, the concentration of species are coupled into algebraic equations and the simulation time is significantly reduced by removing the transport equations for "fast" species. Another popular method is the intrinsic low-dimensional manifold method (ILDM) [62, 63], which assumes a quick convergence of the reaction trajectory to a low-dimensional manifold that represents the reduced mechanism by a small number of species. Other methods like the computational singular perturbation (CSP) [64] and the principal component analysis (PCA) [65] are able to distinguish "fast" reactions and "slow" reactions by the means of the Jacobian matrix.

Chapter 3

Nanoparticle synthesis from the gas-phase

The first part of this chapter introduces the main mechanisms affecting formation and growth of nanoparticles. In the second part, the modeling approaches for the population balance equation, that describes the particle dynamics, are discussed. In the last part, two specific models, Prakash's [66] and Kruis' [67] model, which are implemented in the present work, are presented in detail.

3.1 Governing mechanisms

The synthesis of nanoparticles is a complex process involving many physical and chemical mechanisms. The governing mechanisms for the synthesis of nanoparticles are nucleation, coagulation and coalescence. Figure 3.1 shows the processes of nanoparticles formation from the gas-phase flame. The synthesis processes follow the sequence of nucleation, coagulation and coalescence [68].

3.1.1 Nucleation

Nucleation is the first step of the particle formation [69, 70, 68], and will be described in an example of laminar flame-assisted synthesis from the gas phase in the following. For the synthesis, a precursor is added into laminar, premixed, flat flames. The precursor vapour is mixed together with the fresh gas and fed into the reactor system. After ignition, the flame heats up the precursor vapour that may further decompose or react with the intermediate species of the flame, leading to a supersaturated state of precursor vapour. This state is non-equilibrium for the precursor vapour and tends to equilibrium by forming particles through homogenous or heterogeneous nucleation [70].

Homogenous nucleation occurs without a preferential nucleation site (nuclei or crystals) [69]. It is a spontaneous and random process. The exact formation of nuclei is complex and uncertain. The classical theory of nucleation was studied by Gibbs [71], Volmer [72],

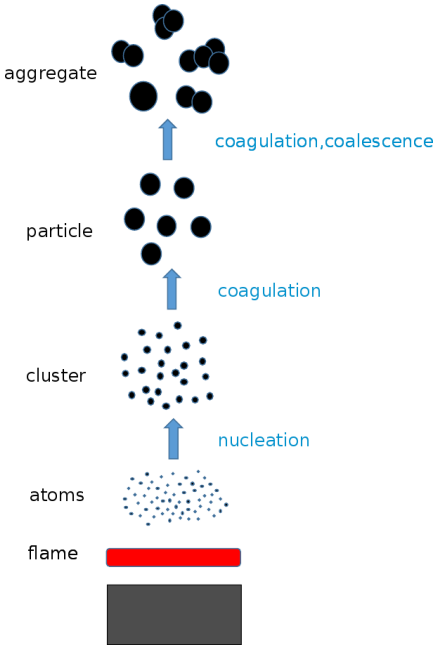

Figure 3.1: Classic processes of nanoparticle synthesis in a flat flame.

Becker and Döring [73] and others. Their work focused originally on the condensation of a vapour to a liquid, and was extended to crystallization of melts and solutions. This process is shortly introduced as follows: after the appearance of microscopic droplets (nuclei), the condensation of vapour takes place on the droplet surface. However, due to the high vapour pressure, the droplets may evaporate rapidly. As a result, the formation and the evaporation occur simultaneously. The stable droplet can finally be formed by coagulation or in the environment of high supersaturation. The formation of nuclei is likely a sequence of molecular addition [74]:

$$\begin{aligned} A + A &\rightleftharpoons A_2 \\ A_2 + A &\rightleftharpoons A_3 \\ &\dots \\ A_{n-1} + A &\rightleftharpoons A_n \end{aligned}$$

where A_n is called critical cluster, and further molecular addition to it causes nucleation

and growth of the nuclei.

The process of homogeneous nucleation can be thermodynamically described by the change of total free energy of a nucleus, which is the sum of surface free energy and the bulk free energy. For a spherical nucleus with radius r, it can be written as:

$$\Delta G = 4\pi r^2\gamma + \frac{4}{3}\pi r^3 \Delta G_v \tag{3.1}$$

where γ and ΔG_v refer to the surface energy and the free energy of the bulk nucleus, respectively. The free energy of the nucleus depends on the temperature T, the Boltzmann's constant k_B, the supersaturation ratio S and the molar volume v_m:

$$\Delta G_v = \frac{-k_B T \ln(S)}{v_m} \tag{3.2}$$

The change of the free energy attains a maximum for the nucleus with a critical radius r_{crit} (see Figure 3.2). This maximum free energy is the barrier that the nucleus needs to pass through to achieve the stable state.

In differential form, Equation 3.1 is written as:

$$\frac{d\Delta G}{dr} = 8\pi r\gamma + 4\pi r^2 \Delta G_v = 0 \tag{3.3}$$

By rearranging Equation 3.3, the critical radius r_{crit} is obtained, which is the smallest size for a stable nuclei:

$$r_{crit} = -\frac{2\gamma}{\Delta G_v} = \frac{2\gamma v_m}{k_B T \ln S} \tag{3.4}$$

Heterogeneous nucleation occurs if the solution contains the impurities of another phase. Here, the nuclei are formed on the surface of the foreign particles. According to the classic nucleation theory, the change of free energy is highly dependent on the surface free energy. Unlike the homogeneous nucleation, contact between the nuclei and the foreign particle surfaces violates the spherical shape of the nuclei. As illustrated in Figure 3.3, the decreasing contact angle Θ leads to the decreasing free surface area of the nuclei, which in turn results in a decreasing barrier energy. A correction factor ϕ, as a function of contact angle, needs to be multiplied with the barrier energy for the homogenous nucleation to account for the mentioned contact effect, resulting in:

$$\Delta G_{crit}^{hetero} = \phi \Delta G_{crit}^{homo} \quad \text{with} \quad \phi = \frac{(2+\cos\theta)(1-\cos\theta)^2}{4} \tag{3.5}$$

Due to the decreased change of the free energy, the heterogeneous nucleation occurs more often than homogenous nucleation.

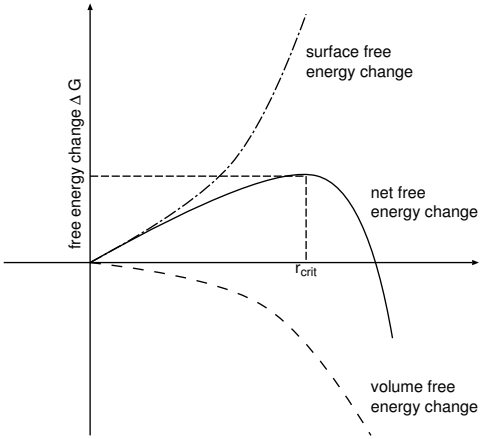

Figure 3.2: Free energy change for homogeneous nucleation.

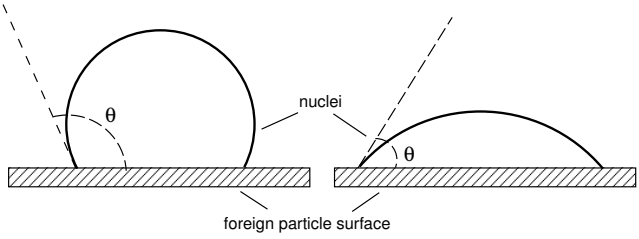

Figure 3.3: Surface area of nuclei decrease with the reduced contact angle.

3.1.2 Coagulation

Particles collide due to their random motion and stick together due to intermolecular forces. This process is well known as particle coagulation [68, 75, 76] and leads to a decrease in the total number of particles and an increase of the particle size. Coagulation of particles is affected by thermal motion (Brownian motion), laminar shear, turbulence, and external forces (gravity and electrical force). In this thesis, the coagulation of nanoparticles is mainly determined by the Brownian motion, which will be addressed in detail. The collision rate of two particles with different size, denoted by i and j, can be calculated as [68]:

$$N_{ij} = \beta_{i,j} n_i n_j \tag{3.6}$$

where β is the collision frequency function and n_i and n_j denote the total particle number of particles. The collision frequency function is characterized by the Knudsen number (Kn), which is a ratio of molecular free path length of the fluid to the particle radius. For particle sizes much larger than the molecular free path length (Kn < 0.1), the particles are in continuum regime, whereas for particles smaller than the molecular free path (Kn > 10), the particles are in free molecular regime. The collision frequency in the continuum regime is expressed as a function of temperature T, viscosity of the fluid μ and the collision radius r_c:

$$\beta_{i,j} = \frac{2k_B T}{\mu}\left(\frac{1}{r_{ci}} + \frac{1}{r_{cj}}\right)(r_{ci} + r_{cj}) \tag{3.7}$$

For a monodisperse system ($r_{ci} = r_{cj}$), this equation reduces to $\beta = \frac{8k_B T}{\mu}$. In the free molecular regime (Kn > 10), where the particles and the fluid hardly interact, the particles behave like molecules and follow the kinetic gas theory. The collision frequency is then written as:

$$\beta_{i,j} = \pi(d_{ci} + d_{cj})^2 \sqrt{\frac{k_B T}{2\pi}\left[\frac{1}{m_{pi}} + \frac{1}{m_{pj}}\right]} \tag{3.8}$$

In the above equation, the collision diameter and the particle mass are denoted by d_c and m_p respectively. A transition regime is defined by $0.1 <$ Kn < 10, there is no exact definition for the collision frequency of the particles in this regime. However, Fuchs [77] proposed an interpolation method to cover the regime from the continuum to the free molecule. This method will be discussed in section 3.2.2.

3.1.3 Coalescence

Sintering or coalescence takes place once two solid spherical particles coagulate [78, 79, 80]. This process changes the structure and the surface area of particles. The driving force for sintering is the reduction of the surface energy. Variation of the surface area causes the gradients in vapor pressure, surface stress and chemical potential, which in turn results

in material transport into the neck region that joins the two particles (see Figure 3.4). Mechanisms of material transport include surface diffusion, grain boundary diffusion, lattice diffusion, evaporation and condensation, and depend on the material properties and the operating environment.

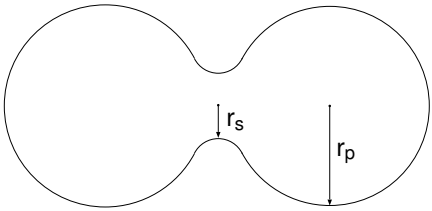

Figure 3.4: Sketch of two sintering particles.

The early phase of sintering can be described by a classical sintering model, where the increase of the neck radius r_s, relative to the initial spherical particle radius r_p, is given by:

$$\left(\frac{r_s}{r_p}\right)^n = \frac{B(T)t}{r_p^m} \tag{3.9}$$

Here, $B(T)$ is a temperature dependent coefficient, the exponent m and n are determined by the type of material transport. In the case of surface diffusion, m and n are set to 7 and 4 respectively. However, the above equation is restricted to the early stage of sintering with a neck radius ratio of $r_s/r_p < 0.3$. Despite of this limit, Equation 3.10 can still be used to calculate the characteristic time for neck growth:

$$\tau_s = \frac{d_p^m}{B(T)} \tag{3.10}$$

Koch and Friedlander [81] proposed a first order equation to describe agglomerate sintering. In their equation, the change of aggregate surface area a depends on the sintering characteristic time τ_s and the minimum aggregate surface area a_s.

$$\frac{\partial a}{\partial t} = \frac{1}{\tau_s}(a - a_s) \tag{3.11}$$

In contrast to Equation 3.9 for the early sintering stage, Equation 3.11 is valid from the equilibrium to the final sintering stage. However, a general model covering the whole range of the sintering process does not exist.

The characteristic time for sintering highly influences the particle morphology. If the sintering process is much faster than the coagulation process, full sintering occurs and spherical particles are formed. Due to a decrease of the gas temperature and growth of the particle

size, the coagulation rate may become comparable with the sintering rate. As a result, particles cannot sinter completely and form aggregates with a branched structure. The particle morphology is varied with the irregular shape, and further affects the particle mobility, scattering and functionality. The evolution of the particle morphology is too complex for a mathematical description. Nevertheless, the aggregates have a fractal morphology that can be described by the fractal dimension D_f. With the fractal dimension, the number of primary particles in an aggregate is calculated from the aggregate diameter d_a and the primary particle diameter d_p:

$$n_p = A\left(\frac{d_a}{d_p}\right)^{D_f} \tag{3.12}$$

The coefficient A depends on the aggregate diameter and the Knudsen number. The fractal-like concept is simple and does not cover all the possible aggregate structures. However, it is an appropriate model for many aerosol processes.

3.2 Population balance equation

During the formation of particles from the gas phase, processes such as coagulation, coalescence and particle transport determine the change of the particle size distribution function n in time and space. The general dynamic equation (GDE) is used to fully describe these processes. By applying proper initial and boundary conditions, this equation can be solved to obtain the accurate particle size distribution function n. Hence, by the means of parameter study, the GDE provides an effective route for the design and optimization of aerosol process conditions. The GDE includes terms related to convection, diffusion, growth and coagulation of particles, and can be written as:

$$\frac{\partial n}{\partial t} + \nabla \cdot n\boldsymbol{u} - \nabla \cdot D_p \nabla n = \left[\frac{\partial n}{\partial t}\right]_{growth} + \left[\frac{\partial n}{\partial t}\right]_{coagu.} - \nabla \cdot \boldsymbol{c}n \tag{3.13}$$

where D_p is the particle diffusion coefficient. The velocity of gas and particle is respectively denoted by $\boldsymbol{u}$ and $\boldsymbol{c}$, the latter results from external forces. The first term on the RHS is the growth term:

$$\left[\frac{\partial n}{\partial t}\right]_{growth} = \frac{\partial I}{\partial v} \tag{3.14}$$

Here, the particle current I is a sum of diffusion and migration in the space of particle volume v. The second term on the RHS is known as a coagulation term, which depends on β, the collision frequency function, also known as a coagulation kernel. The coagulation term is written as:

$$\left[\frac{\partial n}{\partial t}\right]_{coagu.} = \frac{1}{2}\int_0^v \beta(\widetilde{v}, v-\widetilde{v})n(\widetilde{v})n(v-\widetilde{v})d\widetilde{v} - \int_0^\infty \beta(\widetilde{v}, v)n(v)n(\widetilde{v})d\widetilde{v} \tag{3.15}$$

The first term on the RHS accounts for the particle collisions between two classes of particles with the particle volume $\widetilde{v}$ and v. A factor 1/2 ensures that the same particle collision does not count twice. The second term on the RHS presents the loss rate of particles with size v due to the collision with all other particles. Inserting Eq. 3.14 and Eq. 3.15 into Eq. 3.13, leads to a GDE in the continuous form:

$$\frac{\partial n}{\partial t} + \nabla \cdot n\boldsymbol{u} - \nabla \cdot D_p \nabla n = \frac{\partial I}{\partial v} + \frac{1}{2}\int_0^v \beta(\widetilde{v}, v-\widetilde{v})n(\widetilde{v})n(v-\widetilde{v})d\widetilde{v} - \int_0^\infty \beta(\widetilde{v}, v)n(v)n(\widetilde{v})d\widetilde{v} - \nabla \cdot \boldsymbol{c}n \tag{3.16}$$

The GDE is a type of population balance equation (PBE) in a integro-differential form and its analytical solution can be found for few special configurations only. In order to solve the PBE numerically, Equation 3.16 needs to be modeled into simple expressions. Common models are the discrete model, the sectional model, the method of moments and the monodisperse model. Detailed introductions for these models are found in the book of Friedlander [68]. Here, just a brief introduction will be given in the following pages. Figure 3.5 shows the distribution function of the particle size related to the different models. The sub-figures are put in decreasing order of computational cost and simulation accuracy for the individual model.

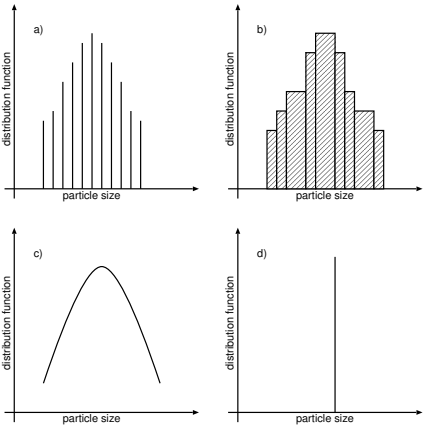

Figure 3.5: Distribution function of particle size for a) the discrete, b) the sectional, c) the moments and d) the monodisperse model.

The discrete model describes the particle sizes as discrete variables, which comprise of different numbers ($i = 1, 2...N$) of monomers. For each particle size, an individual conservation or transport equation needs to be solved. Normally, the nucleation term in these

differential equations is described in detail, containing the number of formed monomers, dimers, trimers and so on. The discrete model yields the exact solution of Eq. 3.16 when the number of discrete variables tends to infinity. However, due to the high computational cost, the discrete model is usually limited to the particle size distribution in a small range (up to 200 monomers). For larger size ranges, the computational cost becomes prohibitive and the simpler models are required.

The sectional model approximates the particle phase space into classes (bins) or sections, where the particle properties, i.e. particle size, surface area and volume are assumed to be constant. For each section, differential equations are solved to obtain the characteristics (number, surface or volume concentration) of the particles. Depending on the target of investigation, the characteristic of interest changes. For example, the optical characteristic can be better represented as the conservation of surface area rather than volume [82]. Due to the particle growth during the simulation, the particle size distribution, as illustrated in Figure 3.5b, changes its form extensively. Thus, the number and width of sections need to be selected according to the particle distribution. Normally, a large number of sections in the model yields accurate simulation results but increases the computational cost. An alternative to the sectional model is the nodal approach, in which the particle distribution is represented by a number of discrete nodes. A widely used nodal model proposed by Prakash et al. [66] is implemented in this work, the details of this model are introduced in section 3.2.1.

The discrete-sectional model is a combination of the sectional model and the discrete model. In this combined model, the size range is divided into two parts: sectional and discrete. The interaction of monomers and small clusters with the limited size are calculated in discrete model, for an accurate description of early particle formation. The sectional model is applied for the bigger particles or clusters to reduce the computational cost. Even though the discrete-sectional model is computationally more efficient than the discrete model, its application is still limited for the discrete sizes up to 100 and the sections up to 100 [70].

The method of moments uses the low order moment of the particle size distribution to describe the process of the particle formation. The moments are integrals of the distribution function. Different particle parameters can be obtained from the different moments, for example 0^{th}, 2^{nd} and 3^{rd} moment represent respectively, the total number concentration, the total surface area concentration and the total volume concentration. Rather than the calculated distribution function in discrete and sectional models, the method of moments requires the closure by assuming the shape of the particle size distribution function. As shown in the investigations by Pratsinis et al. [83] and Bensberg et al. [84], for many of practical cases a reasonable shape assumption is the log normal distribution function, which is characterised by the particle concentration, the geometric volume and the standard deviation. By applying the method of moments, the PBE is converted into transport equations for the moments of the distribution function. As a result, the complex equation system is reduced to a small number of moment equations, leading to a highly decreased computational cost. The accuracy of this method strongly depends on the selection of a presumed distribution function. The method of moments is not feasible for cases where the presumed distribution function

does not correlate with the real distribution. Nevertheless, once the distribution shape is known and can be expressed as an analytic function, this method features an attractive and efficient model for the description of the main physical and chemical phenomena (collision, coalescence and deposition) in the process of the particle formation.

The monodisperse model assumes a log-normal particle size distribution in the method of moments. Monodisperse means that the model assumes all the particles having the same size at the same spatial location and the same time. Although the assumption is a strong simplification, the monodisperse model is still able to capture the main physical phenomena that affect the growth of aggregates. As a result, a time and space dependent mean particle size can be obtained. Compared to the other models introduced above, the monodisperse model requires the least computational resources. This is a big advantage for the simulations of complex flow with the particle formation. A further advantage is its simple structure, which makes the programming straightforward. The monodisperse model is specified by different terms that describe formation, growth and transport of the particle. In the presented work, the model developed by Kruis et al. [67] is employed and extended, the details are discussed in section 3.2.2.

3.2.1 Prakash's model

Prakash's model [66] extends the coagulation equation developed by Lehtinen [85] and modifies the sectional method from Gelbard [86]. The model describes chemical and physical phenomena including nucleation due to supersaturation, surface growth due to evaporation/condensation of monomers and coagulation of the particles. Rather than the finite-size sections used in the sectional model, the particle size domain in Prakash's model is discretised into a number of discrete nodes, which represent particles of a fixed particular size. As a result, the integral appearing in the coagulation/growth term reduces to the sum of nodal based variables (particle number concentration), leading to a simplification of the calculation.

To be consistent with the applied monodisperse model, the modeling of nucleation and surface growth in Prakash's model are put aside, and the coagulation is introduced in detail. A general transport equation including the accumulation term, the convection term, the diffusion term and the source term for the particle number concentration in the node k, is presented in Equation 3.17, with D_p being the particle diffusion coefficient, and w_k the source term:

$$\frac{\partial N_k}{\partial t} + \boldsymbol{u} \cdot \nabla N_k - \nabla \cdot (D_p \nabla N) = w_k \tag{3.17}$$

The particle diffusion coefficient D_p depends on the Boltzmann constant k_B, the temperature T, the fluid viscosity μ and the particle diameter d_p:

$$D_p = k_B T \frac{C_c}{3\pi\mu d_p} \tag{3.18}$$

Here, C_c is the slip correction factor, which ensures D_p covering the range from continuum to free molecular regime. It is defined as an interpolation formula:

$$C_c = \frac{5 + 4\mathrm{Kn} + 6\mathrm{Kn}^2 + 18\mathrm{Kn}^3}{5 - \mathrm{Kn} + (8+\pi)\mathrm{Kn}^2} \tag{3.19}$$

For the calculation of the Knudsen number Kn, here the mean free path is given by:

$$\lambda = k_B T / \sqrt{2}\pi d_p^2 p \tag{3.20}$$

The characteristic length scale is the particle radius. The term w_k accounts for coagulation between the particles and is given by:

$$w_k = \begin{cases} -\sum_{i=1}^{N_s} \beta_{i1} N_i N_1, & k = 1 \quad (3.21) \\ \frac{1}{2}\sum_{i=1}^{N_s}\sum_{j=1}^{N_s} \chi_{ijk}\beta_{ij} N_i N_j - \sum_{i=1}^{N_s} \beta_{ik} N_i N_k, & k > 1 \quad (3.22) \end{cases}$$

Equation 3.21 relates to the monomers ($k = 1$) and Equation 3.22 to the particles larger than the monomers ($k > 1$). The particle number is reduced due to collisions, represented by the negative terms in the two equations. Simultaneously, the number of the particles within the node k increases due to the collisions of the small particles, which is indicated by the first term in the lower equation. A factor $1/2$ ensures that the same particle collision does not count twice. The coagulation frequency β_{ij} for the collision between two particles with the volume v_i and v_j is expressed as follows, whereρ_p is the particle density:

$$\beta_{ij} = \left(\frac{3}{4\pi}\right)^{\frac{1}{6}} \left(\frac{6k_B T}{\rho_p}\right)^{\frac{1}{2}} \left(\frac{1}{v_i} + \frac{1}{v_j}\right)^{\frac{1}{2}} (v_i^{\frac{1}{3}} + v_j^{\frac{1}{3}})^2 \tag{3.23}$$

This expression works well for the free molecule regime. However, for a wide region from the continuum to the free molecule regime, the Fuchs interpolation needs to be applied. As shown by Wagner et al. [87], the Fuchs interpolation agrees well with the experimental results, and can successfully describe the Brownian coagulation. This interpolation is formulated as:

$$\beta_{ij} = 2\pi(d_{pi}+d_{pj})(D_{pi}+D_{pj}) \left[\frac{d_{pi}+d_{pi}}{d_{pi}+d_{pj}+2(g_i^2+g_j^2)^{\frac{1}{2}}} + \frac{8(D_{pi}+D_{pj})}{(d_{pi}+d_{pj})(C_i^2+C_j^2)^{\frac{1}{2}}}\right]^{-1} \tag{3.24}$$

In the equation above, the parameter g_i for a particle i is written as:

$$g_i = \frac{[(d_{pi}+l_i)^3 - (D_{pi}^2 + l_i^2)^{\frac{3}{2}}]}{3 d_{pi} l_i} - d_{pi} \tag{3.25}$$

where the mean free path of a particle i is referred to as l_i:

$$l_i = \frac{8D_{pi}}{\pi C_i} \tag{3.26}$$

The particle velocity C_i for a particle i is calculated as:

$$C_i = \sqrt{\frac{8K_B T}{\pi \rho_p v_i}} \tag{3.27}$$

Due to the collision of two particles (v_i and v_j), a new particle is formed with a volume of $v_i + v_j$. For particles with a size between two bins, the splitting operator χ_{ijk} is used to preserve the total particle mass, and defined as follows:

$$\chi_{ijk} = \begin{cases} \dfrac{v_{k+1} - (v_i + v_j)}{v_{k+1} - v_k}; & \text{if} \quad v_k \leq v_i + v_j \leq v_{k+1}, \\ \dfrac{(v_i + v_j) - v_{k-1}}{v_k - v_{k-1}}; & \text{if} \quad v_{k-1} \leq v_i + v_j \leq v_k, \\ 0; & \text{otherwise} \end{cases} \tag{3.28}$$

3.2.2 Kruis' model

A popular monodisperse model is Kruis' model [67], which describes the growth of the aggregate volume and the surface area by considering simultaneous coagulation and sintering. The primary particle size and the aggregate size are assumed to be monodisperse at the same point in space and time. The structure of the aggregates is taken into account by a mass fractal dimension D_f.

At the early stage of the particle evolution, the coalescence is much faster than the coagulation, resulting in spherical particles. It increases the particle size and the coagulation rate. After the coagulation rate becomes comparable to the sintering rate, the particles cannot maintain a spherical shape and the aggregates are formed with a different structure. The number concentration of aggregates N decreases due to collision between aggregates with the collision frequency β, and can be described by:

$$\frac{\partial N}{\partial t} = -\frac{1}{2}\beta N^2 \tag{3.29}$$

The change of the surface area of an aggregate is mainly affected by coagulation and sintering, expressed as:

$$\frac{\partial a}{\partial t} = -\frac{1}{N}\frac{\partial N}{\partial t}a - \frac{1}{\tau}(a - a_s) \tag{3.30}$$

The first term on the RHS accounts for the increase of surface area due to coagulation and the second term for decrease due to sintering. The characteristic sintering time is τ, its

formula will be introduced later. The surface area of a spherical aggregate is denoted by a_s, and is expressed as:

$$a_s = \left(\frac{v}{v_0}\right)^{\frac{2}{3}} a_0 \tag{3.31}$$

Here, v_0 and a_0 are the monomer volume and the surface area respectively. The increase of an aggregate volume v_a due to the coagulation can be written as:

$$\frac{\partial v_a}{\partial t} = -\frac{1}{N}\frac{\partial N}{\partial t} v_a \tag{3.32}$$

The collision frequency β in Equation 3.38 is calculated using the Fuchs interpolation, which depends on the diffusion coefficient D_p, the particle velocity C, the parameter g and the collision radius r_c:

$$\beta = 8\pi D_p r_c \left(\frac{r_c}{2r_c + \sqrt{2}g} + \frac{\sqrt{2}D_p}{C r_c}\right)^{-1} \tag{3.33}$$

The parameter g accounts for the transition from the free molecular regime to the continuum regime. The collision radius is chosen instead of the solid sphere radius because of the irregular shape of the aggregate, and is calculated as:

$$r_c = \frac{3V}{A}\left(\frac{A^3}{36\pi N V^2}\right)^{\frac{1}{D_f}} \tag{3.34}$$

The total volume concentration and the total surface concentration of particles are referred to as V and A, respectively. The mass fractal dimension D_f ranges from 1.8 to 3, accounting for the shape of open clusters to spherical aggregates. The diffusion coefficient D_p is calculated as:

$$D_p = \frac{k_B T}{6\pi\mu r_c}\left[\frac{5 + 4\mathrm{Kn} + 6\mathrm{Kn}^2 + 18\mathrm{Kn}^3}{5 - \mathrm{Kn} + (8+\pi)\mathrm{Kn}^2}\right] \tag{3.35}$$

Here, k_B, T, μ and Kn refer to the Boltzmann constant, the temperature, the viscosity of fluid and the Knudsen number, respectively. The particle velocity C , the parameter g, and the mean free path of particle l are calculated respectively based on Equation 3.27, 3.25 and 3.26.

The characteristic sintering time depends on the primary particle size $d_p = 6V/A$ and temperature, which is defined as [88]:

$$\tau = A d_p \exp\left(\frac{T_a}{T}\right) \tag{3.36}$$

The pre-exponential factor A and the activation temperature T_a are determined from the experiments.

So far, Kruis' model was developed to describe the collision and sintering of aggregates. However, the formation of new particles in not taken into account by Kruis' model. In order to fully describe the evolution process from the gas phase to final aggregates, Kruis' model is extended with a nucleation term. Assuming that the monomers are stable particles, the nucleation rate I can be converted from the production rate of the related species, such as Fe_2O_3 for iron oxide particles:

$$I = -\frac{\partial Y_i}{\partial t}\rho N_A/M \tag{3.37}$$

Here, ρ is the density, N_A the Avogadro's number and M the molar mass of the species. The monomers are assumed to be stable particles due to the lack of reliable information on the early stage of particle formation. However, this assumption has been applied by several researchers [89, 90].

In order to capture the transport processes of nanoparticles, the three differential equations are modified and extended by including convective transport, diffusive transport and nucleation [91]. Rather than the volume and the surface area of the aggregate, the total volume concentration $V = N \cdot v$ and the total area surface concentration $A = N \cdot a$ of particles are calculated. The three differential equations are:

$$\frac{\partial N}{\partial t} + \nabla \cdot (\boldsymbol{u}N) - \nabla \cdot (D_p \nabla N) = -\frac{1}{2}\beta N^2 + \boldsymbol{I} \tag{3.38}$$

$$\frac{\partial V}{\partial t} + \nabla \cdot (\boldsymbol{u}V) - \nabla \cdot (D_p \nabla V) = \boldsymbol{I} v_0 \tag{3.39}$$

$$\frac{\partial A}{\partial t} + \nabla \cdot (\boldsymbol{u}A) - \nabla \cdot (D_p \nabla A) = -\frac{1}{\tau}(A - N a_s) + \boldsymbol{I} a_0 \tag{3.40}$$

In the above equations, the diffusion coefficient D_p is determined by Equation 3.35. Kruis' model or its extended version have been applied for numerous studies of particle dynamics in different material systems. In the work of Kruis et al. [67], the monodisperse model is applied for the particle growth of silicon. Pratsinis et al. [90], Heine et al. [92], Jeong et al. [93] and Schild et al. [94] used the extended model for the investigation of TiO_2 synthesis. Gröhn et al. [95], Weise et al. [96] and Tsantilis et al. [97] applied this model in the spray-assisted synthesis process. The particle growth of Fe_2O_3 is studied by Wlokas et al. [91] and by Kowalik et al. [98], using the extended version of Kruis' model. In the works mentioned above, the simulation results are compared with the experimental measurements or more complex models, such as the sectional model and the method of moments, and a satisfactory agreement is achieved. The model provides an insight into the synthesis process and works well for an essential parameter study for the control of the synthesis process.

Chapter 4

Numerical approach

In order to describe the behaviour of a reactive flow, the transport equations need to be solved in the computational domain. These partial differential equations are non-linear and their analytical solution is thus not feasible except for very few, simple generic flow configurations. To obtain an approximate solution, the transport equations are discretized in space and time, resulting in a set of algebraic equations that are numerically solved by the computer. Spatial discretization is carried out by the finite volume method (FVM), and introduced in section 4.1. Section 4.2 presents the time discretization in terms of explicit- and implicit schemes. The subsequent section addresses the coupling technique used for pressure and velocity. Operator splitting for the simulations, suffering from multiple-time scales is discussed in section 4.4. Finally, two software frameworks, Openfoam and Cantera are shortly introduced.

4.1 Spatial discretization

By applying the finite volume method, the numerical domain is divided into a number of finite volumes (cells) that fill the domain and don't overlap with each other.

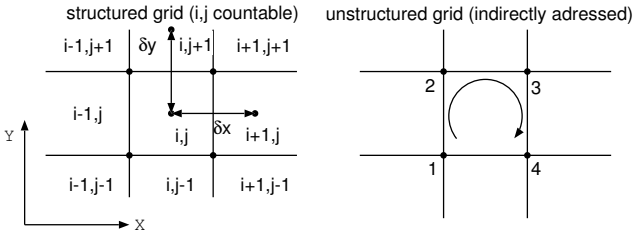

Figure 4.1: Schematic of the 2-D structured and unstructured grid.

Numerical grids can be generally categorized as structured and unstructured, as sketched in Figure 4.1. A structured grid may comprise of rectangular elements (2D) or hexahedral elements (3D), which are represented by their index i, j or i, j and k, respectively. The unique index of each element indicates its location in the Cartesian space in x, y direction for 2D and in x, y, z direction for 3D. Moreover, the location of each cell can be calculated from the locations of its neighbours based on their center distance along the x-direction (δx) and the y-direction (δy). This simple connectivity between neighbouring cells is easily programmed and saves memory space of the computer. However, the structured grid may be difficult to describe the complex geometries. Therefore, unstructured grids are widely used for complex geometries due to the possible irregular shape of the cells. The connectivity between the unstructured cells are defined in a list, which contains the information of vertices, faces and boundaries. For both structured- and unstructured grids, the control volumes are connected by the internal faces, and the numerical grid is bounded by the boundary faces. The variables required for the governing equations can be stored either at the volume centers or at the face centers, depending on the employed algorithm. For the present work, the "collocated" arrangement is used, therefore all the variables are stored at the center of the cell.

4.1.1 Integral of transport equations

As aforementioned, the transport equations can be approximated in a system of algebraic equations, which can be solved by a computer. A general transport equation of generic quantity Φ is taken as an example to explain the process of spatial discretization.

$$\underbrace{\frac{\partial}{\partial t}(\rho\Phi)}_{\text{accumulation}} + \underbrace{\nabla\cdot(\rho\boldsymbol{u}\Phi)}_{\text{convection}} + \underbrace{\nabla\cdot(\rho\Gamma\nabla\Phi)}_{\text{diffusion}} = \underbrace{\dot{w}_\Phi}_{\text{source}} \tag{4.1}$$

Here, Γ is the general diffusivity of Φ. The integration of Equation 4.1 over a volume yields:

$$\int_V \frac{\partial}{\partial t}(\rho\Phi)dV + \int_V \nabla\cdot(\rho\boldsymbol{u}\Phi)dV + \int_V \nabla\cdot(\rho\Gamma\nabla\Phi)dV = \int_V \dot{w}_\Phi dV \tag{4.2}$$

By applying Gauss' theorem,

$$\int_V \nabla\cdot\Phi dV = \int_S \Phi\cdot\boldsymbol{n}dS \tag{4.3}$$

the convective- and diffusive terms can be expressed as fluxes over surfaces, leading to:

$$\frac{\partial}{\partial t}\int_V (\rho\Phi)dV + \int_S \nabla\cdot(\rho\boldsymbol{u}\Phi)\cdot\boldsymbol{n}dS + \int_S \nabla\cdot(\rho\Gamma\nabla\Phi)\cdot\boldsymbol{n}dS = \int_V \dot{w}_\Phi dV \tag{4.4}$$

Up to now, the equation can still provide an exact solution, although only applicable for some simple generic configurations. To express this equation in an algebraic form, an

approximation is made: the volume integrals of quantity Φ are approximated as the product of its value at the midpoint of the cell Φ_M and the cell volume δV. A volume integral is thus expressed as:

$$\int_V \Phi dV \approx \Phi_M \delta V \tag{4.5}$$

Although other higher order approximation schemes exist, this equation is sufficient for 2^{nd} order accuracy in space. Similarly, the surface integrals can be express as:

$$\int_S \Phi \cdot \boldsymbol{n} dS \approx \sum_f \Phi_f \boldsymbol{n}_f \delta S \tag{4.6}$$

Here, Φ_f denotes the value of Φ at the face. The face normal and the face area is represented by $\boldsymbol{n}_f$ and δS respectively. Applying Equation 4.5 and 4.6 to Equation 4.4 leads to:

$$\frac{\partial}{\partial t}(\rho \Phi_M)\delta V + \underbrace{\sum_f (\rho \boldsymbol{u}_f \Phi_f) \cdot \boldsymbol{n}_f \delta S}_{\text{convection}} + \underbrace{\sum_f (\rho \Gamma \nabla \Phi_f) \cdot \boldsymbol{n}_f \delta S}_{\text{diffusion}} = \dot{w}_{\Phi,M} \delta V \tag{4.7}$$

The values of quantities stored at the cell faces (indicated by the subscript $(*)_f$) of the control volume are still unknown. Hence, further approximations are needed to obtain the value on the cell faces from the quantities stored on the cell centers by interpolation. In the next subsections, approximations for the convective- and diffusive fluxes will be introduced.

4.1.2 Approximation of the convective flux

The convective mass flux through a face of a control volume is known as:

$$F = \rho \boldsymbol{u}_f \boldsymbol{n}_f \delta S \tag{4.8}$$

Using this expression, the convective flux of Φ can be simplified into:

$$\sum_f (\rho \boldsymbol{u}_f \Phi_f) \cdot \boldsymbol{n}_f \delta S = \sum_f F \Phi_f \tag{4.9}$$

The face value Φ_f can be determined by different schemes, which are discussed in the following.

Upwind differencing (UD)

For upwind differencing, the value of Φ_f is fixed to a value stored at the center point of the upstream cell. For a control volume, its own and neighbor cell center are denoted by P and N. Given a face f between them and a flux F through the face f, the differencing scheme is defined by:

$$\Phi_f = \begin{cases} \Phi_P & \text{if } F \geq 0 \\ \Phi_N & \text{if } F < 0 \end{cases} \tag{4.10}$$

As a first order scheme, upwind differencing yields larger truncation errors compared to higher order schemes. Further, this scheme may cause significant numerical diffusion that distort the solution of flames, where physical diffusion drives the combustion process [99]. Nevertheless, it ensures the boundedness of the solution and therefore avoids the amplification of numerical oscillation.

Central differencing (CD)

The central differencing is a simple linear interpolation of Φ_P and Φ_N:

$$\Phi_f = \psi_x \Phi_P + (1 - \psi_x)\Phi_N \tag{4.11}$$

Here, the interpolation factor ψ_x is calculated from the distance between f and N and the distance between P and N:

$$\psi_x = \frac{|x_N - x_f|}{|x_N - x_P|} \tag{4.12}$$

Compared to the upwind scheme, central differencing is second order accurate and thus suppresses the numerical diffusion. However, its truncation error can cause numerical instability. In particular, for the transport of scalars, the diffusion may be too small to compensate for numerical oscillations. As a result, the simulation may become unstable.

Blended differencing (BD)

In order to preserve a bounded and accurate solution, the blended differencing scheme is developed as a linear combination of the upwind- and the central differencing. This scheme inherits the advantages of the two differencing schemes above and it is written as:

$$\Phi_f = (1 - \gamma)\Phi_f(UD) + \gamma \Phi_f(CD) \tag{4.13}$$

Here, γ is a blending factor, which can be set constant for all the faces of the grid. It varies between zero and one, and controls the numerical diffusion in the simulation. By setting $\gamma = 0$ and $\gamma = 1$, the blended differencing is reduced to upwind differencing and central differencing, respectively. Alternatively, the blended factor may be calculated adaptively

using the Total Variation Diminishing (TVD) [100] or the Normalized Variable Approach (NVA) [101, 102]. For the detailed discussion on these two approaches, interested readers are referred to the references [103, 104, 105, 106].

Besides TVD and NVA schemes, other approaches exist for low-diffusive, non-oscillatory scalar transport. Well-known ones are the Flux Corrected Transport (FCT) [107] and the Essentially Non-Oscillatory (ENO) schemes [108]. Due to the complexity and slightly higher computational cost of these approaches, they are not applied here.

4.1.3 Approximation of the diffusive flux

The diffusive flux is known in Equation 4.7,

$$\sum_f (\rho \Gamma \nabla \Phi_f) \cdot \boldsymbol{n}_f \delta S \tag{4.14}$$

where the gradient $\nabla \Phi_f$ remains unknown. For an orthogonal mesh, the vector through the center points P and N is parallel to the face normal $\boldsymbol{n}_f$. Therefore, the gradient is given by:

$$\nabla \Phi_f = \frac{\Phi_N - \Phi_P}{|x_N - x_P|} \tag{4.15}$$

However, the mesh is not orthogonal in most practical cases. Equation 4.15 needs to be split into orthogonal contribution I and non-orthogonal correction II:

$$\boldsymbol{n}_f \cdot \nabla \Phi_f = \underbrace{\boldsymbol{J} \cdot \nabla \Phi_f}_{\text{I}} + \underbrace{\boldsymbol{K} \cdot \nabla \Phi_f}_{\text{II}} \tag{4.16}$$

in this equation, the following condition must be satisfied:

$$\boldsymbol{J} + \boldsymbol{K} = \boldsymbol{n}_f \tag{4.17}$$

There are many approaches to determine the vector $\boldsymbol{J}$, as introduced in details in the literature [104, 109]. With the calculated $\boldsymbol{J}$, the vector $\boldsymbol{K}$ is obtained from Equation 4.17.

4.2 Temporal discretization

Temporal discretization is used for the accumulation term in the transport equations. Applying the temporal integral and inserting Equation 4.9 in Equation 4.7, a "semi-discretized" form of the transport equation is obtained:

$$\int_t^{t+\delta t} \left[\frac{\partial}{\partial t} (\rho \Phi_M) \delta V + \sum_f F \Phi_f + \sum_f (\rho \Gamma \nabla \Phi_f) \cdot \boldsymbol{n}_f \delta S \right] \delta t = \int_t^{t+\delta t} \left[\dot{w}_{\Phi,M} \delta V \right] \delta t \tag{4.18}$$

Many methods have been developed during the years to solve the time integral. For most of these methods, the center value Φ_M, the face value Φ_f and the gradient $\delta\Phi$ are assumed to be constant during the time step Δt. The temporal discretization schemes are distinguished based on the evaluation of these three values, from the new or the old time. Three of them will be introduced in the following. For the following subsection, the superscript $\circ$ denotes "old" and n stands for "new".

Explicit

In the explicit schemes, the spatial terms are discretized using values from the previous time step (old) to calculate the values at the current time (new). A common scheme is the forward Euler method, where the fully discretized transport equation is expressed as:

$$\rho\frac{\Phi_M^n - \Phi_M^\circ}{\delta t}\delta V + \sum_f F\Phi_f^\circ + \sum_f(\rho\Gamma\nabla\Phi_f^\circ)\cdot\boldsymbol{n}_f\delta S = \dot{w}_{\Phi^\circ,M}\delta V \tag{4.19}$$

The Euler explicit scheme yields first order accuracy in time. Other high order explicit schemes like the Runge-Kutta scheme are preferred for practical cases with a strong transient behaviour. A stability criterion for explicit schemes is the CFL number:

$$\mathrm{CFL} = \frac{\boldsymbol{U}_f\cdot\delta t}{|x_N - x_P|} \tag{4.20}$$

Explicit schemes tend to become unstable when the CFL number is larger than unity. Therefore, for a stable simulation run, $\mathrm{CFL} \leq 1$ needs to be satisfied:

Implicit

Implicit schemes use values from the new time step. A common scheme is the backward Euler method, where the fully discretized transport equation is written as:

$$\rho\frac{\Phi_M^n - \Phi_M^\circ}{\delta t}\delta V + \sum_f F\Phi_f^n + \sum_f(\rho\Gamma\nabla\Phi_f^n)\cdot\boldsymbol{n}_f\delta S = \dot{w}_{\Phi^n,M}\delta V \tag{4.21}$$

This scheme is of first order accuracy in time, unconditionally stable and ensures the boundedness of the solution. Compared to the explicit scheme, the Euler implicit scheme allows relatively big time steps, which makes it attractive for cases with weakly transient behaviour or for steady state solutions.

Implicit-explicit hybrid

For an implicit-explicit hybrid scheme, the value of the spatial terms is evaluated from both the previous and the current time step, using a trapezoidal rule. A common approach is the Crank-Nicolson method, where the temporal integral is:

$$\int_t^{t+\delta t}\Phi dt = \frac{1}{2}(\Phi^\circ + \Phi^n)\delta t \tag{4.22}$$

Using Equation 4.22, the fully discretized form of the transport equation is given by:

$$\begin{aligned}\rho\frac{\Phi_M^n-\Phi_M^\circ}{\delta t}\delta V+&\frac{1}{2}\sum_f F\Phi_f^\circ+\frac{1}{2}\sum_f(\rho\Gamma\nabla\Phi_f^\circ)\cdot\boldsymbol{n}_f\delta S\\&+\frac{1}{2}\sum_f F\Phi_f^n+\frac{1}{2}\sum_f(\rho\Gamma\nabla\Phi_f^n)\cdot\boldsymbol{n}_f\delta S\\&=\frac{1}{2}\dot{w}_{\Phi^\circ,M}\delta V+\frac{1}{2}\dot{w}_{\Phi^n,M}\delta V\end{aligned}\tag{4.23}$$

The Crank-Nicolson method is of second order accuracy in time.

With the aforementioned spatial and temporal discretization schemes, a linear algebraic equation for each control volume can be obtained. A general form of the linear algebraic equation is:

$$a_P\Phi_P^n+\sum_N a_N\Phi_N^n=R_P\tag{4.24}$$

The coefficients a_P and a_N are determined by the prefactors of Φ. The value of Φ_P^n depends on the values of the neighbouring cells. The source term is denoted by R_P. This type of linear algebraic equation system can be expressed in a matrix form

$$[A][\Phi]=[R],\tag{4.25}$$

Here, A is a sparse square matrix with coefficient a_P on the diagonal and a_N off the diagonal. There are many efficient approaches to solve such a sparse matrix system, and interested readers are referred to the literature [104].

4.3 Pressure-Velocity Coupling

The transport equations for continuity and momentum, the Navier-Stokes equations, provide four equations with four unknowns: velocities in three directions and pressure. The pressure is coupled with the velocity in the transport equation of momentum, therefore neither pressure nor velocity can be solved solely. Moreover, the continuity equation does not contain the information of pressure. Due to the lack of an independent equation for the pressure, a straightforward solution of the pressure is not feasible. Therefore, pressure-velocity algorithms are proposed to overcome the aforementioned issue. The most common pressure-velocity algorithms are the "semi-implicit method for pressure linked equations" (SIMPLE) [110] and the "pressure implicit with splitting of operators" (PISO) [111].

The SIMPLE algorithm employs the coupled relation of the velocity and the pressure to build a pressure correction equation that enforces the mass conservation and obtains the pressure field. The velocity is then corrected by the calculated pressure gradient. However, after calculation of the pressure correction, the velocity and the velocity flux may not satisfy the momentum balance. The calculation needs to be repeated iteratively until the balance

is satisfied. The PISO algorithm evolved from the SIMPLE algorithm. It overcomes the mentioned shortcomings of the SIMPLE algorithm with two correction steps: the neighbour and the skewness correction. In the neighbour correction, the iterative calculations are moved into PISO loops. The PISO algorithm takes slightly longer run time per iteration than the SIMPLE algorithm, but reduces the number of iterations required for convergence, especially for transient cases. The skewness correction is used for the skew meshes. Due to the skewness of skewed cells, the pressure correction struggles to satisfy the conservation of the momentum equation in a single step. Therefore, an iterative process similar to the neighbour correction is needed. The pressure gradient is recalculated after the initial solution of the pressure correction and the momentum flux is updated using the pressure gradient. This iterative process can reduce the convergence difficulties induced by the skewness of the cells.

In this thesis, the PISO algorithm is applied to the investigated problems. The procedure of this algorithms is shown as follows:

(a) Predict velocity flux: momentum equations are calculated using the pressure field from the previous time step, since the exact pressure field at the current time step is not known yet. A genetic form of the momentum equation, taking the gradient of pressure as a source term $\boldsymbol{S}(p)_f$ is expressed as [104]:

$$a_p \boldsymbol{u_f} = \boldsymbol{H(u)} - \sum_N \boldsymbol{S}(p)_f \tag{4.26}$$

with the transport term

$$\boldsymbol{H(u)} = -\sum_N a_N \boldsymbol{u_N} + \frac{\boldsymbol{u}^\circ}{\Delta t} \tag{4.27}$$

rearranging Equation 4.26, the velocity fluxes are calculated as:

$$\boldsymbol{u_f} = \left(\frac{\boldsymbol{H(u)}}{a_p}\right)_f - \left(\frac{1}{a_p}\right)_f (\nabla p)_f \tag{4.28}$$

(b) Solve the pressure correction equation: the pressure correction equation is constructed by enforcing the velocity from the momentum equation to satisfy the continuum equation. The predicted velocity from the first step is used to calculate $\boldsymbol{H(u)}$. The pressure gradient is updated according to Equation 4.29

$$\nabla \cdot \left(\frac{1}{a_p} \nabla p\right) = \nabla \cdot \left(\frac{\boldsymbol{H(u)}}{a_p}\right) = \sum_f \boldsymbol{S} \cdot \left(\frac{\boldsymbol{H(u)}}{a_p}\right)_f \tag{4.29}$$

(c) Correct velocity flux: the face flux F is calculated from:

$$F = \boldsymbol{S} \cdot \boldsymbol{u}_f = \boldsymbol{S} \cdot \left[\left(\frac{\boldsymbol{H(u)}}{a_p}\right)_f - \left(\frac{1}{a_p}\right)_f (\nabla p)_f\right] \tag{4.30}$$

(d) Reconstruct the velocity: the velocity is updated with the new pressure field explicitly:

$$\boldsymbol{u_p} = \frac{\boldsymbol{H(u)}}{a_p} - \frac{1}{a_p}\nabla p \tag{4.31}$$

These steps are repeated for the prescribed number of steps or until a convergence criterion is satisfied.

4.4 Operator Splitting

Multi-physics problems are usually modeled by a set of linear or non-linear differential equations. Often, many of them are mathematically stiff systems, which span a big range of time scales that differ by orders of magnitude. For example, the modeling of a methane flame may cover the time scales for the NO_x formation (10 s), gas transportation (1 ms), and formation of some critical radicals (1 μs). Due to the complexity of the system, a unique numerical method, which can provide an accurate solution to every physical process within a reasonable integration time, does not exist. Operator splitting method is designed to solve the problem [112, 113]. This method splits the spatial differential operator into a sum of sub-operators with respect to different physical phenomena. The relatively simple form of sub-operators can be solved by easy numerical approaches.

In order to introduce the splitting scheme properly, the system of ordinary differential equations is simplified into a form consisting of two operators M and S, where ϕ is the unknown quantity and ϕ_0 is the given initial condition of ϕ:

$$\begin{cases} \dfrac{d\phi(t)}{dt} = M\phi(t) + S\phi(t), \quad 0 < t < T \\ \phi(0) = \phi_0 \end{cases}$$

The simplest operator splitting method is the sequential splitting. According to the work of Csomós et al. [114], this method is defined in the following sequence:

$$\begin{cases} \dfrac{d\phi_1(t)}{dt} = S\phi_1(t), \quad (n-1)\tau < t \leq n\tau \\ \phi_1((n-1)\tau) = \phi_{spl}((n-1)\tau) \end{cases}$$

$$\begin{cases} \dfrac{d\phi_2(t)}{dt} = M\phi_2(t), \quad (n-1)\tau < t \leq n\tau \\ \phi_2((n-1)\tau) = \phi_1(n\tau) \end{cases}$$

$$\begin{aligned} &\text{with} \quad \phi_{spl}(n\tau) = \phi_2(n\tau) \\ &\qquad n = 1, 2, 3...N \end{aligned}$$

where $\phi_{spl}(t)$ is the solution of the whole system on the mesh. The sequential splitting divides the time interval into N steps with a time step size τ. At each time-step, two simple sub-problems are solved. The sub-problems are connected via initial conditions. This method is of first order accuracy and unconditionally stable. It is illustrated in a schematic diagram in Figure 4.2.

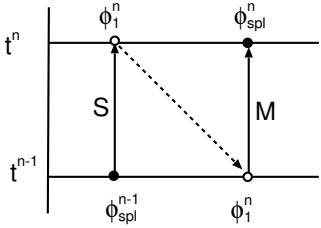

Figure 4.2: Sketch of the sequential splitting scheme.

The following, simple splitting technique is applied in the present work. The transport equation for species involved in the laminar flame model is split into the two sub-operators. For the first sub-operator, the chemical source terms is solved for each individual cell as a zero-dimensional batch reactor. The kinetic equations are integrated over a time step Δt using the Radau-IIA method [115]. The reaction rate in the species transport equation is calculated from the change of molar concentration C:

$$\dot{w}_i = M_i \frac{C_i(t_0 + \Delta t) - C_i(t_0)}{\Delta t} \tag{4.32}$$

In the second sub-operator, the flow transport is calculated based on equation 2.7 using the time step Δt, which is much larger than the characteristic chemical time step. This technique highly reduces the overall computational time.

Many other more complex splitting techniques have been developed during the years, here two of them are briefly introduced for the future development of the operator splitting in Openfoam. The first one is the Strang-Marchuk splitting [116, 117], where three sub-problems are solved in a sequence at each time step [114]:

$$\begin{cases} \dfrac{d\phi_1(t)}{dt} = S\phi_1(t), \quad (n-1)\tau < t \leq (n-\dfrac{1}{2})\tau \\ \phi_1((n-1)\tau) = \phi_{spl}((n-1)\tau) \end{cases}$$

$$\begin{cases} \dfrac{d\phi_2(t)}{dt} = M\phi_2(t), \quad (n-1)\tau < t \leq n\tau \\ \phi_2((n-1)\tau) = \phi_1((n-\dfrac{1}{2})\tau) \end{cases}$$

$$\begin{cases} \dfrac{d\phi_3(t)}{dt} = S\phi_3(t), \quad (n-\dfrac{1}{2})\tau < t \leq n\tau \\ \phi_3((n-\dfrac{1}{2})\tau) = \phi_2(n\tau) \end{cases}$$

with $\phi_{spl}(n\tau) = \phi_3(n\tau)$

$n = 1, 2, 3...N$

The Strang-Marchuk splitting theory is of second order accuracy and unconditionally stable if the operators M and S are positive definite matrices. The procedure of this splitting technique is shown in Figure 4.3.

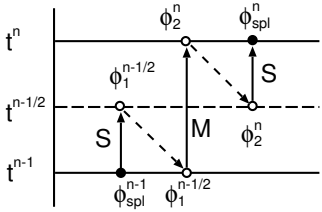

Figure 4.3: Sketch of the Strang-Marchuk splitting scheme.

For the system with more than two operators, the operators can be arranged in different ways:

$$L = M_1 + M_2 + M_3 = (M_1 + M_2) + M_3 = M_1 + (M_2 + M_3) \tag{4.33}$$

The second splitting technique is the so called "weighted sequential splitting", where two sequential splittings are applied in different order:

$$\frac{\phi(t)}{dt} = \Theta(M\phi(t) + S\phi(t)) + (1-\Theta)(S\phi(t) + M\phi(t)) \tag{4.34}$$

In the above equation, terms like $M\phi(t) + S\phi(t)$ and $S\phi(t) + M\phi(t)$ are calculated following the procedure of the sequential splitting. If the weighting factor Θ is set to $1/2$, the splitting technique becomes a symmetrically weighted sequential splitting.

For all the operator splitting techniques, the different numerical approaches may cause significant numerical errors and splitting errors. The splitting errors are the deviation of the solution obtained by using sub-operators, compared to the solution obtained by using the original operator. The splitting error has been theoretically estimated and more information can be found in [114]. The interaction of splitting and numerical errors can result in a new order of error.

4.5 Openfoam

The modeling of laminar flames and nanoparticle formation was implemented in Openfoam (Open source Field Operation And Manipulation). It is a C++ library that is free and open source under the GNU General Public License. This library is used to solve the partial differential problems describing continuum mechanics, fluid dynamics, financial processes and general multi-physics problems. The functionality of Openfoam includes pre-processing, solving and post-processing, similar to most commercial CFD packages. For pre-processing, Openfoam provides, unstructured mesh generators (*blockMesh* and *snappyHexMesh*) and data manipulation tools (*mapFields* and *transformPoints*). For solving the partial differential problems, libraries and executable are designed in Openfoam to supply numerous capabilities, such as transport and thermophyiscal models, the Lagrangian particle tracking and the discretization of the partial differential equations. Furthermore, the dynamic meshing, the solution of various ODE solvers and the solution of matrix equations with tensor and field operations are available in Openfoam. Different types of boundary conditions are implemented to model geometric constraints (symmetry, empty, wedge and cyclic) and to provide integral parts of the numerical solution (*fixedValue* and *zeroGradient*). By applying the message passing interface (MPI), Openfoam is able to run a large scale problem in parallel on an "unlimited" number of computational cores. For post-processing, the results are saved in formates that can be visualized via ParaView or EnSight. More details about the structure of Openfoam are introduced in the thesis of Jasak [104].

The aforementioned capabilities provided by the library are used to develop applications, which are grouped into solvers and utilities. The solver solves the differential equations combining the problem related models, while the utilities are used to create the mesh, set up the case and post-process the results. Under the C++ framework, library files are compiled separately into a binary executable, known as shared object file, which can be further linked to applications. Therefore, it is possible to implement a new library or solver in Openfoam without recompiling the whole code.

The implementation of a partial differential equation in Openfoam is straightforward: a general transport equation,

$$\frac{\partial \rho \boldsymbol{U}}{\partial t} + \nabla \cdot \phi \boldsymbol{U} - \nabla \cdot \mu \nabla \boldsymbol{U} = -\nabla p$$

is represented in Openfoam syntax as:

```
solve(fvm::ddt(rho, U) + fvm::div(phi, U)
    -fvm::laplacian(mu, U) == -fvc::grad(p));
```

The syntax above starts with "solve", a function that creates and solves the algebraic equation in the form of a matrix. The operators fvm::ddt, fvm::div, fvm::laplacian and fvc::grad represent the time derivative, divergence, laplacian and gradient, respectively, for discretization of the finite volume method. The function fvm stands for the implicit treatment, fvc for the explicit treatment. Moreover, the operator "==" is used in Openfoam to enforce a value assignment on the boundary patches.

Openfoam developments in the present thesis

For the simulation of laminar reacting flows, additional routines for the calculation of species diffusion coefficients were implemented into Openfoam as part of this thesis, which are based on a library provided by Novaresio [118]. In this library, the species diffusion coefficient was calculated based on either a mixture-averaged equation (2.19) or the Stefan-Maxwell equation (2.15). Additionally, the correction velocity (Equation 2.24) was implemented to ensure global conservation of species. The detailed calculation of laminar flames also require an accurate description of the viscosity and the heat conductivity of the gas mixture. Therefore, the formulations proposed by Wilke [28] and by Mathur & Saxena [30] were implemented in the library named *thermophyisicalModels*. Besides the modifications in the libraries, two solvers, namely *myMultiRegionSpFoam* and *modifiedReactingFoam* were implemented to calculate the laminar flame with and without conjugate heat transfer, respectively. With these modifications and implementations, Openfoam can simulate one-dimensional laminar flames as accurately as Cantera (as described in the next section), but lacks grid adaptivity.

4.6 Cantera

One-dimensional, laminar flames can be simulated using Cantera, an open-source reaction kinetics library originally developed in C++ by Goodwin [119]. In Cantera, numerous models for the simulation of chemically reacting systems, such as time-dependent perfectly stirred reactors or laminar, one-dimensional flames are implemented. Cantera covers the calculation of thermodynamic and transport properties of gases using the models described in chapter 2 and the calculation of the finite rate chemistry. Furthermore, models including electrochemical energy conversion and storage, fuel cells, batteries, plasmas and thin film deposition are also implemented.

To run a simulation, the models need to be called via an interface which can be accessed via C++, Python, Matlab or Fortran 90. This interface is a text file, where the employed models, the initial grid, the operation condition, the path for the input reaction kinetics and the solution criteria are defined. Cantera reads the reaction mechanisms in a CTI format, where the species names, the reactions and the corresponding Arrhenius' coefficients, the NASA polynomials for the calculation of thermodynamic properties (heat capacity, enthalpy and entropy) and the Lenard-Jones coefficients for the calculation of transport properties (viscosity, thermal conductivity and diffusion coefficient) are presented in a sequence. Cantera covers the functionality of the popular Chemkin II package using a modern software development paradigm.

For the work in this thesis, the temperature-dependent viscosity and the heat conductivity of pure species were determined by Cantera for a wide range of temperatures and were approximated with 5th order polynomials for use in Openfoam. Furthermore, these data and the reaction mechanisms were converted into a format suitable for Openfoam.

Chapter 5

Validation of the flame and nanoparticle models

The accurate prediction of unperturbed flames is crucial for studies of uncertainties in experiments against presumed one dimensional, ideal models. Furthermore, the formation of nanoparticles highly depends on the temperature and the composition of the gas phase, as well as the residence time that is a result of the flow velocity. Therefore, as an important step towards the investigation of perturbed flames and the synthesis of nanoparticles, the robustness and the reliability of the implemented laminar flame model were verified in this chapter. First the model was validated by one-dimensional burner stabilised flames calculated by Cantera. Two different fuels, methane and hydrogen, were investigated and various chemical mechanisms were employed. The same fuels will also be used later on in section 6. The model was further examined by a simulation of a non-premixed hydrogen flame. The results obtained from the two dimensional simulation were compared against experimental results. At the end of the chapter, Prakash's- and Kruis' model for the synthesis of nanoparticles were verified by a zero dimensional numerical experiment. The simulation results were compared with reference data [120].

5.1 Premixed Flame

The flame model is first tested against 1-D Cantera simulations of premixed hydrogen and methane flames with different equivalence ratios (from lean to rich) under the ambient conditions ($T = 300$ k, $p = 1$ bar). The equivalence ratio of 0.6, 1 and 1.4 are results of the mixture composition as outlined in table 5.1. For the simulations in Cantera, the mass flow rate per unit area at the inlet for all the flames is set to 0.1 kg/m^2s. The corresponding velocity at the inlet used in Openfoam is shown in table 5.1. These simulations were carried out using a quasi one dimensional grid constructed by one cell in lateral direction. The grid extends 3 mm in axial direction containing 800 cells, each with a size of 0.004 mm.

Hydrogen flames have been extensively investigated by many researchers and several reaction mechanisms are available from the literature [32, 121, 122]. The consistency of

Table 5.1: Equivalence ratio, and the corresponding gas composition for the hydrogen flames.

ϕ	X_{H_2}	X_{O_2}	X_{N_2}	U_{in}
0.6	0.375	0.3125	0.3125	0.124
1	0.5	0.25	0.25	0.154
1.4	0.5834	0.2083	0.2083	0.18

those chemical mechanisms for hydrogen flames was checked. A stoichiometric flame (ϕ=1) was calculated using three different chemical mechanisms from Li et al. [32], Burke et al. [121] and Conaire et al. [122]. The calculated temperatures with different mechanisms are in good agreement, as shown in Figure 5.1 (left). Figure 5.1 (right) shows the mole fraction of the intermediate species OH. A discrepancy is found for the mole fraction of OH calculated using the different mechanisms, especially downstream of the flame. However, the magnitude and the position of the peak mole fraction are well predicted. Moreover, an overall good agreement is achieved between results from Openfoam and Cantera.

Figure 5.2 shows the simulated flames with various equivalence ratios using the mechanism from Li et al. [32] to test the implemented flame model. The simulation results calculated by Openfoam agree well with the results obtained from Cantera for all the flames. The results are shown in Figure 5.2 for temperature, velocity, mole fraction of H_2O and intermediate species H. The slight deviation of the H mole fraction may be caused by the different numerical schemes and different numerical implementation of the boundary conditions in the two frameworks. The differences appear at very small concentrations of the species (mass fraction in order of 1×10^{-3} or less), which makes this quantity sensitive to the accuracy of the numerical solution. However, both numerical solvers, implemented in Cantera and in Openfoam respectively are stable and consistent.

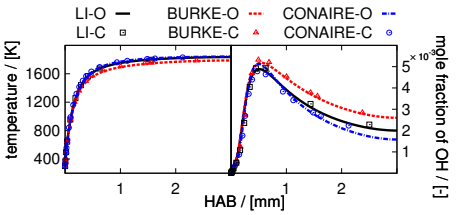

Figure 5.1: Temperature and mole fraction of OH of the simulated stoichiometric H_2 flame using chemical mechanisms from Li et al. [32], Burke et al. [121] and Conaire et al. [122], lines: Openfoam, symbols: Cantera (every 5th point is shown)

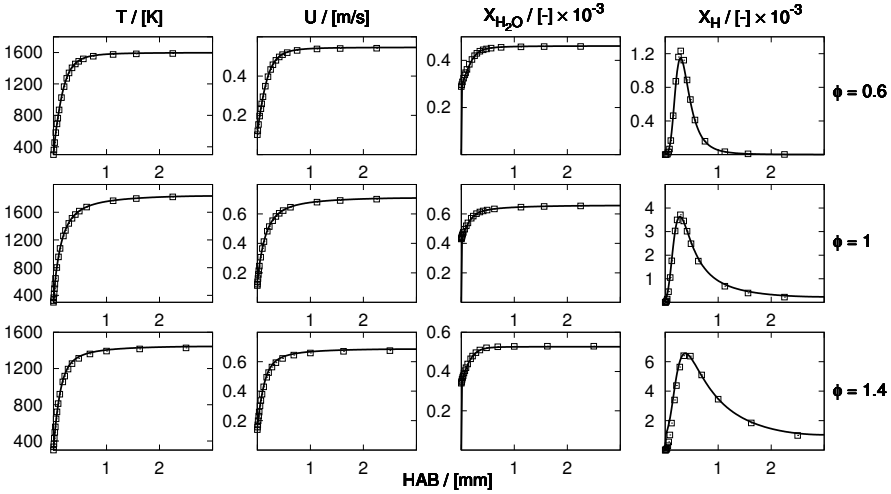

Figure 5.2: Temperature, velocity, mole fraction of CO_2 and H of the simulated H_2 flames with different equivalence ratio using Li's mechanism, lines: Openfoam, symbols: Cantera (every 5th point is shown)

Table 5.2: Equivalence ratio, and the corresponding gas composition for the methane flames.

ϕ	$X_{\mathrm{CH_4}}$	$X_{\mathrm{O_2}}$	$X_{\mathrm{N_2}}$	U_{in}
0.6	0.13	0.435	0.435	0.017
1	0.2	0.4	0.4	0.018
1.4	0.26	0.37	0.37	0.0186

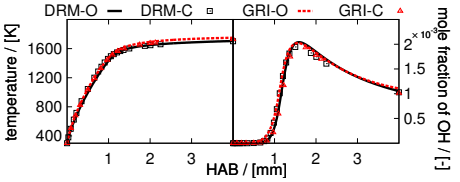

Figure 5.3: Temperature and mole fraction of OH of the simulated stoichiometric CH_4 flame using the chemical mechanisms GRI 1.2 [123] and DRM [124], lines: Openfoam, symbols: Cantera (every 5th point is shown)

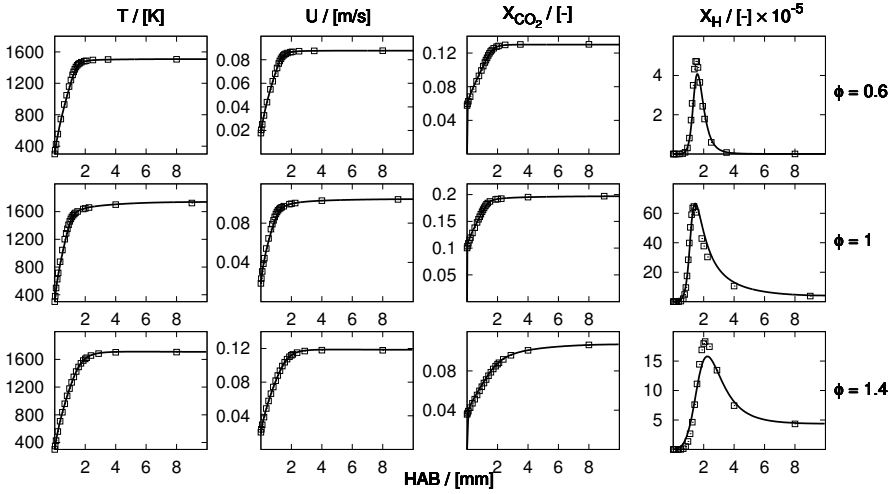

Figure 5.4: Temperature, velocity, mole fraction of CO_2 and H of the CH_4 flames with different equivalence ratios using the DRM mechanism, lines: Openfoam, symbols: Cantera (every 5th point is shown)

Table 5.2 shows the composition and the inlet velocity of the simulated methane flames. The numerical grid had a length of 10 mm and contained 3200 cells with a cell size of 0.003 mm. The well-defined GRI 1.2 mechanism [123] and its reduced version DRM [124] were used. As shown in Figure 5.3, simulation results with different mechanisms are similar. The results calculated by Openfoam are compared with those predicted by Cantera, and good agreement is achieved with respect to the profiles of temperature, axial velocity and mole fractions of CO_2 and H. Nevertheless, the aforementioned difference of the numerical implementations account for slight deviations.

5.2 Non-Premixed Flame

The second test-case is a non-premixed atmospheric, laminar $H_2\backslash O_2\backslash N_2$ flame, which was investigated experimentally and numerically by Toro et al. [125]. The solution of a hydrogen flame is highly sensitive to the quality of the laminar flame models, because the fast reactions and the high diffusion of atomic hydrogen occur at the same time. In addition, compared to the simulation of other flames, the detailed mechanism of the hydrogen flame is small in the size of species and reactions, and requires relatively low computational effort. Therefore, this flame was chosen to validate the model implementations in a 2-D simulation.

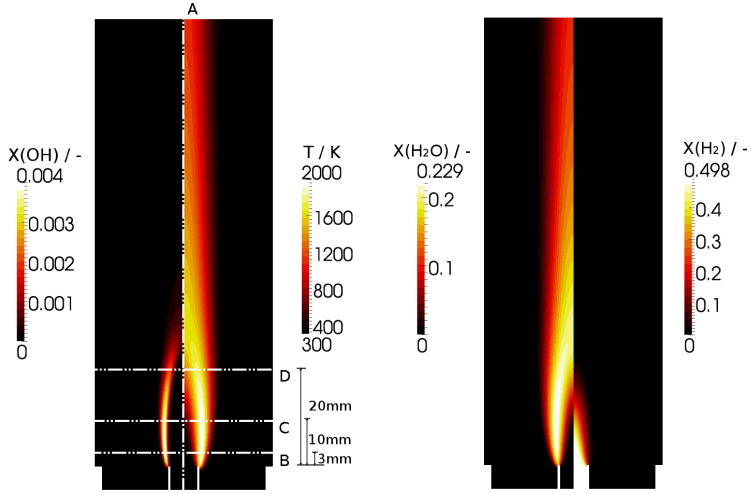

Figure 5.5: Contour plot of the simulated non-premixed flame, left: Distribution of mole fraction of OH and temperature, right: distribution of mole fraction of H_2O and H_2.

In the experiment, the flame was stabilised above a burner that supplies the fuel stream surrounded by the coflow air. The fuel was a mixture of hydrogen and nitrogen (1:1), which was provided through a stainless steel tube with an inner diameter of 0.9 cm. The air coflow annulus had an inner diameter of 9.5 cm. Both fuel and coflow exited the burner with the same velocity. In the work of Toro et al. [125], flame structures were studied with the exit velocity of 18 cm/s, 27 cm/s and 50 cm/s individually, where in this work the flame with the velocity of 50 cm/s was replicated. The mole fraction of stable species was measured with spontaneous Raman scattering, whereas the temperature was measured with spontaneous Raman Scattering and coherent anti-Stokes Raman scattering individually, and a good agreement was achieved between these two methods. The measurements were carried out along centerline and radial lines at varied distance above the burner.

The simulation domain used in this work (Figure 5.5) extended downstream of the jet exit for 14 cm to ensure a fully developed flame. Upstream of the jet exit, 0.8 cm were included in the domain, a sufficient length to obtain the velocity profile at the jet exit. The computational grid consisted of 15,600 cells. To check the convergence of the solution, the simulation was repeated on a coarse mesh consisting of 8000 cells and nearly the same simulation results were obtained. Due to the fact that in the experiment the fuel stream was diluted in mole ratio (H_2:N_2 = 1:1) to decrease the heat loss from the flame to the burner, the burner outer surface was assumed to be adiabatic. Unlike the simulations performed by Toro et al. [125], the radiation and the thermal diffusion of species were not taken into account in our model.

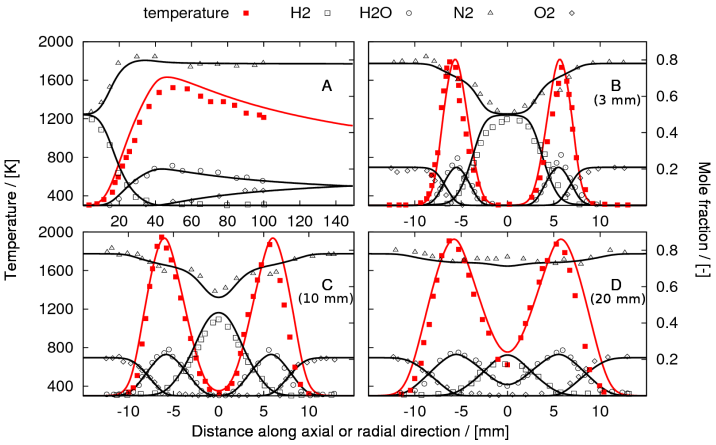

Figure 5.6: Comparison between the simulation results (lines) and the experimental measurements (symbols) along the centerline and the radial lines at 3 mm, 10 mm and 20 mm above the burner.

Figure 5.5 shows the 2-D contour plots for the temperature and the mole fraction of OH, H_2O and H_2. As observed in the experiment, the flame is stabilised above the burner (see mole fraction of OH). The H_2 and O_2 are fed into the reaction zone where the mixing and the combustion take place simultaneously. The main product of the combustion, H_2O, is produced in the flame and shown in Figure 5.5 (right). The highest temperature of the gas phase is nearly 2000 K. The simulation results along four sampling lines (indicated by blue lines in 5.5) are presented in Figure 5.6. Experimental results are compared against the simulation results in terms of the temperature and the mole fraction of stable species (H_2, O_2, N_2 and H_2O). A good agreement is achieved, although the measured temperature axial profile drops slightly faster than the simulated one. Nevertheless, as aforementioned, the radiation effect, which may contribute to the additional heat loss from the flame, was not taken into account in the simulation.

5.3 Test for Nanoparticle synthesis

In the last test case, the nanoparticle synthesis models were tested via an artificial zero dimensional simulation for the synthesis of TiO_2. This test case was originally carried out by Spicer et al. [120] to validate a moving sectional model. The simulation was conducted at atmospheric pressure for different temperatures ranging from 1000 to 1800 K. Further, different initial volume fractions of a mixture of $TiCl_4$ and O_2 were set from 0.001 to 0.5. This test case originally aimed to investigate the impact of the gas phase and surface oxidation of $TiCl_4$ on the particle formation. For the validation of the implemented Prakash-model, to simplify the reaction model only the gas phase oxidation was considered and the surface oxidation was neglected. The formation of TiO_2 from the reaction of $TiCl_4$ and O_2 was described by a one-step mechanism:

$$TiCl_4 + O_2 \longrightarrow TiO_2 + 2\,Cl_2 \tag{5.1}$$

The reaction rate of the reaction above is calculated as:

$$\frac{dC}{dt} = -kC \tag{5.2}$$

The concentration of $TiCl_4$ is denoted by C and the overall oxidation rate constant k is written as [90]:

$$k = 8.26 \times 10^4 \exp\left(\frac{-10,681}{T}\right) \tag{5.3}$$

Figure 5.7 shows the particle size distribution (PSD) under the operating condition $T = 1400K$ and $\phi = 0.1$ for varied time instances. The simulations employing Prakash's model were performed individually using 10, 30, and 50 bins with a diameter spacing factor of 3, 1.5 and 1.2, respectively. Even with different resolutions, the simulations indicate a similar trend at the different time instances. At the initial stage, a large number of monomers

(TiO_2) are formed from the gas-phase oxidation of $TiCl_4$. Particles grow and form a bimodal distribution after $t = 0.01s$, due to the coagulation. The particle continues growing in size and a self-preserving form is reached at $t = 1s$. The calculated PSD becomes accurate with an increasing number of bins and a decreasing space ratio, but leads to an increased computational cost as well. The simulation results using 50 bins shows the best agreement compared to the reference results by Spicer et al. [120], where the same space ratio for the bins is used.

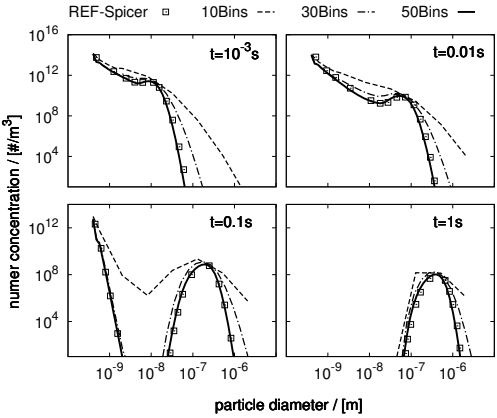

Figure 5.7: Particle size distribution at different time for $T = 1400$ K and $\phi = 0.1$

In order to test the sensitivity of the simulation results to the spacing ratio, simulations using 50 bins with slightly changed spacing ratios (1.2 "$+/-10\%$") were performed. As shown in Figure 5.8, the deviation of the PSD using varied spacing ratios are noticeable. It should be stressed that for the calculation of the PSD using Prakash's model, the spacing ratio needs to be carefully chosen (sufficiently low) to obtain a convergent solution.

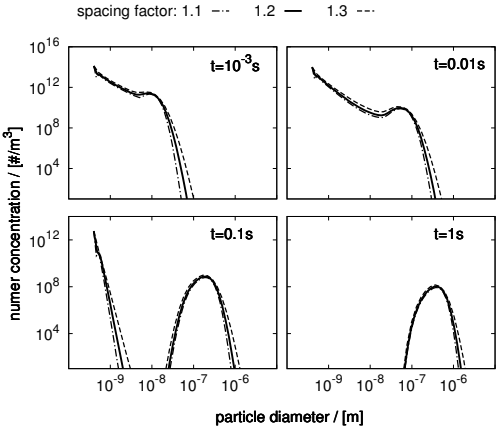

Figure 5.8: Particle size distribution for $T = 1400K$, $\phi = 0.1$ using 50 bins accounting for diameter spacing factors of 1.1, 1.2 and 1.3.

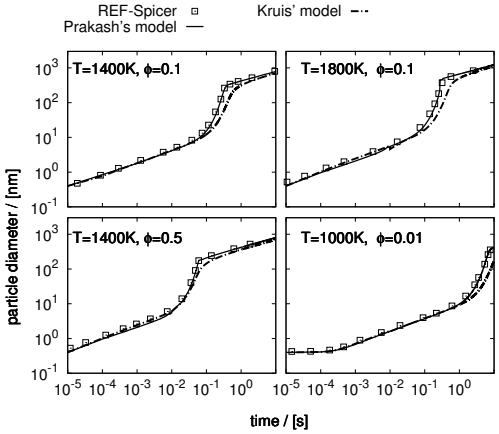

Figure 5.9: Evolution of the volume-based average diameter of particles for $T = 1400$ and $\phi = 0.1$, square points: reference simulation results by Spicer et al. [120], black lines: simulation results using Prakash's model with 10 bins at the spacing ratio of 3, dashed lines: simulation results using Kruis' model, where the sintering effect is not taken into account.

Figure 5.9 shows a comparison between Kruis' model and Prakash's model using volume-based average particle diameters from the simulations with different temperatures and equivalence ratios. It is an interesting finding that even coarse bins yield the same profile of the average diameter of the particles as fine bins. All the simulation results agree with the reference data. It seems that the time evolution of the average particle diameters is robust against the setting of bins. A second sharp increase of the particle size is observed for all the presented cases. Compared to other cases, with a low temperature and concentration of $TiCl_4$ ($T = 1000$ K, $\phi = 0.01$), the increase of the average particle diameter becomes slow and the sharp increase take place after 1 s. Although Kruis' model predicts similar results as Prakash's model for small particle sizes up to 10 nm, Kruis' model underpredicts the particle size when particles grow sharply. Nevertheless, for the investigated case in sections 7.5 and 7.3, the formed particles have a limited size ranging from 0.5 to 10 nm. Therefore, Kruis' model is still suitable there.

As a summary for this chapter on the validation of the flame model, the simulation results of Openfoam were first compared against the 1-D Cantera calculation of premixed flames. The overall agreement suggested the reliability of the detailed calculation of chemistry using Openfoam. It was interesting to notice that for the calculation of the hydrogen flames, even well-established reaction mechanisms [32, 121, 122] predicted fairly different profiles of OH downstream of the flame. Due to the computational efficiency of the mechanism proposed by Li et al. [32], this mechanism was chosen for further simulations of hydrogen flames. In the second step, the flame model was further tested against the experimental data of a non-premixed hydrogen flame, where the transport behavior of the gas phase species required detailed description. A satisfactory agreement between the simulation results and the experimental measurements gave evidence that the mixture-averaged models mentioned in Chapter 2 were well implemented in Openfoam. In the last step, the monodisperse model (Kruis' model) and the sectional model (Prakash's model) were validated against the artificial case for TiO_2 synthesis designed by Spicer et al. [120]. Compared to the reference data obtained by Spicer et al. [120], both Kruis' model and Prakash's model implemented in Openfoam provided similar results. Although Kruis' model underpredicted the particle size once the particles became bigger than 10 nm, Kruis' model is still suitable for the simulation of nanoparticle synthesis reactors later on, since the investigated nanoparticles were limited to the size range $0.5 \sim 10$ nm.

Chapter 6

Uncertainties in the experiment

Experimental uncertainties and errors affect the findings from experiments. For example in a the flame reactor, the flame can be affected by the intrusive measuring techniques (thermocouple, sampling probe) at low HAB. Furthermore, the geometric configuration of the reactor may modify the flow field and heat transfer may occur between the reactor housing and the flame. In most cases, these errors are hard to be reduced, but often, they can be quantified and corrected by a detailed calculation.

This chapter first presents a mass spectrometry sampling technique for premixed, atmospheric flames, where the sampling nozzle affects the flame, as well as the perforated burner plate that may cause the non-ideality of the 1-D assumption. A short introduction of a premixed flame within a low pressure reactor is given in section 6.2. Here a mass spectrometry sampling technique similar to the one in the first experiment is applied and the buoyancy effect becomes crucial for the investigated operating condition. In section 6.3, the probing nozzle effect on the early iron particles is discussed. The section 6.4 shows the experimental setup for the investigation of soot particles, in which the sampling orifice in the center of the stagnation plate may notably perturb the flow. In the last section, several measuring techniques used in the study of silicon-dioxide particle synthesis, as well as the discontinuity of the measured temperature caused by the reactor housing, are introduced.

6.1 Effect of alignment of sampling nozzle and perforated plate on the ambient flame [22]

This section was previously published in 'Combustion and Flame, 162 (5), L. Deng, A. Kempf, O. Hasemann, O. P. Korobeinichev and I. Wlokas, Investigation of the sampling nozzle effect on laminar flat flames, 1737-1747 (2015)' and is reprinted with permission. The author L. Deng implemented the detailed models for viscosity and thermal conductivity of the gas phase and diffusive transport of species and a solver coupling the conjugate heat transfer to a reactive gas flow, ran all simulations, wrote the paper and generated all figures. The author O. Hasemann generated the reduced mechanism. The author O. P. Korobeinichev provided the experimental results and contributed discussions and proof-reading. The authors A. Kempf

and I. Wlokas contributed guidance, corrections, discussions and proof-reading.

For the study of the flame structure, gas samples are usually taken by a sonic quartz nozzle, which is inserted into the region of interest of the flame. In a typical experiment, the burner is moved in the axial direction, relative to the sampling nozzle, to measure spatially resolved concentrations of every species as a function of height above the burner (HAB). However, the technique is invasive and the sampling nozzle does affect the flame, so further calibration and additional measurements of temperature are needed to preserve the precision of the experiment.

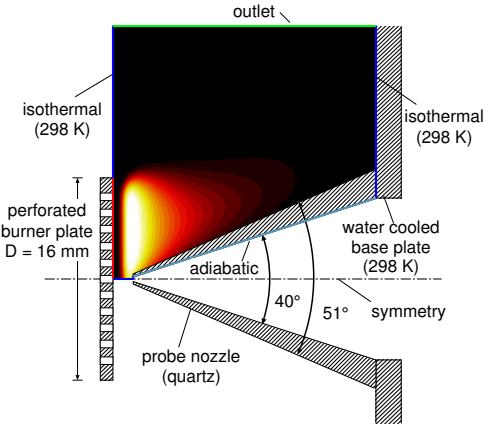

Figure 6.1: Sketch of the experimental setup used by Korobeinichev et al. [13]. The OH concentration field indicates the shape and location of the methane flame and the extension of the computational domain. Image is not exactly to scale. Reprinted with permission [22].

It is important to examine what is already known about the continuous sampling of a flame at $\sim$ 2000 K through a small orifice into a mass spectrometer. The fact that there has to be sonic flow, with a Mach number of unity, in the narrowest part of the orifice leads to a considerable cooling (by up to 300 K) of the sample [14, 126]. However, before reaching the inlet hole, the flame gases have to move close to the tip of the relatively cool sampling nozzle and consequently there is a further cooling of the sample in thermal boundary layers [127, 128, 129]. This cooling is bigger for a smaller orifice [130], but has been measured to be as much as 400 K [129, 130]. After passing through the orifice, the sample expands supersonically and almost adiabatically [126] in the first vacuum chamber, where the temperature can fall to $\sim 400 - 500$ K before collisions cease.

Interestingly the cooling in the supersonic expansion is greater for a larger inlet orifice [130]. The residence times in the thermal boundary layer and supersonic expansion are

both of the order of 0.1 μs [131], so that ionic reactions like $HCl + e^- = H + Cl^-$ and $NH_4^+ + H_2O = NH_4 + H_2O$ [132] are fast enough to be equilibrated in the flame, in the thermal boundary layer and also in the earliest part of the supersonic expansion. In these cases the mass spectrometer measures ratios of ion concentrations for the point, where an equilibrium freezes. It appears that boundary layer cooling dominates for inlet orifices smaller than $100 - 150$ μm in diameter, but for larger orifices the cooling is entirely in the supersonic expansion. For these larger inlet orifices other effects such as scattering in the first chamber can be important [133]. In addition to the sample being cooled by a probe, there is a disturbance to the flame's flow field [134, 135].

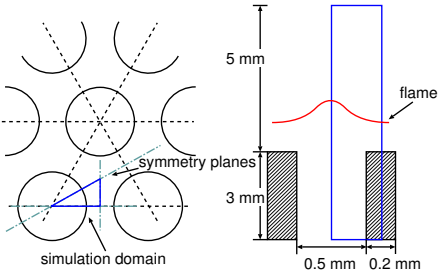

Figure 6.2: The perforated plate of the burner, and the computational domain for simulation of the flow through the plate. Reprinted with permission [22].

Smith [136] examined the sampling nozzle's effect on an H_2/O_2/Ar flame, doped with HCN by measuring the concentration of the CN radical using probes with differently sized orifices. In order to quantify the gas dynamic effect of the sampling nozzle, Yi and Knuth [137] expressed the shift in concentration profiles as a function of the orifice diameter, the Reynolds number and the Schmidt number. However, due to the complexity of the sampling system, an accurate prediction of all the effects could not be obtained. Alongside these theoretical studies, many experiments have been conducted to analyze the problem [138, 23, 139, 140]. An investigation on the interaction of a sampling probe on a narrow flame by Korobeinichev et al. [138] confirmed the need for a detailed study of the probe effects. Thus, based on their work, Korobeinichev et al. [138] suggested a semi-empirical relation for the point of sampling being shifted in the axial direction to compensate for the probe effects. The effects of a sampling nozzle on the structure of a low-pressure flame were studied by Hartlieb et al. [23], who measured the concentrations of OH and NO using laser-induced fluorescence. Struckmeier et al. [139] have focused on the cooling of a flame gas by a sampling probe at different axial positions along a flat, premixed, low pressure flame. Recently, Skovorodko et al. [140] have presented a numerical study of probe-induced perturbations of a CH_4/O_2/Ar flame for comparison with experimental measurements by Korobeinichev et al. [13]. They used a finite difference method, a heat source model, and

the measured temperature of the probe surface.

Furthermore, the perforated plate on which the flame was stabilized can also cause deviations from perfect one-dimensionality, especially near the burner. Several groups have examined the flow through plates, perforated to generate turbulence [141, 142, 143]. Somers and de Goey [144] completed a two-dimensional numerical study to consider perturbations originating from holes with different diameters for a stoichiometric methane-air flame. In the context of the heat flux method for measuring flame speeds, Bosschart and de Goey [145] have investigated a perforated plate burner. Recently, Konnov et al. [146] investigated 2-D effects in a flat flame burner by means of computational fluid dynamics, but the burner plate was modeled as a porous plug.

In the present work, the setup of Korobeinichev et al. [13] and Knyazkov et al. [147, 148] was analyzed for the burning of a $CH_4/O_2/Ar$ flame and another of $H_2/O_2/N_2$. These measurements, used to verify the simulation methods employed, were made at atmospheric pressure which is exceptionally high for this type of diagnostic.

The experimental setup for the methane flame is shown in Figure 6.1. A similar setup was operated for the hydrogen flame. This set-up used an axis-symmetric quartz sampling probe with a tip diameter of 0.24 mm and an orifice diameter of 0.08 mm, which is sufficiently small for any effects of the supersonic expansion to be ignored [1]. The conical probe had inner and outer angles of 40° and 51° respectively and was fixed to a water cooled base plate. For the methane flame measurements, the distance from the burner surface to the probe was varied from 0.17 mm to 3.59 mm. The diameter of the burner plate was 16 mm and the velocity of the unburned gas was 0.157 m/s at a temperature of 368 K. The mole fractions of $CH_4/O_2/Ar$ were 0.06/0.15/0.79, corresponding to an equivalence ratio of $\Phi = 0.8$ and resulting in an adiabatic flame temperature of 1855 K. For the hydrogen flame experiment, burner distances from 0.4 mm to 2.8 mm were considered. The diameter of the burner plate was 24 mm and the velocity of the unburned gas was 0.425 m/s at a temperature of 333 K. The molar composition of 0.165/0.075/0.76 for $H_2/O_2/N_2$ yields an equivalence ratio of $\Phi = 1.1$ and an adiabatic temperature of 1476 K. Both burners were open to the atmosphere and an ambient pressure of 101325 Pa was assumed for the simulations. The orientation of the burners was 'upright'.

The perforated plate, 3 mm thick, had holes of 0.5 mm in diameter, spaced 0.7 mm apart center to center, as shown in Figure 6.2. The region upstream of the perforated plate was filled with 3 mm (diameter) metal beads to homogenize the flow. The perforated plate and the computational domain are sketched in Figure 6.2.

The simulation results of adiabatic, one-dimensional, laminar flame models, as implemented e.g. by PREMIX [44] or Cantera [119] cannot capture the effect of the sampling nozzle and have therefore shown a clear deviation from the measurements. The present study applies a detailed simulation to determine the effect of the sampling nozzle on the flame and to explore whether a bias is induced by the perforated plate on the burner's face. In addition, a simulation work-flow is suggested for the detailed calculation of perturbed laminar flames in order to enhance the interpretability of experimental measurements, obtained from mass spectroscopy with molecular beam sampling.

6.2 Effect of buoyancy and sampling nozzle in a low pressure flame reactor

The work in this section is going to be submitted to the journal Combustion and Flame. L. Deng developed the code and the flame model and ran all simulations. Y. Karakaya from the Chair of Thermodynamics, Institute for Combustion and Gas Dynamics, University Duisburg-Essen conducted the experiments.

Another experiment using the sampling mass spectrometry on the $CH_4/O_2/Ar$ flames was conducted at the Chair of Thermodynamics, Institute for Combustion and Gas Dynamics, University Duisburg-Essen. They used a McKenna type burner, installed in a low-pressure housing. The burner diameter is 60 mm, the operating pressure was set to 16 kPa. The orientation is upwards. The reactor consists of a combustion-, an expansion- and an analysis chamber, each with a diameter of 250 mm.

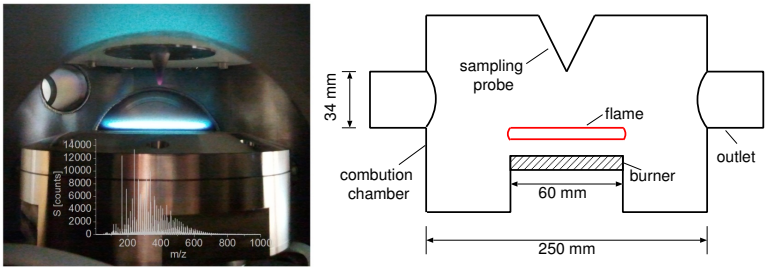

Figure 6.3: The low pressure flame reactor (left), and a sketch of the combustion chamber (right).

Figure 6.3 illustrates the combustion chamber of the reactor, containing optical windows, vacuum pump connection and four exhaust gas outlets. In addition, a sampling nozzle was mounted at the top of the combustion chamber to extract the gas samples at different HAB. This probe was made of nickel, with a thickness of 0.2 mm. The distance between the burner and the probe can be varied in a range of $0 - 300$ mm. Through the orifice (0.55 mm in diameter) of the nozzle, the molecular beam was formed in the expansion chamber and passed to the mass spectrometer. In the present work, the mentioned experimental setup was used for the analysis of flames with an equivalence ratio of 0.8, 1 and 1.2 individually. For all the flames, the fresh gas was fed into the burner at a flow rate of 4 standard liter per minute (slm). The flow rate for mixture components is shown in table 6.1.

As illustrated by Weise et al. [149], the design of a reactor for nanoparticle synthesis is normally very straightforward. However, the fluid dynamic and thermodynamic processes within the reactor are complex and may modify the flow- and temperature fields. Therefore,

Table 6.1: Equivalence ratio, and the corresponding flow rate for mixture components.

ϕ	CH_4[slm]	O_2[slm]	Ar[slm]
0.8	0.57	1.43	2
1	0.67	1.33	2
1.2	0.75	1.43	2

2D/3D CFD simulations are required to evaluate the influence from the fluid dynamic and thermodynamic processes.

The simulations showed that also in the upward-giving configuration, buoyancy affects the flow field, especially at large heights above the burner, which are of interest for particle forming flames. The probing effect, as mentioned in the studies of flame structure, has to be considered in the simulation. Details of the simulation and the results are presented in section 7.2.

6.3 Effect of alignment of sampling nozzle on the formation of early iron particles [12]

This section was previously published in 'CrystEngComm 17 (36), S. Kluge, L. Deng, O. Feroughi, F. Schneider, M. Poliak, A. Fomin, V. Tsionsky, S. Cheskis, I. Wlokas, I. Rahinov, T. Dreier, A. Kempf, H. Wiggers and C. Schulz, Initial reaction steps during flame synthesis of iron-oxide nanoparticles, 6930-6939 (2015)' and figures are reprinted with permission. The author L. Deng developed the detailed models for viscosity and thermal conductivity of the gas phase and diffusive transport of species, ran all simulations and generated parts of the figures. The author S. Kluge conducted the PMS and QCM measurements for the Duisburg reactor, wrote the paper and generated most parts of figures. The author O. Feroughi conducted the LIF measurements for the Duisburg reactor. The authors F. Schneider, M. Poliak, A. Fomin and V. Tsionsky conducted the experiments for the Tel Aviv reactor. The authors S. Cheskis, I. Wlokas, I. Rahinov, T. Dreier, A. Kempf, H. Wiggers and C. Schulz contributed guidance, corrections, discussions and proof-reading.

Investigation of iron-oxide nanoparticles is important for researchers due to their wide range of application, including optical magnetic recording, magnetic resonance imaging, gas sensors, and bioseperation. Interested readers are referred to the review article of Lu et al. [150]. Flame-assisted synthesis is an attractive way to produce iron-oxide nanoparticles with tailored particle properties. It provides many advantages, e.g. high production rate, great purity of the product and most importantly, an easily scalable route to large-scale industrial production [151, 152].

Many research groups worldwide investigated the effects of combustion conditions on the formation of iron-oxide nanoparticles. Janzen et al. [153] studied the effect of the different amount of precursor loadings on the formation of iron-oxide nanoparticles. In their work,

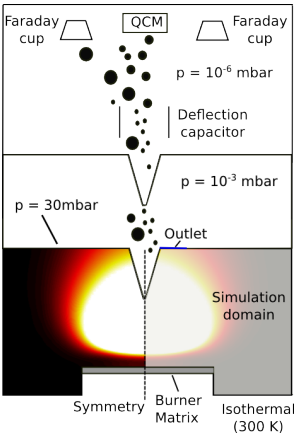

Figure 6.4: Experimental setup of Duisburg reactor.

nanoparticles in a size region of 4-12 nm were synthesized in a low pressure, premixed $H_2/O_2/Ar$ flame. Zachariah and coworkers [154] operated a premixed $CH_4/O_2/N_2$ flame doped with two different precursors to obtain silicon coated iron-oxide nanoparticles. Besides premixed synthesis flames, several studies were performed using non-premixed flames as well. Buyukhatipoglu et al. [155] investigated the effects of flame temperature, additive loading and flame configuration on the size of iron-oxide nanoparticles formed inside a methane diffusion flame. In the work of Kumfer et al. [156], the flame was fed by an injection of oxidizer into a surrounding hydrocarbon fuel. They explored the temperature effect on the particle size by varying the stoichiometric mixture fraction.

Recently, early iron particle formation has been observed by Feroughi et al. [157] and Poliak et al. [18] in a non-premixed and a premixed $Fe(CO)_5$ doped CH_4/O_2 flame, respectively. The study of Feroughi et al. [157] proposed a reaction mechanism combining iron-oxide formation by Wlokas et al. [91] and iron-cluster formation by Wen et al. [158]. This mechanism was also used in the work of Poliak et al. [18], where they measured the deposition of particulate material using a PMS combined with a quartz crystal microbalance (QCM). Their measurements were qualitatively confirmed by one-dimensional simulations of the doped flame.

This work presents methods to investigate the initial steps toward the particle formation. Two reactor systems were investigated using several measurement techniques to obtain extensive information for the validation of CFD simulations and the kinetic model of the precursor. For the first reactor system, the Duisburg reactor (DU-R), the mass flow rate of condensed material, the temperature and the iron atom concentration were measured by QCM, NO-LIF thermometry and laser-induced fluorescence (LIF), respectively. In the

Kluge et al. CrystEngComm (2015), figures are reprinted with permission.

second reactor system, the Tel Aviv reactor (TA-R), in addition to the PMS measurement for the mass flow rate, the temperature was measured by OH-LIF and the concentration of FeO by intra-cavity laser absorption spectroscopy (ICLAS).

A water-cooled sintered matrix was placed in the DU-R of 100 mm in diameter with four windows that provide optical accesses for the LIF measurement. To extract the gas samples, a sampling nozzle was used, which was made of nickel (BeamDynamics model 2) with a 0.5 mm orifice. The bottom-to-top flame was fed by the fresh gas (400 sccm H_2, 400 sccm O_2 and 600 sccm Ar), leading to an equivalence ratio of 0.5 at a pressure of 3000 Pa. In the TA-R, a top-to-bottom flame was burnt on a McKenna burner with a diameter of 60 mm. A stainless steel sampling nozzle with a 0.5 mm orifice was used here. The fresh gas, constituting of 450 sccm CH_4, 900 sccm O_2 and 1-51 sccm N_2 was injected into the burner at a pressure 4000 pa. For the both reactor systems, part of the argon was replaced by $Fe(CO)_5$ to add precursor into the flame. The precursor concentration was varied between 0-200 ppm for DU-R experiments and 20-920 ppm for Tel Aviv experiments. The setup and the working strategy of LIF measurement will be described in subsection 6.5.

Numerical simulations were conducted to consider the impact of the geometric configuration of the reactor and the sampling nozzle on the flame, and further on the evolution of nanoparticles. The monodisperse model was used to simulate formation and growth of the iron-oxide particles. The simulation results were compared with the experimental data to enhance the interpretability of the experimental measurements. Section 7.3 discusses the simulation and the results of the described experimental configurations.

6.4 Effect of stagnation-plate and sampling orifice on an ambient flame [159]

Most parts of this section were previously published in 'Combustion and Flame 162 (10), J. Camacho, C. Liu, C. Gu, H. Lin, Z. Huang, Q. Tang, X. You, C. Saggese, Y. Li, H. Jung, L. Deng, I. Wlokas and H. Wang, Mobility Size and Mass of Nascent Soot Particles in a Benchmark Premixed Ethylene Flame, 3810-3822 (2015)' and figures are reprinted in chapter 7 with permission. The author L. Deng implemented the detailed models for viscosity and thermal conductivity of the gas phase and diffusive transport for species, ran all CFD simulations and 1-D Cantera simulations and generated parts of the figures. The author J. Camacho conducted the experiments at University Stanford, wrote the paper and generated most parts of figures. The author C. Liu conducted the experiments at Stanford University. The authors C. Gu and H. Lin conducted the experiments at Shanghai Jiao Tong University. The authors Q. Tang conducted the experiments at Tsinghua University. The author C. Saggese ran all 1-D OPPDIF simulations. The author Y. Li conducted the experiments at University of California Riverside. The authors Z. Huang, X. You, H. Jung, I. Wlokas and H. Wang contributed guidance, corrections, discussions and proof-reading.

For the investigation of soot particle formation in the premixed laminar flame, an often used facility [160, 15, 161, 162] is a combination of burner stabilized stagnation (BSS) flame, micro-orifice probe sampling and scanning mobility particle sizer (SMPS). The burner setup

is shown in Figure 6.5, where the flame burns on a water-cooled burner towards a circular plate cooled by water. In the center of the plate, a micro-orifice is drilled for sampling. The boundary condition of the flame can be fully specified, since the plate acts as a stagnation surface downstream the flame. In this way, the flame can be simulated using one dimensional tools, such as OPPDIF [163], PREMIX [44] and Cantera [119], which in turn enables a direct comparison between the simulation results and the measurements. The combination of BSS flame and SMPS provides valuable data for understanding chemical and physical processes of soot particle formation and further contributed to refined theoretical and experimental modeling.

Figure 6.5: The burner stabilized flame and the stagnation plate with a sampling orifice in the center (from the University of Stanford).

The target flame was the benched flame (Flame C3 [161]) at atmospheric pressure, burning the fresh gas (16.3% C_2H_4, 23.7% O_2 and 60% Ar) with an equivalence ratio of 2.97. The fresh gas was fed into the burner with a velocity of 8 cm/s at standard conditions (298 K and 1 atm), whereas a shroud of nitrogen with a velocity 43.6 cm/s was injected to isolate the flame from the ambient air. In the laboratory at Stanford, the measurements dependency on the burner size was first checked by two different burner diameters (5 and 7.6 cm). As no significant difference was observed, further measurements (see section 7.4) were conducted using the burner with a diameter of 5 cm. The material for the outer body was brass, whereas the plug plate was made of bronze. The plug was a porous plate with a pore size of 20 μm and a thickness of 1.3 cm. In order to specify the temperature boundary condition at the burner and the stagnation surface for the numerical modeling, a thermocouple with a wire diameter of 130 μm and a bead size of 300 μm were used. The thermocouple surface was coated with a mixture of Y/BeO to prevent surface catalysis. Radiation correction was taken into account following the procedure of Shaddix [164]. The uncertainty in the corrected temperature at the lowest measured temperature was around

Camacho et al. Combust. Flame (2015), figures are reprinted with permission.

±5 K, whereas the uncertainty may reach ±90 K at the peak temperature. The temperature at the burner surface was obtained via extrapolation of the axial temperature data towards the burner surface, where the closest distance to the burner surface was the radius of the thermocouple bead.

The flow stagnation surface used here is an aluminum disc (8 cm in diameter and 1.3 cm in thickness), in which a stainless steel tubular sampling probe with a thin-wall (0.635 cm) was embedded. The disc was water cooled and the temperature of the stagnation surface was measured by a type-K thermocouple. For the measurement, the stagnation surface can be moved along the axial direction of the flame as a function of HAB with an accuracy of ±0.025 cm. The soot samples were extracted from the flame through the sampling orifice with a diameter of 127 μm, and they were rapidly diluted with a cold flow of nitrogen at 30 L/min (298 K and 1 atm) to reduce particle coagulation. The pressure-drop across the orifice controls the flow rate into the orifice and was measured by two manometers upstream and downstream of the sampling orifice. Furthermore, the dilution ratio was given as a function of the pressure drop.

The described sampling method was applied on the same flame in Stanford, Tsinghua and Shanghai Jiao Tong universities. Here, two dimensional CFD simulations were conducted based on the Stanford experiment to evaluate the impact from the sampling orifice on the flame and further on the measurement. Due to the pressure drop across the sampling orifice, the velocity through the orifice under dilution increases by a factor of 100 and a spherical volume of the sampling zone is formed in the vicinity of the orifice. Hence, the flow field and the temperature can be highly influenced. Two dimensional CFD simulations were carried out to understand the nature of the sampling method and to examine how strong it affects the boundary condition of the one dimensional stagnation flame formulation. In section 7.4, detailed discussions and suggestions are given by the comparison of experimental- and simulation results with the consideration of the probing effect.

6.5 Effect of geometric configuration of the reactor on the flame [25]

This section was previously published in 'Proceedings of the Combustion Institute, O. M. Feroughi, L. Deng, S. Kluge, T. Dreier, H. Wiggers, I. Wlokas and C. Schulz, Experimental and numerical study of a HMDSO-seeded premixed laminar low-pressure flame for SiO_2 nanoparticle synthesis (2016)' and figures are reprinted with permission. The author L. Deng implemented the detailed models for viscosity and thermal conductivity of the gas phase and diffusive transport of species and Kruis' model, ran all simulations and generated parts of the figures. The author O. M. Feroughi conducted the LIF measurements, wrote the paper and generated most parts of figures. The author S. Kluge conducted the PMS measurements. The authors T. Dreier, H. Wiggers, I. Wlokas and C. Schulz contributed guidance, corrections, discussions and proof-reading.

Feroughi et al. Proc. Combust. Inst. (2016), figures are reprinted with permission.

The synthesis of silicon dioxide (SiO_2) nanoparticles was studied in a lean $H_2/O_2/Ar$ flame doped with hexamethyldisiloxane (HMDSO). The properties of nanoparticles depend on the temperature of the flame, since it is strongly related to thermo-decomposition of the precursor and to the particle formation, and therefore of great interest. In the current work, the temperature of the gas-phase was measured by multi-line NO laser-induced fluorescence (LIF). For the measurement, a small amount of NO (around 100 ppm) was doped in the flame with negligible influence on the flame chemistry.

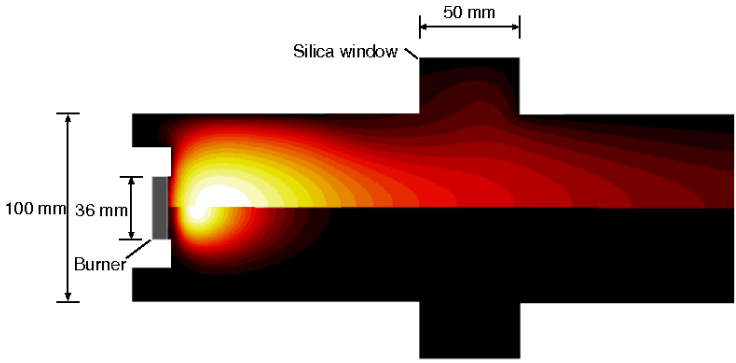

Figure 6.6: Configuration of the flame reactor. Distribution of the temperature (top) and the mole fraction of OH (bottom).

An important intermediate species during the formation of SiO_2 particles is SiO, which is formed after the decomposition of the precursor and the nucleation and formation of the particles. Since this intermediate links the gas-phase chemistry and the particle formation and growth, the measured SiO concentration serves as a valuable input for the development of models and the simulation validation. A series of studies [165, 166, 167, 168, 169, 170, 171] has been conducted focusing on the SiO LIF measurement during different chemical and physical processes (e.g. dry oxidation, chemical vapor deposition and flame assisted synthesis) of particle formation in various material systems. For this work, LIF excitation emission measurement for SiO was carried out on the $H_2/O_2/Ar$ flame mentioned above, following the procedures introduced in [172]. The size distribution of SiO_2 particles was measured by PMS using molecular beam sampling. This PMS system has been established and successfully used for the previous studies [173, 12] for the measurement of particle size distributions in low pressure flame.

As illustrated in Figure 6.6, within a cylindrical reactor (300 mm in length and 100 mm in diameter), an $H_2/O_2/Ar$ flame was stabilized on a water-cooled sintered stainless-steel burner with a diameter of 36 mm at a pressure of 3 kPa. The flame was sustained by a feeding of 700 sccm H_2, 900 sccm O_2, 300 sccm Ar and 200 ppm of HMDSO, leading to an equivalence ratio of 0.39 and a gas velocity of 1m/s. The burner head can be moved in

Feroughi et al. Proc. Combust. Inst. (2016), figures are reprinted with permission.

a range of 0-210 mm so that the optical measurements and the molecular beam sampling were obtained as a function of HAB. For optical access, four fused silica windows (50 mm in diameter) were equally distributed around the reactor side and flushed by the inert gas.

A sampling nozzle in combination with a skimmer (both made of nickel and 0.5 mm in orifice diameter) were used to form a molecular beam that propagated into the analysis chamber, where physical and chemical processes of particles were frozen due to the gas expansion with a pressure of $\sim 10^{-4}$ Pa. The charged particles travel through an electric capacitor, where they are deflected according to their mass and charge. By varying the voltage of the capacitor, the particles with the different charge/mass are classified and passed through an outer slit. Finally, these particles reach a Faraday-cup detector and the deflection voltage is measured. The mass of particles is calculated assuming completely fused, spherical particles within the molecular beam.

The measurements of temperature were carried out at five burner positions, leading to a variety of modified geometric configurations, which may cause the discontinuity in the temperature field. Therefore, simulations were performed separately according to the burner positions to quantify the uncertainties of the measurements. The sampling probing effect was not taken into account for the modeling of the particle synthesis, as the PMS measurements were conducted far downstream of the flame. Simulation results were compared with the measurements for the validation of the proposed kinetic model of SiO/SiO_2 formation. The measurements and the simulation results are presented in section 7.5.

Feroughi et al. Proc. Combust. Inst. (2016), figures are reprinted with permission.

Chapter 7

Simulations and results

Simulations and results are discussed in the same order as the experiments introduced in the previous chapter.

7.1 Effect of alignment of sampling nozzle and perforated plate on the ambient flame [22]

This section was previously published in 'Combustion and Flame, 162 (5), L. Deng, A. Kempf, O. Hasemann, O. P. Korobeinichev and I. Wlokas, Investigation of the sampling nozzle effect on laminar flat flames, 1737-1747 (2015)' and is reprinted with permission. The author L. Deng implemented the detailed models for viscosity and thermal conductivity of the gas phase and diffusive transport of species and a solver coupling the conjugate heat transfer to a reactive gas flow, ran all simulations, wrote the paper and generated all figures. The author O. Hasemann generated the reduced mechanism. The author O. P. Korobeinichev provided the experimental results and contributed discussions and proof-reading. The authors A. Kempf and I. Wlokas contributed guidance, corrections, discussions and proof-reading.

This section presents the simulations and the results for a premixed $CH_4/O_2/Ar$ and a premixed $H_2/O_2/N_2$ burnt on a perforated-plate burner. The objective of the simulation is to investigate the perturbation induced by the sampling nozzle and the perforated plate. The experimental setup was introduced in section 6.1.

In addition to the modeling of reactive flow, the heat transfer within the solid needs to be taken into account. This was described by the transient Fourier equation (7.1) for unsteady heat conduction. This equation was solved together with the conservation equations of the reacting fluid. In Eq. (7.1), c and k indicate the specific heat capacity and the thermal conductivity of the solid respectively.

$$\frac{\partial}{\partial t}(\rho c T) - \nabla \cdot (k \nabla T) = 0 \tag{7.1}$$

The surface of the quartz probe was assumed to be chemically inactive. However, the reaction

kinetics were affected by the presence of the wall through a longer residence time and heat transfer to the wall.

The transient simulation coupled the calculation of the chemical source term and the convective and the diffusive transport in the fluid with the heat conduction in the solid. Such computations suffer from a wide variation in the time scales governing the different physical phenomena involved. For a steady solution of the heat distribution within the solid nozzle, the transient term in equation (7.1) is zero, so that the specific heat capacity of the solid could be reduced, to shorten the convergence time.

Kinetic modeling

The reaction kinetics of the H_2/O_2 system was described using the mechanism by Li et al. [32], consisting of 8 reacting species and 25 reactions. The detailed mechanism was employed for the one-dimensional, the two-dimensional and the three-dimensional simulations.

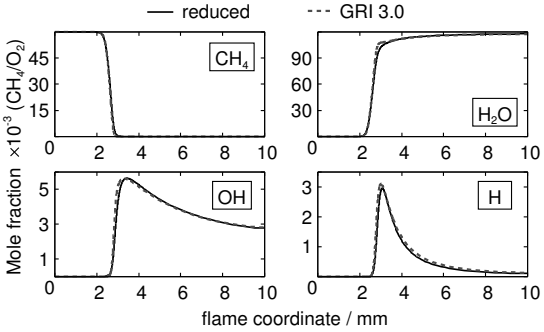

Figure 7.1: Species profiles in a freely propagating flame predicted with GRI3.0 and the new reduced mechanism. The unburned gases composition corresponds to the investigated methane flame. Reprinted with permission [22].

For the CH_4/O_2 system, the one-dimensional simulations were performed initially with the GRI 3.0 mechanism [123], which consists of 35 species and 219 reactions, excluding the C/N/O subsystem. The GRI mechanism required large computational times for the two-dimensional simulations and was not suitable for the simulations of different probe positions. Thus, a reduced mechanism was developed from the methane combustion mechanism by Cremer [174] and from the mechanism by O'Conaire et al. [122] as a hydrogen sub-system, using a genetic algorithm based reduction and optimization methods developed by Sikalo et al. [55]. The resulting reduced mechanism contains 14 reacting species and 26 reactions and was optimized to match the temperature profile and species' concentrations calculated with GRI 3.0 for an equivalence ratio of $0.7 < \Phi < 0.9$ at atmospheric conditions. Good

agreement between the GRI 3.0 and the new mechanism was achieved, as demonstrated for a freely propagating flame in Figure 7.1 for a fresh gas composition of the investigated methane flame. It must be noted that the aim of the reduction/optimization was to stay consistent with the reference mechanism used in the one-dimensional simulations, regardless of the quality of the reference mechanism.

Simulation

The overall simulation strategy required the investigation of all possible violations of the one-dimensionality of the flame, which is usually perturbed by the geometry and other properties of the experimental setup. The investigated flames are open to the atmosphere, which reduces the relevant geometric features to the perforated burner plate and the probing nozzle attached to the water cooled flange.

The CFD simulations of the flame-probe configuration were conducted in a two dimensional computational domain containing a fluid and a solid part. The axis-symmetric wedge had an extent of one element in the angular direction, as Openfoam requires a three-dimensional integration domain. The extent in the radial direction was chosen to be 20 mm, ensuring a sufficient distance between the burner and the boundary of the integration domain. The domain length was varied from 13.67 mm to 17.09 mm for the methane flame and from 13.9 mm to 15.9 mm for the hydrogen flame, depending on the burner and probe position.

The mass flow rate from the experiments [13, 147, 148] was set at the inlet where diffusion of species was suppressed. The temperature at the outer surface of the probe resulted from the coupled simulation. The inner surface was considered as adiabatic, neglecting heat losses due to radiation and convection at the very low gas density on the inside of the nozzle. The pressure at the outer boundaries of the integration domain was set to 101325 Pa, as all experiments were performed with burners, which were open to the atmosphere. The outlet pressure at the orifice was set to 60150 Pa for the methane flame and 63855 Pa for the hydrogen flame, resulting from the assumption of a critical mass flow rate through the choked orifice in the nozzle.

These simulations were performed for five significant probe locations in both, the methane flame (0.17, 0.32, 0.73, 1.06, 3.59 mm HAB [13]), and the hydrogen flame (0.4, 0.6, 0.8, 1.4, 2.4 mm HAB [147, 148]). All simulations were performed with Openfoam on a hexahedral mesh ranging from 37740 to 47980 cells; each case required a run time of 1 week utilizing 12 cores (AMD Abu Dhabi 6344, 2600 MHz). The effects induced by the perforated burner were simulated on a three-dimensional computational grid (19950 cells), which exploits various symmetry planes as shown in Figure 6.2. The domain extended 5 mm downstream from the perforated plate, to consider the distortion of the flame. The thickness of the reaction zone was 0.66 mm for the hydrogen flame and 0.8 mm for the methane flame, based on the steepest temperature gradient. The uniform inlet velocity corresponded to the mass flow rate in the experiments [13, 147, 148]. At the outer burner's outer surface, the temperature was calculated from the coupled heat flux simulation. The temperatures at the inlet and

at the aligned boundary of the solid part of the computational domain were set to values measured in the corresponding experiments (368 K for the methane flame and 333 K for the hydrogen flame). The run time for each simulation was approximately 5 days on 12 cores.

The 2-D/3-D simulations of the methane flame were conducted using a reduced mechanism to reduce computational cost. To obtain species' concentrations from the detailed mechanism, a post-processing procedure was applied by relying on the assumption that the temperature field is calculated with a good accuracy even when the reduced mechanism is used: First, the CFD simulation of the flame was performed with the reduced mechanism, which yielded the flow and temperature fields. These fields were used in Cantera to calculate the chemical state along a streamline, using a detailed mechanism. (This approach is widely applied where the temperature profiles can be obtained from the experiments.) One-dimensional simulations based on temperature profiles reconstructed with CFD have been presented by Weise et al. [149] or Wlokas et al. [91] in the past.

Results and discussion

Although the robustness and validity of the finite rate chemistry solver implementation in Openfoam was tested in Chapter 5, the 2-D modeling of investigated flame needs to be validated here. It was realized by comparing the results of three different simulations of the ideal burner-stabilised $H_2/O_2/N_2$ flame: an initial simulation was conducted in Openfoam in one dimension, a second one in Openfoam in two dimensions, and a third one in one dimension using Cantera. All three results in Figure 7.2 demonstrate a good agreement of the three methods. The small deviations are mainly due to the lower grid resolution of the Openfoam simulations and due to the slightly different treatment of the inflow boundary conditions in Cantera. The good agreement of the temperature field is particularly relevant for the species post processing that was previously outlined and inspires confidence that the burner- and probe-induced effects on the flame can be simulated with good accuracy.

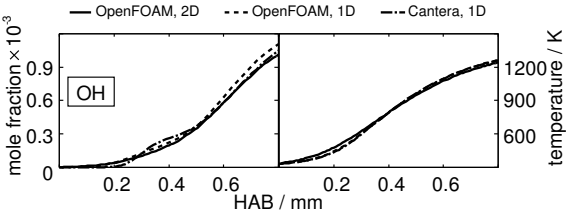

Figure 7.2: Mole fraction of OH and the temperature as function of height above burner (HAB) simulated with Cantera and with Openfoam for the hydrogen flame. Reprinted with permission [22].

The sampling probe causes aerodynamic effects (flow acceleration and hence reduced residence time) and thermal effects (heat transfer to and from the nozzle) on the flow, the

temperature and the species fields. In order to distinguish between the thermal and the aerodynamic effects, different temperature boundary conditions were applied for the probe: an adiabatic, an isothermal and the conjugate heat transfer model between the gas phase and the solid probe. The results for the hydrogen flame are shown in Figure 7.3 in comparison to the idealized one-dimensional flame (see also Figure 7.2). The isothermal boundary condition had a strong impact on the temperature and the OH mole fraction profile, whereas the adiabatic and the conjugate heat transfer model showed a smaller deviation from the ideal, unperturbed flame. From the results in Figure 7.3 one may conclude that the distortion of the flame (up to HAB of 0.7 mm) is caused by aerodynamic effects since the adiabatic and the conjugate heat transfer model show a similar deviation from the ideal 1-D flame. The aerodynamic and the thermal effects can be individually distinguished only near the orifice (above HAB of 0.7 mm in Figure 7.3), where the accelerated gas is cooled. This cooling has little effect on the OH mole fraction (compared to the adiabatic probe), as the residence time in this area is short due to the strong acceleration of the fluid. The overall effect on the species' concentrations is considerable – deviations of up to 25 % are observed.

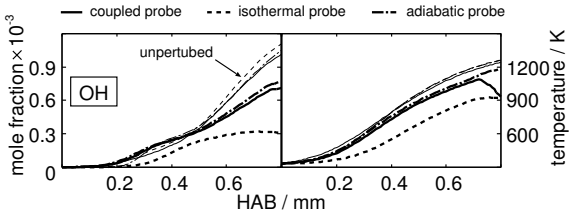

Figure 7.3: Mole fraction of OH and the temperature as function of height above burner (HAB) at the burner axis in presence of a sampling probe for the hydrogen flame. Reprinted with permission [22].

As the measurements in the atmospheric flame were conducted at a very small HAB, the perforation of the burner plate had to be considered in order to account for the magnitude of possible deviations. Figure 7.4 shows the simulation results considering the perturbations induced by the perforated plate for the methane and for the hydrogen flame. From the velocity fields in the vicinity of the burner surface, the streamlinepatterns indicate a "weak" recirculation or wake caused by the solid parts of the perforated plate. This wake zone thickens the temperature and the stable species' concentration (H_2O) layer. For the intermediate species of OH, CH_3 or H, this aerodynamic effect is weak, leading to a very homogeneous concentration field. Figure 7.4 shows a uniform temperature field above the plate and hence a negligible thermal impact from the perforated plate. This result confirms the findings by Somers et al. [144]. The simulation results along three parallel lines, which are indicated in Figure 7.4, are presented in Figure 7.5. Near the burner surface, the variation in the mole fractions of H_2, CH_4 and H_2O for the three lines has the same quantity as the

Deng et al. Combust. Flame (2015), reprinted with permission.

deviation between experiment and the various models (see Figure 7.10). For probe positions very close to the burner surface, the probe suction affects an area that covers the entire center to center distance between the holes and thus may lead to some compensation of the inhomogeneity of the burner. However, compensation effects could not be quantified, as the history of the sample after passing the orifice remains unknown. In the present study, the position of the probe tip relative to the single holes of the burner surface is not accounted for, but the simulation sheds light on some disagreement between experiment and the idealized one-dimensional simulation. The problem of inhomogeneous flow in the vicinity of the burner surface does not occur for sinter matrix burners. The subsequent simulations were performed assuming an ideal burner and conjugate heat transfer between the solid probe and the gas for a steady state flow.

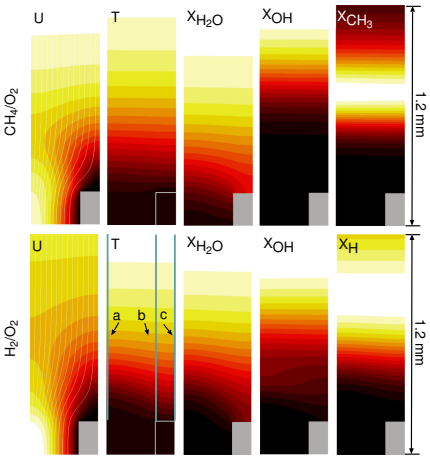

Figure 7.4: Qualitative pattern of the velocity, the temperature and the mole fraction of H_2O, OH and CH_3 field for the CH_4/O_2 flame, and the mole fraction of H_2O, OH and H field for the H_2/O_2 flame respectively. Reprinted with permission [22].

The impact of the probe on the temperature field is displayed in Figure 7.6. The large distortions in the temperature field are mainly a result of convective transport, not of diffusion or heat conduction. This conclusion is also supported by the results shown in Figs. 7.7 and 7.8 for both flames, where the strong effect of the aerodynamic distortion on the radical species' concentrations is clearly visible. Figures 7.7 and 7.8 show passive Lagrangian particles that enter the domain every 0.1 ms (for the hydrogen flame) and every 0.15 ms (for the methane flame). The particles indicate that the zone where the assumption of one-dimensionality is violated, is restricted to a spherical volume with a radius of roughly 3

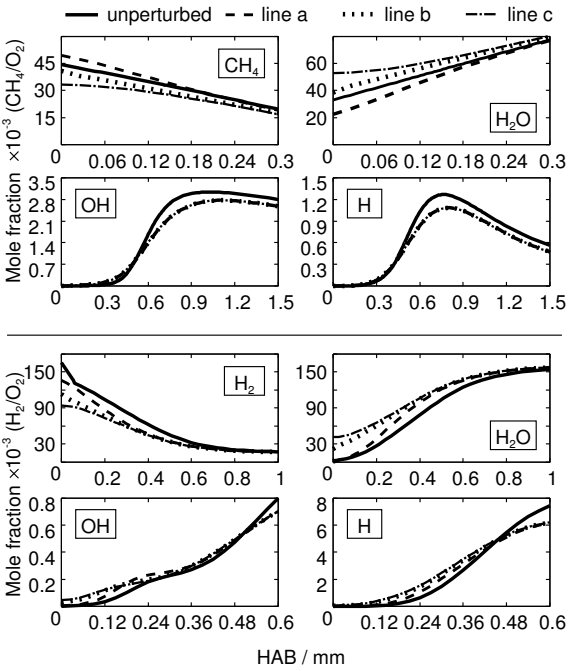

Figure 7.5: Species mole fractions from simulation of the investigated CH_4/O_2 flame and the H_2/O_2 flame above the perforated plate, along lines a, b, and c as displayed in Figure 7.4. The solid line indicates the unperturbed flame above an ideal flat flame burner. Reprinted with permission [22].

orifice diameters. However, it must be stressed that this affected volume is the region from which the sampled gas is taken. Figure 7.9 shows the magnitude of velocity for different distances between the burner and the probe. The area of high acceleration and short residence time corresponds to the observation made with Lagrangian particles. Furthermore, for the short residence times of the probe in the flame the thermal distortion becomes significant – and more importantly: less quantifiable.

Figures 7.7 and 7.8 show heat conduction in the probe (arrows). Interestingly, the tip can actually be hotter than the surrounding gas. This weak effect may be relevant when measurements are taken on the cold side of the flame. Another weak effect on the concentrations of species is the gas dynamic cooling caused by the acceleration of the flow up to the local speed of sound in the orifice plane. Assuming a constant c_p of the sample during

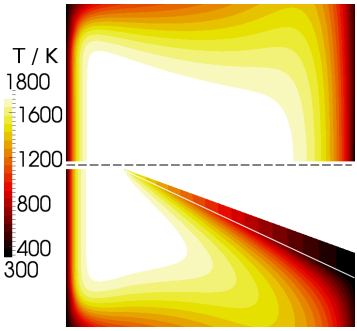

Figure 7.6: Temperature field for a probe position of 3.59 mm over the burner surface. The temperature of the probe tip (solid) reaches 1570 K, while the gas temperature at the probe orifice reached 1720 K. Reprinted with permission [22].

the isentropic and adiabatic acceleration up to the speed of sound, an additional cooling of $\sim$ 150 K can be expected. This temperature difference is notable, but the corresponding residence time is also very short (see Figure 7.9), so that the impact on species' concentrations measurements is expected to be small. A more detailed investigation of the flow in the direct vicinity of the orifice is not possible using the low-Mach number approach and would require a solution scheme for a fully compressible formulation of the conservation equations.

Deng et al. Combust. Flame (2015), reprinted with permission.

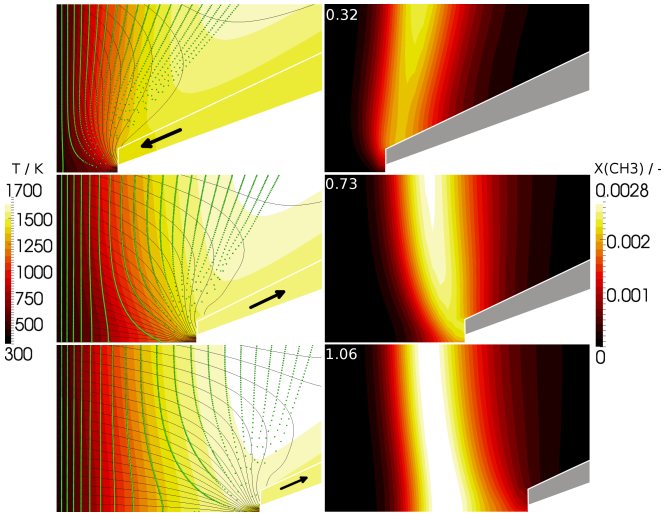

Figure 7.7: Simulation of the CH_4/O_2 flame: temperature field and streamline pattern on the left-hand and CH_3 radical concentration field on the right-hand side for probe positions of 0.32 mm, 0.73 mm and 1.06 mm above the burner surface. The sample history is visualized by the Lagrangian particles entering the domain in steps of 0.15 ms. Reprinted with permission [22].

An important aspect of the simulations was the steady state assumption for the heat conduction in the solid parts. A transient simulation of one second physical time would require approximately 5 weeks of computational time on the 12 cores, while the thermal steady state of the experimental setup takes up to several minutes of real time. Thus, the thermal distortion is minimized in the experiment and can be quantified by simulations only if the probe remains long enough in the flame.

A comparison of the simulation results and the measurements are shown in Figure 7.10 and in Figure 7.11 for the methane and hydrogen flames respectively. The classical, one-dimensional model of the burner-stabilized, laminar flame without correction was not able to reproduce the measurements. The raw results of species mole fractions in the orifice plane, calculated with Openfoam have already shown a good agreement despite the low grid resolution.

The CFD simulations of the methane flame were conducted using a reduced mechanism. The impact of simplification of the reaction mechanism must be analyzed and compensated for. This was achieved in a post processing step where the one-dimensional equations of the laminar flame were solved with Cantera using the GRI 3.0 reaction mechanism, employing

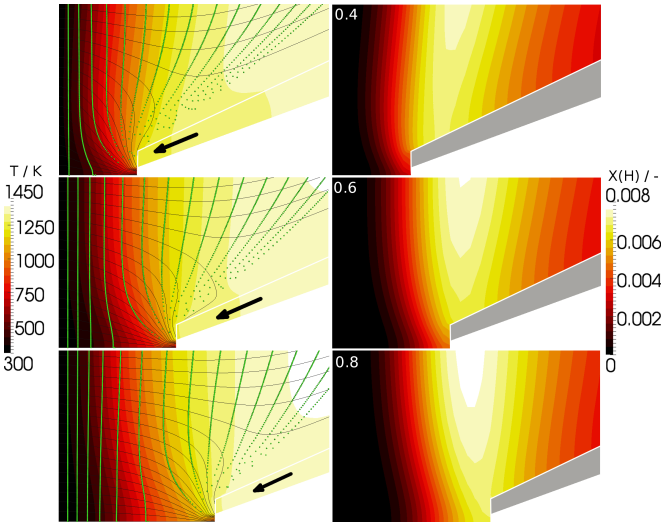

Figure 7.8: Simulation of the H_2/O_2 flame: temperature field and streamline pattern on the left-hand and H radical concentration field on the right-hand side for probe positions of 0.4 mm, 0.6 mm and 0.8 mm above the burner surface. The sample history is visualized by the Lagrangian particles entering the domain in steps of 0.1 ms. Reprinted with permission [22].

the velocity and temperature fields obtained with Openfoam along a streamline. This procedure resulted in the best agreement between simulation and experiment. Interestingly, the deviation of the simulations from the experimental measurements near the burner surface is of similar magnitude as the spread of the concentrations of species in the simulations of the perforated burner plate, displayed in Figure 7.5. However, a detailed and quantifiable study of this effect would require additional measurements.

The methane flame was investigated previously by Skovorodko et al. [140]. Their observations, including a downstream shift of the flame, were qualitatively similar to the results presented here. (It should be noted that the simulation strategy employed by Skovorodko and colleagues was very different and required much more *ad hoc* assumptions and sophisticated measurements of boundary conditions.) In the present study, the number of assumptions was minimized to the unknowns of the experimental setup and quantities that are inaccessible by the physical model employed. These are: a) the relative position of the orifice to the burner plate holes, b) the assumption of a critical flow state in the orifice plane, and c) no heat flux through the inner surface of the nozzle.

The extensive simulations of a hydrogen and methane flame provided detailed insight into

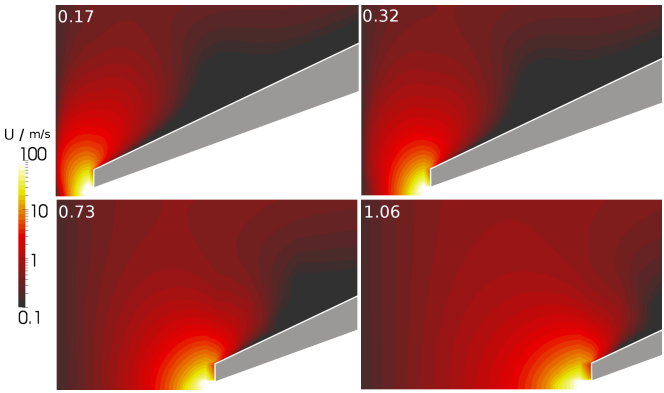

Figure 7.9: The velocity field for different probe positions (methane flame) shows the strong distortion of one-dimensionality, but also the boundary layer at the probe and the area of high acceleration; the color coding is logarithmic and clipped at 100 m/s. Reprinted with permission [22].

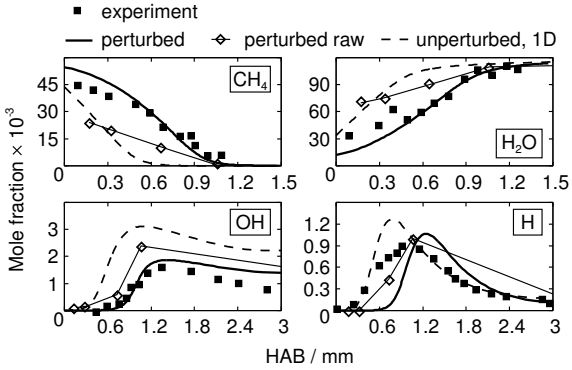

Figure 7.10: Species mole fractions from simulations of the investigated CH_4/O_2 in comparison to experiments [13]. The species mole fractions from perturbed flame (solid line) were calculated in one-dimensional simulations using the "reconstructed" temperature profiles of the flame. Reprinted with permission [22].

Deng et al. Combust. Flame (2015), reprinted with permission.

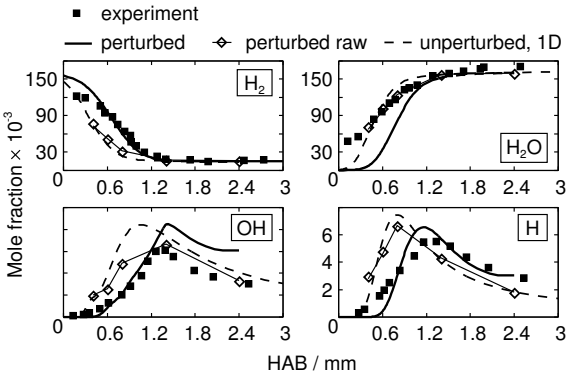

Figure 7.11: Species mole fractions from simulations of the investigated H_2/O_2 in comparison to experiments [147, 148]. The species mole fractions from perturbed flame (solid line) were calculated in one-dimensional simulations using the "reconstructed" temperature profiles of the flame. Reprinted with permission [22].

the perturbation effects caused by the invasive probing technique. The CFD, using detailed transport models, was shown to reconstruct the temperature field with good accuracy. Complementary CFD enables a better interpretation of species' concentrations measurements in the absence of temperature and flow field measurements, and also allows assessment of the experimental uncertainties. The findings may be summarized as follows:

(a) assuming the probe has a cold, isothermal surface leads to an overprediction of the probe perturbation effect. This means that a short residence time of the probe in the flame reduces the reproducibility of the measurements and a thermal steady state of the experimental setup should be achieved before the measurement is taken. For a long residence time of the probe in the flame, the adiabatic and the conjugate heat transfer boundary conditions lead to a similar prediction of the perturbation of the species' concentration. The presence of an adiabatic probe causes small deviations in the flame temperature but a significant impact on the measured species' concentrations.

(b) The aerodynamic cooling due to the acceleration has little effect on species' concentrations.

(c) The geometric distortion (stretching) of the flame caused by the suction is the dominant mechanism for the perturbations caused by the probe.

(d) It was shown that accurate temperature profiles along the probe axis, either from CFD

or measurements, are indispensable for one-dimensional simulations of the experimental setup.

Considering the wide variety of nozzle types, operating conditions and the complex interaction of the non-linear physical phenomena involved, it seems unlikely that a simple scaling rule or correction formula can describe the impact of the probing nozzle with good accuracy.

7.2 Effect of buoyancy and sampling nozzle in a low pressure flame reactor

The work in this section is going to be submitted to the journal Combustion and Flame. L. Deng developed the code and the flame model, ran all simulations. Y. Karakaya from the Chair of Thermodynamics, Institute for Combustion and Gas Dynamics, University Duisburg-Essen conducted the experiments.

The simulations and the results for premixed $CH_4/O_2/Ar$ flames in a low-pressure reactor will be discussed here. The configuration of the experimental setup was introduced in section 6.2. The effect of buoyancy and sampling nozzle were evaluated.

The geometric configuration of reactor may affect the flow field and cause the deviations from axisymmetry that can not be addressed by 2-D simulations. To investigate whether the 3-D setup of the reactor can be reduced to the 2-D configuration for the simulation, the consistency of fluid dynamic behavior between 2-D and 3-D simulation needs to be proven. This is realized by 2-D and 3-D simulations using simply a hot gas emerging from the burner surface neglecting chemical reactions. It is the first and necessary step towards the detailed studies of combustion in a reactor using 2-D simulation.

Kinetic modeling

The reaction mechanism used for the simulation of the $CH_4/O_2/Ar$ flame was DRM 22 [124], which is a reduced mechanism based on GRI 1.2 [123]. This mechanism constitutes 22 species and 104 reactions, as a suitable mechanism offering a compromise between modeling accuracy and computational cost.

Simulation

The simulation domain for the 3-D simulations was a pseudo 3-D grid (398,376 cells) that represented a quarter of the experimental configuration. For the study of 3-D effects, the domain was extended by 125 mm (diameter of the reactor) in radial direction. On the inlet, a mass flow rate boundary condition, corresponding to the volume flow rate fed into the reactor, was applied, while the temperature was set to 400 K. The pressure in the reactor was equal to 16,000 Pa. An adiabatic boundary condition was applied on the sampling nozzle outer surface, which appears realistic due to the thin thickness (10 μm) of the sampling

nozzle and hence the little heat conduction it permits. The nozzle orifice was closed, as the influence of the open orifice was studied in the later 2-D simulations.

The simulation required the heat release from the chemical reaction. Since the modeling of finite rate chemistry for a methane flame was prohibitive for the 3-D simulation and detailed knowledge of the combustion was not relevant for the study of the geometric effect, a volumetric heat source was used to provide the energy that heats the gas to the desired temperature. Replacing the term that accounts for the heat release from the reaction ($\dot{w}_T$) with a fixed heat source ($\dot{Q}_c$), and neglecting the terms considering viscous heating, species diffusion and chemical reaction, the energy conservation equation 2.9 was simplified as:

$$\frac{\partial}{\partial t}(\rho h_s) + \nabla \cdot (\rho \boldsymbol{u} h_s) = \frac{Dp}{Dt} + \nabla \cdot (\alpha \nabla h_s) + \dot{Q}_c \tag{7.2}$$

A similar approach had been employed by Weise et al. [149] in a 3-D reactor simulation and Skovorodko et al. [140] in a 2-D simulation. The buoyancy force resulting from the density gradient was taken into account by a volume force density term in the momentum transport equation.

Two types of 2-D simulations were carried out. The first type of 2-D simulations were used to compare with the 3-D simulation to evaluate the geometric effect. These simulations employed the heat source and the same boundary conditions as the 3-D simulation. The second type of 2-D simulations calculated the detailed chemistry to investigate the alignment of the probe nozzle on the target flame. For the first type of simulations, a quasi 2-D computational domain, which featured a symmetric wedge with an extent of one cell in the angular direction, was used. The axial extent of the domain was 150 mm, which was sufficient for solving the flow field downstream. For the second type of simulations, the differences were the following: the length of the domain was varied in a range of 1, 2.25, 3.25 and 25 mm, as these values were relevant measuring positions in the experiment, leading to a total grid cell number from 19,660 to 30,655. The nozzle orifice was open with a pressure of 12,000 pa that was calculated from the assumption of a critical mass flow rate through the choked orifice in the nozzle.

Results and discussion

The computed velocity and the temperature fields from the 2-D and 3-D simulation, with and without gravity, are shown in Figure 7.12. The results from the 2-D and 3-D simulations are in good agreements, which suggests the suitability of the 2-D simulation to capture the 3-D geometric constraints. Further in Figure 7.12, it can be seen that the structure of the velocity and the temperature field calculated without gravity are similar to the 1-D flame predictions that were shown in section 5.1. This proofs one of the most important features of the present flame, that the simple flame structure enables a 1-D modeling approach. A sharp velocity and temperature rise due to the heat release from the volumetric heat source can be observed close to the burner surface. The temperature and the velocity attain a peak value at roughly 5 mm above the burner, after which they continuously decrease due to the gas

expansion. In contrast to the behavior discussed above, the simulations considering gravity show a two-step axial velocity increase and a relatively flat temperature profiles downstream (see Figure 7.13). This effect results from the buoyancy force and violates the pseudo 1-D assumption, especially far downstream from the burner. However, due to the fact that the flame species are usually sampled at low HAB, the top wall of the reactor is closer towards the burner and thus shortens the flow path and limits the evolution of the flow. Therefore, the buoyancy force hardly affects the measurement of species concentrations in these cases. This is proven by the comparison of simulation results between a 1-D, unperturbed Cantera simulation and a 2-D simulation with the sampling position at 25 mm (see Figure 7.17 and 7.18). Nevertheless, for the measurements of the particle distribution function under such a flow condition, the buoyancy effect may become relevant, since the measurements are normally conducted downstream of the flame. Due to the fact that the modified velocity affects the residence time of the particles and the temperature affects the particle formation, gravity was taken into account in the next two simulations regarding the particle formation and growth.

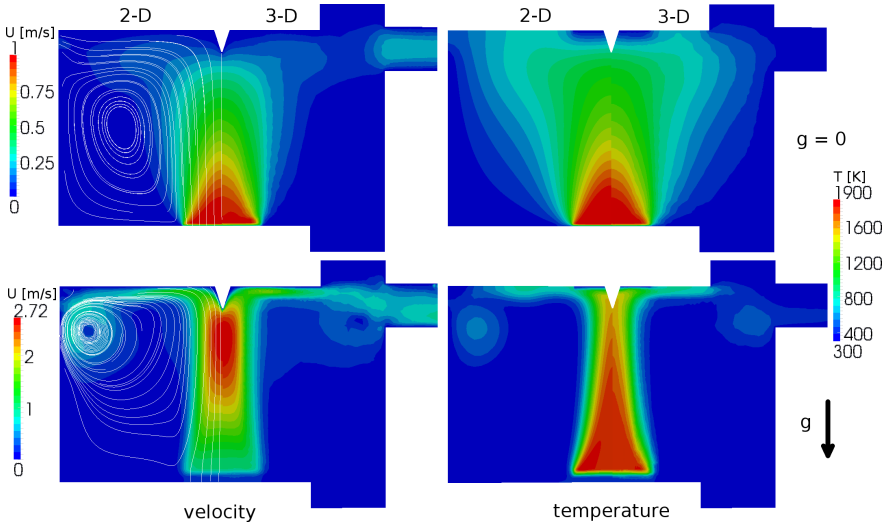

Figure 7.12: The velocity and the temperature field from 2-D and 3-D simulation, top: simulation without gravity, bottom: simulation with gravity.

The simulated temperature and species OH and H were found to provide a consistent picture of the physics. However, simulation results for CH_3 have shown a strange behavior, e.g. under the probing effect, the mole fraction of CH_3 for the whole flame was increased,

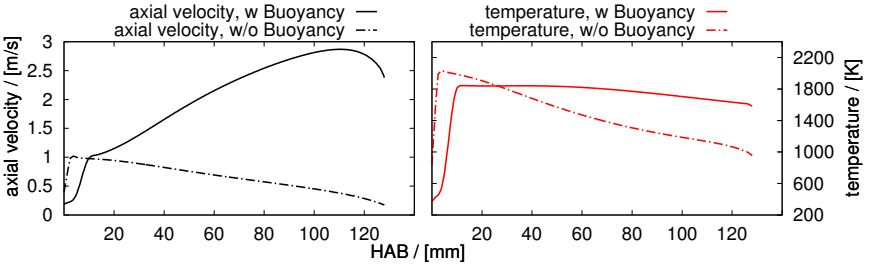

Figure 7.13: Axial velocity and temperature from 3-D simulation with and without buoyancy effect.

even at the position far away from the orifice (see Figure 7.14). This inconsistency could be addressed to the reduced reaction mechanism used for the simulations. In order to prove this, simulations were carried out in Cantera with the velocity and temperature profile along the streamlines from Openfoam simulations, as indicated in Figure 7.14 left. Simulation results along the different streamlines show a similar behavior. As an example, simulated CH_3 mole fractions along one streamline were displayed in Figure 7.15 and two inconsistencies appear here. First, the mechanism DRM 22 shows a significant inconsistency in comparison to the original mechanism GRI 1.2 for the simulation using the velocity and temperature profile from Openfoam with the closed orifice. It seems that the CH_3 prediction was not the focus in the mechanism reduction and validation for the investigated flow conditions. Second, the mechanism DRM 22 is more sensitive to the very slightly changed velocity profile compared against the mechanism GRI 1.2. Thus, as shown in Figure 7.14 and 7.15, the CH_3 concentration increases significantly with the open orifice. Nevertheless, tests using the original mechanism (GRI 1.2) have shown a consistent picture for CH_3 and consistent CH_3 mole fractions were predicted for the cases with open and closed orifice.

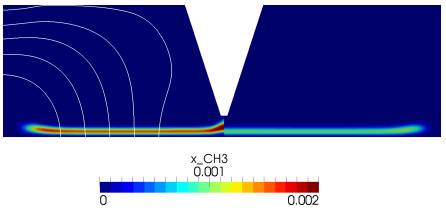

Figure 7.14: Strange (unphysical) behavior of CH_3 mole fractions with open (left) orifice in comparison to closed (right) orifice.

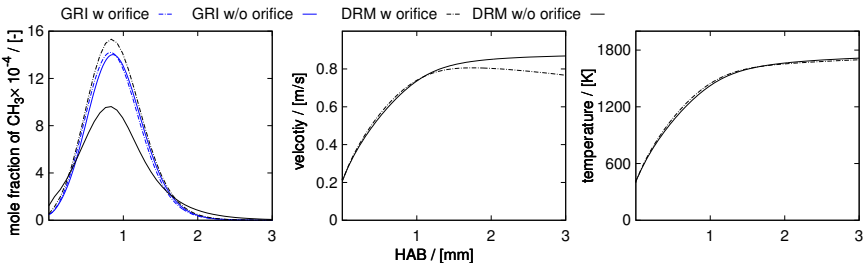

Figure 7.15: Prediction of CH_3 mole fraction using different mechanisms for the investigated case. Left: simulated CH_3 mole fraction using GRI 1.2 and DRM 22 mechanism with the velocity and temperature profiles from 2-D simulation with open and closed orifice. Middle: the velocity profiles from 2-D simulations with open and closed orifice. Right: the temperature profile from the 2-D simulations with open and closed orifice.

Figure 7.16 shows the computed temperature and the mole fraction fields of OH and H from the stoichiometric flame affected by the sampling nozzle at different positions. At the farthest position of 25 mm above the burner, the sampling nozzle hardly influences the flame, and thus a flat unperturbed flame can be seen in the left column of Figure 7.16. As shown in the top of Figure 7.16, the closer nozzle position leads to a cooler temperature field, due to a stronger convective heat loss to the cool top wall of the reactor. Correspondingly, the mole fraction of the species decrease as the sampling nozzle approaches the burner surface. Furthermore, the aerodynamic effects induced by the sampling nozzle can significantly modify the flame shape. Taking the mole fraction OH as an example, the sampling nozzle at the position 3.25 mm above the burner lifts the flame away from the burner. In contrast, the sampling nozzle at the position of 1 mm pushes the flame towards the burner surface. A similar behavior is also found for other radicals. The mentioned aerodynamic effects are the main mechanisms that causes the deviations in comparison to the unperturbed flame. Most interesting are the simulation results along the centerline, where the species samples are captured.

A comparison of the simulation results and the measurements, in terms of temperature and species mole fractions, for all the flames are shown in Figures 7.17 and 7.18, respectively. For the results from the 2-D simulations with the nozzle position of 25 mm, agreement is achieved compared with an unperturbed 1-D Cantera simulation. It demonstrates again the robustness and the reliability of the implemented flame models and the irrelevance of the buoyancy effect for a distance between the sampling nozzle and the burner surface of less than 25 mm. The diamond points indicate the simulation data sampled by the sampling nozzle. As illustrated in Figure 7.17, a significant cooling effect of the sampling nozzle is identified in the measurements. This effect is also well predicted by the 2-D simulations. The highest temperature in the measurement is shown for the stoichiometric flame ($\Phi = 1$). Not

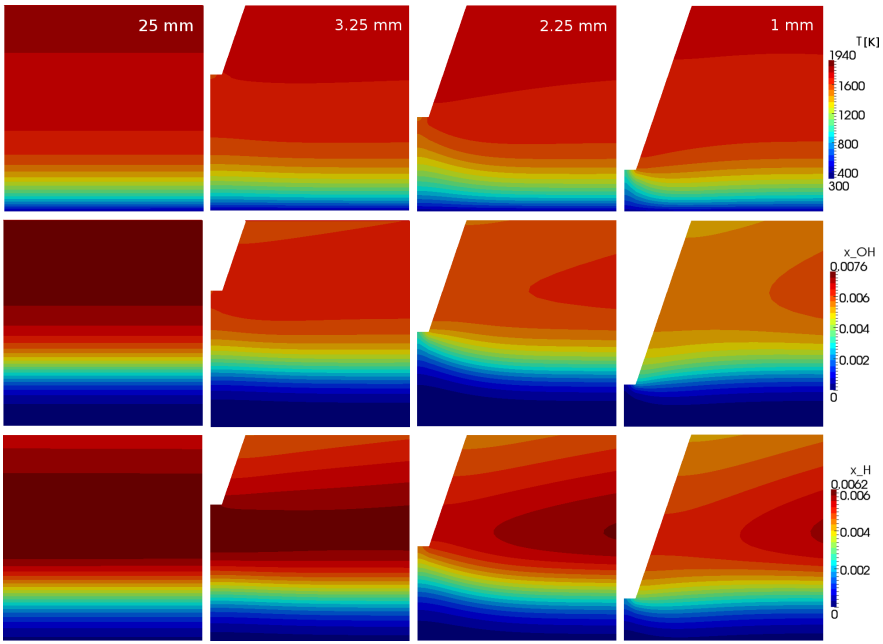

Figure 7.16: Temperature and mole fraction of OH and H from the 2-D simulations concerning various sampling nozzle positions.

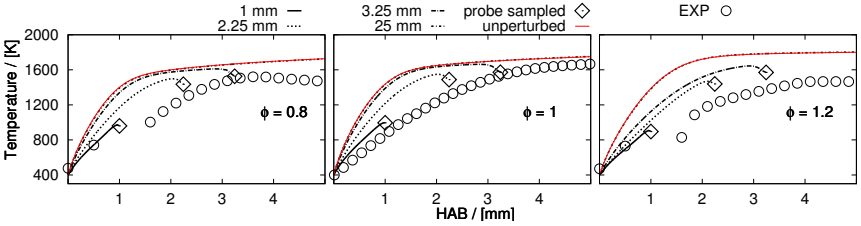

Figure 7.17: Axial temperature from simulation in comparison to experiments. The temperature from unperturbed flame was calculated in 1-D Cantera simulation (solid red line) and the temperature from perturbed flame was calculated in 2-D simulations (black dashed lines).

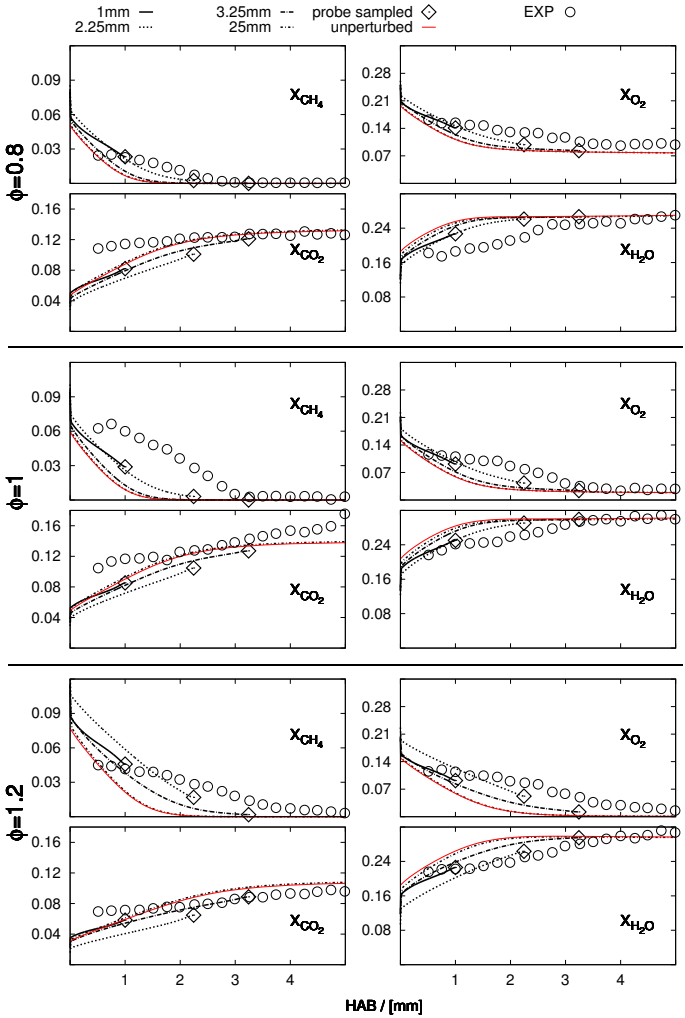

Figure 7.18: Mole fraction of CH_4, O_2, CO_2 and H_2O from simulations in comparison to experiments. The species mole fractions from unperturbed flame were calculated in 1-D Cantera simulation (solid red line) and the species mole fractions from perturbed flame were calculated in 2-D simulations (black dashed lines).

surprisingly, both 1-D Cantera simulations and 2-D Openfoam simulations also predicted the highest temperature for the stoichiometric flame. For all the flames, overall good agreement is shown in the profiles of the temperature and the mole fractions of CH_4, O_2 and H_2O. A notable deviation appears in the profile of the CO_2 mole fraction for the flames with equivalence ratios of 0.8 and 1, though the trend of the CO_2 mole fraction is predicted well. Another significant discrepancy is in the mole fraction of CH_4 for the stoichiometric flame upstream, where the simulation underpredicted the measurements. It is possible that the deviations are due to uncertainties in the flow rate controller for the fresh gas inflow, where a 5% bias may exist.

A detailed study of the buoyancy effect on laminar, premixed flat-flames at low pressure was presented by Weise et al. [149]. They found that the buoyancy force lifts the center of the flame upwards in the horizontally aligned reactors, which violated the assumed 1-D model. Since then, all reactor setups within the NETZ building were adjusted vertically. However, as shown in the current work, another aspect of the buoyancy effect that accelerates the flow field and modifies the temperature field was found in a vertically aligned reactor. This highlights the importance of a parameter study by simulating the flame reactors. Care must also be taken when choosing operating conditions for the investigated flame to avoid unexpected buoyancy effects. A significant probing effect is shown for the investigated flame, so that the complementary 2-D simulation including the sampling probe is indispensable for the comparison of the experimental measurement and the modeling prediction.

7.3 Effect of alignment of sampling nozzle on the formation of early iron particles [12]

This section was previously published in 'CrystEngComm 17 (36), S. Kluge, L. Deng, O. Feroughi, F. Schneider, M. Poliak, A. Fomin, V. Tsionsky, S. Cheskis, I. Wlokas, I. Rahinov, T. Dreier, A. Kempf, H. Wiggers and C. Schulz, Initial reaction steps during flame synthesis of iron-oxide nanoparticles, 6930-6939 (2015)' and figures are reprinted with permission. The author L. Deng implemented the detailed models for viscosity and thermal conductivity of the gas phase and diffusive transport of species, ran all simulations and generated parts of the figures. The author S. Kluge conducted the PMS and QCM measurements for the Duisburg reactor, wrote the paper and generated most parts of figures. The author O. Feroughi conducted the LIF measurements for the Duisburg reactor. The authors F. Schneider, M. Poliak, A. Fomin and V. Tsionsky conducted the experiments for the Tel Aviv reactor. The authors S. Cheskis, I. Wlokas, I. Rahinov, T. Dreier, A. Kempf, H. Wiggers and C. Schulz contributed guidance, corrections, discussions and proof-reading.

The simulations and the results for a premixed $H_2/O_2/Ar$ in the DU-R and a premixed $CH_4/O_2/N_2$ in TA-R will be discussed in this section. Both flames were doped with $Fe(CO)_5$ for the formation of iron-oxide particles. The flame configurations and the experimental approaches were introduced in section 6.3.

Kinetic modeling

The addition of iron-oxide precursor influences the flame chemistry, due to the presence of iron atoms. The previous studies of Linteris et al. [175] found an increasing heat release if the lean premixed hydrogen flame was doped with iron pentacarbonyl in a low pressure environment. Such an effect needs to be taken into account in reaction mechanisms by involving the main reaction path of flame radicals and metal species interaction. Recently, based on the mechanism developed by Wen et al. [158] and Wlokas et al. [91], in the work of Feroughi et al. [157] a sub-mechanism of $Fe(CO)_5$ was proposed. This sub-mechanism involves the pyrolysis of $Fe(CO)_5$, the formation of iron clusters, the interaction of flame radicals with iron-containing species, and the formation of iron-oxide molecules. Furthermore, the $Fe(CO)_5$ sub-mechanism can be added to other flame reaction mechanisms for the simulation of nanoparticle synthesis in different assisted flames.

In the present work, the iron sub-mechanisms was combined with the C1 mechanism proposed by Li et al. [32] and with the DRM-22 mechanism [124] for the simulations of a $H_2/O_2/Ar$ flame within the DU-R and for the simulations of a $CH_4/O_2/N_2$ flame within the TA-R, respectively. These mechanisms are computational expensive, further reductions were thus required to obtain efficient skeletal mechanisms with a satisfied accuracy. By applying a genetic algorithm method proposed by Sikalo et al. [55], the mechanisms were finally reduced to the size of 40 species and 66 reactions for the hydrogen flame and 50 species and 140 reactions for the methane flame. The reduced mechanisms were validated by comparing the simulation results in terms of laminar flame speed, adiabatic flame temperature, total iron-cluster mole fractions and mole fraction of iron-oxide against the results of the detailed mechanism. Cantera allows 1-D simulations using much bigger mechanisms, so that the iron sub-mechanism is added to GRI3.0 [123] to predict much more accurate species concentration.

Simulation

A reactor similar to the DU-R and the TA-R has been already investigated in subsection 7.2, proving that a quasi-2D rotationally symmetric computational domain is sufficient to capture the influence of the reactor housing and the sampling probe on the flame. For the DU-R, the simulations were conducted with the burner-probe distance of 2, 4, 6, 8, and 10 mm to account for the perturbation induced by the probe. The grids were in a range of 34,000 to 51,800 cells. An adiabatic boundary condition was applied on the outer surface of the probe, as it was made of nickel and had a thickness of 10 μm. The temperature on the outer boundary was set equal to 300 K to mimic the heat losses through the reactor housing.

For the TA-R, a numerical domain similar to the one for the DU-R was used. Due to the large reactor diameter of the TA-R, the radial extent of the numerical domain was set smaller to reduce the computational cost by decreasing the grid size. Therefore, an inlet-outlet boundary condition was applied on the outer boundary to allow inflow of cool gases into the domain.

Kluge et al. CrystEngComm (2015), figures are reprinted with permission.

To avoid the errors caused by the reduced skeletal mechanism, a post processing step similar to the approach in section 7.1 was applied. In this step, the 1-D equations of the laminar flames were solved with Cantera using the detailed mechanism, employing the temperature profiles along the streamlines calculated from Openfoam. This approach may compensate for the bias of the species prediction caused by the reduced mechanism.

Results and discussion

The iron atoms and the CO are formed from the decomposition of $Fe(CO)_5$ in the flame. The iron atoms react in a catalytic cycle with flame radicals (H and OH) and thus affect the combustion chemistry. Therefore, in the first step, the impact of addition of $Fe(CO)_5$ on the temperature without invasive probing was investigated. Figure 7.19 shows the significant difference of the computed temperature fields for the DU-R flame with and without 300 ppm $Fe(CO)_5$. The addition of $Fe(CO)_5$ in the fresh gas clearly increases the temperature in the vicinity of the burner.

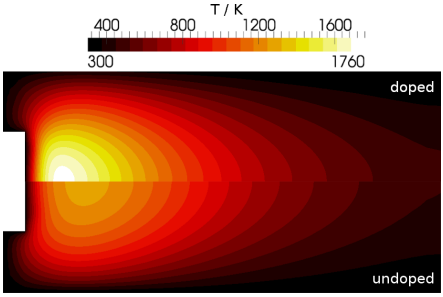

Figure 7.19: Computed temperature of DU-R flame, top: doped with 300 ppm $Fe(CO)_5$, bottom: undoped. Reprinted with permission [12].

In the experiment, the temperature was measured via multiline NO-LIF thermometry for varied positions of the sampling nozzle. Figure 7.20 shows the measured temperature profiles of the flame doped with 0 ppm, 100 ppm and 200 ppm $Fe(CO)_5$. The sampling position here is 8 mm above the burner, where the probe hardly influenced the temperature field. The temperature along the centerline was obtained by an average over a region $\pm$ 1.5 mm around the axis and plotted to indicate the influence of the different concentration of the precursor. It is clear that the temperature of the flame increases with the increasing concentration of $Fe(CO)_5$.

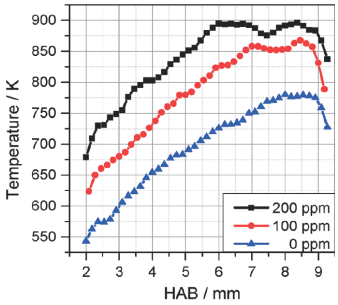

Figure 7.20: Measured axial temperature of DU-R flame with 0, 100, and 200 ppm $Fe(CO)_5$. Reprinted with permission [12].

Figure 7.21 shows the computed and the measured temperature field for the probe position of 8 mm HAB. While the temperature fields are very similar in the region between the burner and the probe, they don't match well in the absolute value, because the simulation suffers from the uncertainties in the temperature boundary setting on the burner surface. However, both the modeling prediction and the measurement demonstrate that at this probe position, the effect of the probe on the temperature is quite weak.

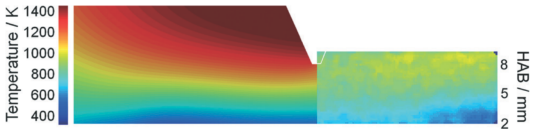

Figure 7.21: Comparison of computed temperature (left) with multiline NO-LIF measured temperature (right) for the DU-R flame doped with 200 ppm $Fe(CO)_5$ under the perturbation of probe at 8 mm above the burner. Reprinted with permission [12].

The initial formation of particles is strongly linked to Fe atoms, which are generated from the decomposition of $Fe(CO)_5$. This process is very sensitive to the experimental conditions, due to the limited thermal stability of $Fe(CO)_5$. In the experiment, the spatial distributions of iron atoms were measured close to the burner by Fe-LIF imaging employing laser excitation around 225.15 nm. In order to investigate the probe induced perturbation on the iron atom concentration, the measurements were conducted for the probe position of 5 mm, 7 mm and 9 mm, individually. The first two millimeters were not accessible by the laser sheet because of geometric constraints.

Kluge et al. CrystEngComm (2015), figures are reprinted with permission.

As illustrated in Figure 7.22, both simulation and measurement show a strong impact of the probe nozzle (HAB= 5mm) on the field of Fe concentration. In the vicinity of the nozzle orifice, the velocity increases and the Fe concentration decreases significantly.

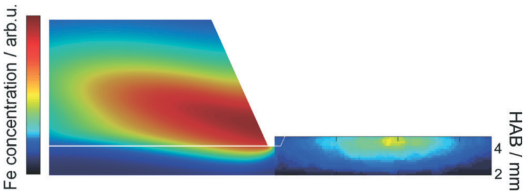

Figure 7.22: Comparison of the computed iron atom concentration (left) with the Fe-LIF measurements (right) for the DU-R flame doped with 200 ppm $Fe(CO)_5$ under the perturbation of probe at 5 mm above the burner. Reprinted with permission [12].

Figure 7.23 presents the measured Fe concentration within the flame doped with 100 ppm and 200 ppm $Fe(CO)_5$. Similar to the measured temperature field, the probe hardly influences the Fe concentration field at high HAB of 9 mm, whereas for low HAB, such as 5mm and 7mm, the suction of the probe significantly affects the local Fe concentration field.

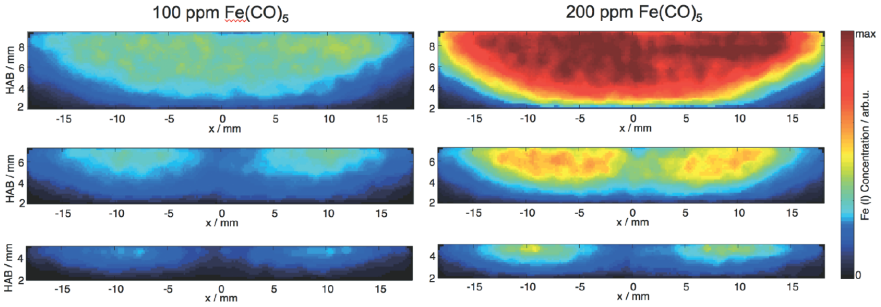

Figure 7.23: Measured semi-quantitative iron atom concentration within the DU-R flame doped with 100 ppm (left) and 200 ppm (right) $Fe(CO)_5$ at the probe position of 5 mm (bottom), 7 mm (middle) and 9 mm (top). Reprinted with permission [12].

FeO is one of the most important products of Fe and reacts further towards iron-oxide particles. In the present work, the FeO concentration in the TA-R was measured by ICLAS in the 611 nm band range. Compared to the DU-R flame, the increased size of the burner and relatively higher pressure in the TA-R result in a reduced cold gas velocity and a shorter reaction zone, and a different spatial distribution of the species. Even though the setups for the two reactors are slightly different, their results can be compared qualitatively.

Kluge et al. CrystEngComm (2015), figures are reprinted with permission.

Figure 7.24 shows the dependence of the measured FeO absorbance profile and the multiline OH-LIF measured temperature profile on the HAB. Further shown is the computed Fe and FeO mole fraction of the 1-D Cantera simulation using the measured temperature profile as an input. The computed FeO mole fraction is in good agreement with the measurements. An interesting finding is the structure of the Fe profile. The Fe concentration rises suddenly within the first millimeter downstream from the burner head, due to the initial pyrolysis of $Fe(CO)_5$ at early stage of reaction. Nevertheless, the immediate drop of Fe concentration after the first peak is somewhat unclear. It might be attributed to the formation of iron clusters, which is followed by the thermal decomposition of iron clusters that release iron atoms starting from about 3 mm HAB. Therefore, the second peak is formed at roughly 6 mm from the burner head. It is worth mentioning that the formation of FeO is not related to the sink of Fe atoms, as the Fe concentration is five times higher than the FeO concentration.

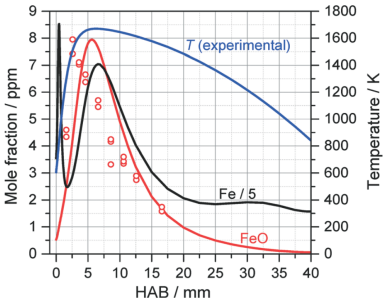

Figure 7.24: Comparison between computed FeO concentration (red line) and ICLAS measurements (open circles) for the TA-R flame doped with 900 ppm $Fe(CO)_5$. Measured temperature (blue line) and computed iron atom concentration (black line) are also plotted. Reprinted with permission [12].

The spatial distribution of computed temperature and Fe concentration of the TA-R flame with probe position of 7 mm is displayed in Figure 7.25. As mentioned, the sequence of early decomposition of $Fe(CO)_5$, the formation of iron atoms and the growth of iron clusters leads to a two-peak structure of the Fe concentration within the TA-R flame. The 2-D simulated Fe concentration is shown on the RHS of Figure 7.25, confirming such a structure in the 1-D simulation. The 2-D simulation over-predicts the temperature of the flame. This might be attributed to the uncertainties in the temperature boundary condition at the probe surface.

The PMS and the QCM were used in TA-R to investigate the nucleation within the flame. For the TA-R, the flames doped with $Fe(CO)_5$ show a strong luminosity arising from a narrow region in the vicinity of the flame front. This effect arises probably due to the blackbody radiation from hot, nascent nanoparticles. This observation is consistent with the

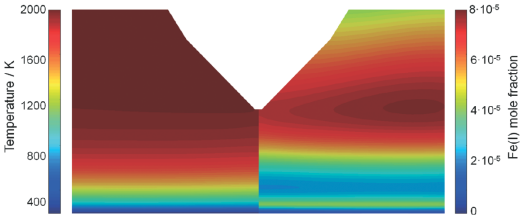

Figure 7.25: Computed temperature and iron atom concentration field for TA-R flame with a probe 7 mm away from the burner. The early formation of Fe-particle precursors is in a good agreement with 1-D simulation, while the temperature is over-predicted. Reprinted with permission [12].

QCM measurement in the vicinity of the burner head, where substantial nanoparticles were found in the preheated zone. The mass concentration of those particles drop at roughly 6 mm downstream of the burner head, as shown in Figure 7.26 left. The Measurements of PMS at varied HAB were carried out simultaneously to the QCM measurements. Based on the measured current dependence on the deflected voltage, a probability density distribution of the mean mass of the particles is derived and shown in Figure 7.26 right. It can be seen that the mean mass of the particle is consistent with the measured particle mass concentration and the maximal nanoparticle mean mass decreases four-fold over 5 mm close to the flame front. The phenomena that the early nanoparticles vanish once they pass the flame front, might be explained by their evaporation/oxidation in the high temperature area downstream of the flame, as suggested in the work of Fomin et al. [176]. Another interesting feature in Figure 7.26 left is a slight increase of the QCM signal starting from 50 mm away from the burner head. Here, nucleated species measured by the QCM cannot originate from Fe or FeO, due to the disappearance of Fe atoms and FeO from 25 mm HAB in the measurement of ICLAS (see Figure 7.24). Assuming that neither FeO nor Fe is the origin of condensable species, condensation occurs most probably from $Fe(OH)_2$ and FeOOH, and leads to iron-oxide polymorphs that are commonly observed from the flame synthesis.

The PMS was also applied for the DU-R, and a similar behavior of early particles was observed. As shown in Figure 7.27 left, the condensed species measured by QCM exit only in a very narrow region from 1 mm to 8 mm HAB. Further shown are the computed mass concentration profiles of Fe_n (n= 2-8) that indicates all iron mass except for the iron atoms or gaseous species. The unperturbed 1-D flame simulation using Cantera with the detailed chemistry yields a similar shape of the measured condensed species. In order to investigate the perturbation by the probe nozzle and better interpret the measurements, 2-D Openfoam simulations were conducted for probe positions of 2, 4, 6, 8, and 10 mm. Simulation results were extracted from five sampling positions at the center of the probe orifice. They show good agreement with the measurements and a clear shift compared to the unperturbed Fe_n profile, due to the suction of the probe. Further, the mass concentration of Fe_n was reconstructed by

Kluge et al. CrystEngComm (2015), figures are reprinted with permission.

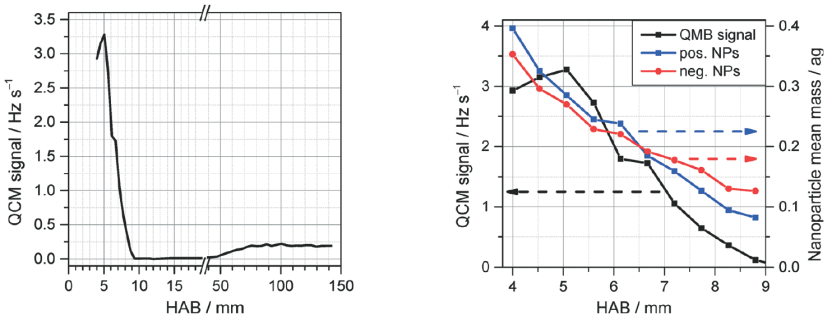

Figure 7.26: Measurements of nanoparticle mass concentration. Left: QCM signal proportional to nanoparticle mass concentration as a function of HAB for TA-R. Right: scale-up of the peak of nanoparticle formation along with the PMS measured mean mass of positively and negatively charged nanoparticle. Reprinted with permission [12].

1-D Cantera flame model using the aforementioned post processing methodology with the detailed mechanism. An improved result can be observed compared to the measurements. The agreement between the simulations and the measurements suggests that the condensed species sampled by the QCM in the short region of 2-8 mm HAB consist of iron nanoparticles.

Similar to Figure 7.24, the temperature measured with multiline NO-LIF was used as an input for the 1-D Cantera simulation to calculate Fe and FeO concentration (see Figure 7.27 right). For the concentration of Fe atoms, a good agreement is found compared to the Fe-LIF measurement. The calculated FeO concentration is nearly 10 times less than Fe concentration.

A combined experimental and modeling approach was presented in the current work to investigate the important steps towards the initial formation of iron nanoparticles in two reactor systems. Moreover, the probing effect on flame temperature and concentration of Fe atoms were evaluated. The consistent findings in two reactor systems are discussed in the following. The $Fe(CO)_5$ precursor is easily decomposed after leaving the burner surface. When the concentration of $Fe(CO)_5$ added to the flame is sufficiently high, the decomposition of $Fe(CO)_5$ provides enough iron atoms for a homogenous nucleation, which occurs a few millimeters downstream of the burner head, and leads to a substantial amount of iron nanoparticles that could be detected by the PMS and the QCM. Simultaneously FeO molecules are formed at a ratio of $\sim$ 20% related to the iron atom concentration. These nanoparticles travel with the gas flow and pass through the flame front, where the temperature is high enough (up to 1700 K) to decompose both the iron nanoparticles and the FeO molecules. Further downstream as the temperature decreases, the nucleated species are formed again. Due to the fact both the Fe and the FeO molecules almost vanish at this position, most likely the nanoparticles originate from other molecules, such as FeOOH and

Kluge et al. CrystEngComm (2015), figures are reprinted with permission.

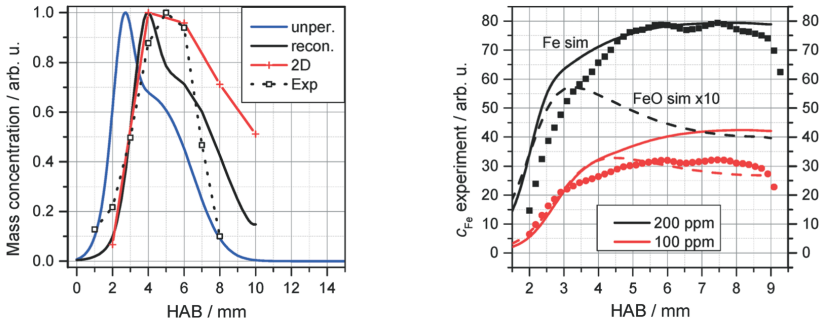

Figure 7.27: Measurements of nanoparticle mass concentration in DU-R. Left: normalized QCM signal (symbols/dotted line) as a function of HAB for DU-R doped with 200 ppm $Fe(CO)_5$, simulated Fe_n species concentration from 1-D unperturbed Cantera simulation (blue line), 2-D Openfoam simulation (red line) and reconstructed 1-D simulation (black line). Right: normalized LIF measured Fe concentration (symbols) for 100 ppm and 200 ppm $Fe(CO)_5$, computed Fe and FeO concentration by 1-D simulation using multiline NO-LIF measured temperature profile as an input. Reprinted with permission [12].

$Fe(OH)_2$. The sampling nozzle significantly modifies the temperature field and the concentration field of Fe in the vicinity of the burner. This effect becomes weak once the sample nozzle is moved to the higher position (> 9 mm) relative to the burner surface. Based on a post processing approach, the Fe_n concentration is calculated and shows good agreement comparing against the experimental measurements.

7.4 Effect of stagnation-plate and sampling orifice on an ambient flame [159]

Most parts of this section were previously published in 'Combustion and Flame 162 (10), J. Camacho, C. Liu, C. Gu, H. Lin, Z. Huang, Q. Tang, X. You, C. Saggese, Y. Li, H. Jung, L. Deng, I. Wlokas and H. Wang, Mobility Size and Mass of Nascent Soot Particles in a Benchmark Premixed Ethylene Flame, 3810-3822 (2015)' and figures are reprinted with permission. The author L. Deng implemented the detailed models for viscosity and thermal conductivity of the gas phase and diffusive transport for species, ran all CFD simulations and 1-D Cantera simulations and generated parts of the figures. The author J. Camacho conducted the experiments at University Stanford, wrote the paper and generated most parts of figures. The author C. Liu conducted the experiments at Stanford University. The authors C. Gu and H. Lin conducted the experiments at Shanghai Jiao Tong University. The authors Q. Tang conducted the experiments at Tsinghua University. The author C. Saggese ran all 1-D OPPDIF simulations. The author Y. Li conducted

Kluge et al. CrystEngComm (2015), figures are reprinted with permission.

the experiments at University of California Riverside. The authors Z. Huang, X. You, H. Jung, I. Wlokas and H. Wang contributed guidance, corrections, discussions and proof-reading.

In this section, the simulations and the results for a burner stabilized stagnation flame will be shown. The configuration of the flame and the experimental approaches were introduced in section 6.4. The simulation focused on the influence of the sampling orifice on the flame. Furthermore, the effects from the sampling orifice on the relevant species for soot particles formation were evaluated. At the end, two suggestions are proposed for the improvement of the 1-D modeling approach for the soot particles in future work.

Kinetic modeling

The mechanism USC Mech II is a $H_2/CO/C_1$-C_4 kinetic model consisting of 111 species and 784 reactions [177]. This mechanism includes a comprehensive reaction model for ethylene combustion and was chosen for 1-D simulations. For 2-D simulations, the computational cost of the USC Mech II is prohibitive so that its reduced 32-species mechanism developed by Luo et al. [178] was employed.

Simulation

The experimental configuration was modeled first by a 1-D stagnation flame at two universities using two different methods: a modified version of OPPDIF [163] at Stanford, and Cantera [119] at Duisburg. For OPPDIF simulations, the transport equations were discretized by the conventional differencing techniques and the species diffusion was modeled using a multicomponent approach, taking thermal diffusion into account. Heat release rates and transport properties were determined by Sandia CHEMKIN [44] and TRANFIT [179], respectively. Heat loss induced by radiation of CO_2 and H_2O were taken into account as well. The OPPDIF features an adaptive mesh that resolves the flame with roughly 200 cells.

In contrast to the OPPDIF simulations, the Cantera simulations employed a mixture-averaged formula for the calculation of species diffusion and thermal diffusion was not considered. Furthermore, the radiative heat loss from CO_2 and H_2O was not considered.

The 2-D axisymmetric simulations were conducted using Openfoam. The methods for the numerical solution have been discussed in chapter 2 and 4. Here, it is worth mentioning again that the simulations focus on the prediction of the flame and the flow field. Neither soot formation nor the radiative heat loss from the gas species or soot particles were considered in the 2-D simulation. The simulation domain was an axisymmetric wedge with a radial extent of 50 cm, including the coflow region. The simulations were carried out at five relevant sampling position (H_p = 0.55, 0.6, 0.7, 0.8 and 1.0 cm), where the case of H_p = 1 cm was resolved on a grid of 56,200 cells with 10 cells across the orifice. In order to check the convergence of the solution, the simulation was repeated on a coarse grid of 12,300 cells and a low orifice resolution (5 cells). Nearly the same flame temperature and velocity field were obtained.

Camacho et al. Combust. Flame (2015), figures are reprinted with permission.

In order to obtain the boundary condition for the experimental condition, the burner temperature was set to the extrapolated gas temperature measured in the vicinity of the burner surface. The stagnation surface was treated as a no-slip wall, whose temperature was measured by a plate-embedded thermocouple. The flow at inlet was a uniform plug flow with the mass flux given by the cold gas velocity and the gas composition in the experiment. For the 1-D simulations, the species flux were determined from a weighted function of convective flux and diffusive flux ($\dot{m}''\varepsilon_k = \dot{m}''Y_k + J_k$), well know as Robin boundary condition, whereas the diffusive flux was suppressed for the 2-D simulations. However, these two approaches yielded the similar species fluxes. For the 2-D simulations, the stagnation plate with and without the sampling orifice was simulated. In the presence of the orifice, a pressure drop corresponding to the experimental condition was imposed on the orifice to form a finite flow through the orifice.

Results and discussion

The comparison between the measured and the computed axial flame temperature with the stagnation plate at various positions is shown in Figure 7.28. By applying the 1-D stagnation flame model in Cantera, the temperature profile predicted by the 32-species skeletal mechanism was first compared against the temperature profile calculated by the USC Mech II to check the accuracy of the reduced mechanism. An agreement among the computed temperatures and the low computational cost of the 32-species mechanism suggests its suitability for the 2-D simulations. The overlap of the computed temperatures from all 1-D simulations shows a satisfying agreement between the models implemented in Cantera and OPPDIF, which even employ the slightly different physical models (the species diffusion and the radiative heat loss). Moreover, the agreement between the 2-D simulations with a closed orifice and the 1-D simulations indicates that the investigated flame can be well predicted by a pseudo 1-D stagnation flow model. Also observed in Figure 7.28 is that the computed temperatures match the measured temperatures well except in the post-flame region. The discrepancy might be attributed to the changes in the emissivity of the thermocouple resulting from soot deposition on surface. Another potential uncertainty is the drag on the wire caused by the flow. The effect of the drag may decrease significantly when the measurements were performed in the vicinity of the burner surface. In contrast to all other simulation results, the 2-D simulations considering the orifice predicted a relatively higher temperature downstream the flame (up to 300 K). This might be explained by the aerodynamic effect induced by the sampling orifice. Instead of the cold stagnation plate, a finite flow with high temperature passes through the orifice and leads to a increased temperature profile in the vicinity of the orifice. More details for the probing effect will be discussed in the following.

A strong temperature gradient is shown on the LHS of Figure 7.29, indicating a strong cooling effect of the stagnation plate. On the RHS, the mole fraction of CH_3 is displayed to present the position of a flat flame. Figure 7.29 top presents the sampling zone for the soot samples. Due to a pressure drop of 0.01 bar at the orifice (the dilution ratio of ∼400), the gas velocity exceeds linearly 50 m/s in the orifice, leading to a half spherical sampling

Camacho et al. Combust. Flame (2015), figures are reprinted with permission.

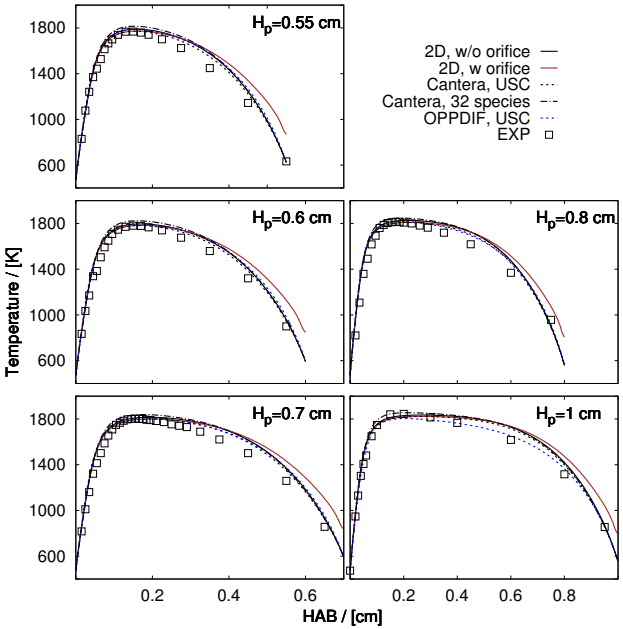

Figure 7.28: Comparison of the measured (symbols, [161]) and computed (lines) temperature profile of the stagnation flame. 2D, w/o orifice: 2-D simulations without the influence from orifice flow, 2D, w orifice: 2-D simulations considering orifice flow, Cantera, USC: 1-D Cantera simulations using reaction mechanism USC-Mech II, Cantera, 32 species: 1-D simulations using 32-species skeletal mechanism, OPPDIF, USC: 1-D OPPDIF simulation using reaction mechanism USC-Mech II, EXP: measurements.

zone with a radius around 2 mm. Hence, instead of a single value at a sampling point in the center of the orifice, the experimental result becomes an averaged sampled value over the whole sampling zone. It is important to notice that the assumed 1-D stagnation flow model is only valid outside the sampling zone.

To further evaluate the aforementioned sampling effects, the results of the 1-D stagnation flame simulation and the 2-D simulation with a flow through the orifice are compared. The temperatures and the axial velocities along the centerline of the flame for $H_p = 0.8$ cm are shown in Figure 7.30. Two significant effects highlight the influence of the orifice. The first effect (thermodynamic effect) is the slightly higher temperature of the post flame computed by the 2-D simulation at the "stagnation point", as already shown in Figure 7.28. The second

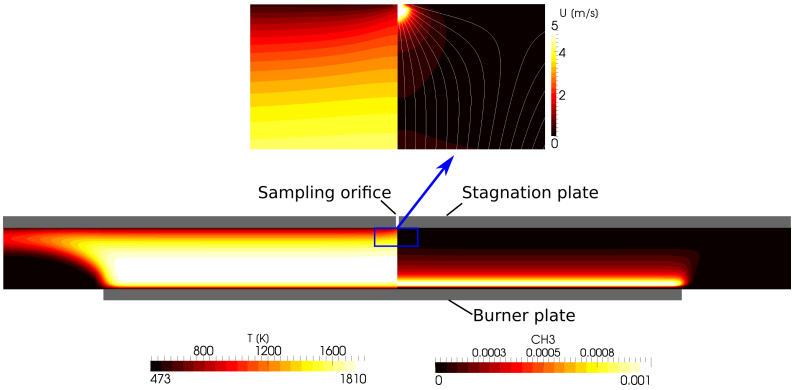

Figure 7.29: The temperature field (LHS) and mole fraction of CH_3 (RHS) for $H_p = 0.8$ cm shows the strong impact of the stagnation plate on the flame. The sampling zone (LHS: temperature, RHS: velocity) is scaled up to indicate the influence of the sampling orifice.

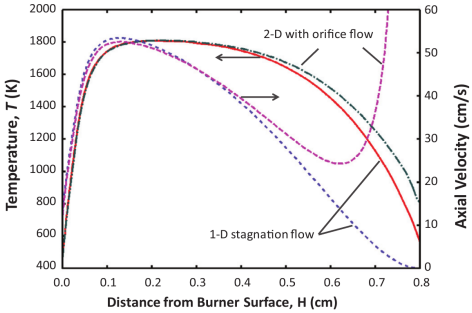

Figure 7.30: Comparison of the temperature along centerline and the axial velocity for $H_p = 0.8$ cm from the 1-D stagnation flame simulation and from the 2-D simulation with an orifice flow. Reprinted with permission [159].

effect (aerodynamic effect) is a drastic increase of the axial velocity, due to the convective orifice flow.

In order to distinguish the thermodynamic effect and the aerodynamic effect on the relevant species for the formation of soot particles, two separate 1-D Cantera simulations were carried out. The first applies the temperature profile and the second uses both the temperature and the velocity profiles from Figure 7.30. A big advantage of this approach is

that the simplification error of the reduced mechanism can be compensated by detailed 1-D simulations of ethylene flame using USC-Mech II. As illustrated in Figure 7.31, compared to the unperturbed 1-D ideal flame simulation, the simulation employing the "reconstructed" temperature profile shows a significant deviation downstream of the flame, due to the temperature increase (around 200 K) there. Notably, the thermodynamic effect on the C_6H_4 is extremely strong, and the deviation attains around 30 %. However, this bias is reduced by the aerodynamic effect, whereas for other species shown in Figure 7.31 the suction of the sampling nozzle enhances the distortion. These findings shed light on the further investigations of probing effects on the PSDF. A modeling of the PSDF using the 1-D stagnation flow model taking the convective flow through the orifice into account should yield an accurate result against the experiment.

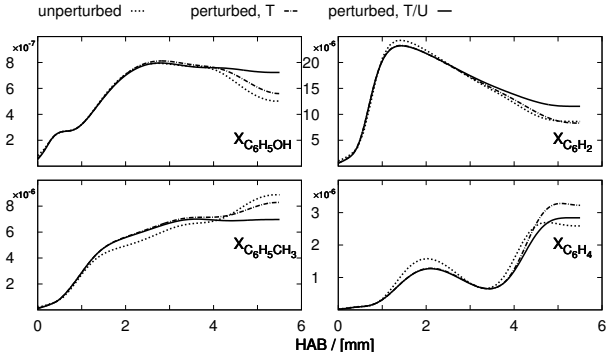

Figure 7.31: Mole fractions of the relevant species for the formation of soot particles for different cases, unperturbed: results calculated from ideal stagnation model, perturbed, T: results calculated from 1-D simulation using the "reconstructed" temperature profile of the flame, perturbed T/U:results calculated from 1-D simulation using the "reconstructed" temperature profile and velocity profile of the flame.

Figure 7.32 shows a comparison between the convective flow time (the time a fluid element needs to pass through the centerline of the flow) for the 1-D simulation and for the 2-D simulation with orifice flow. For the current case with a dilution ratio of $\sim$ 400, the soot samples passing through the orifice need several milliseconds. For other varied dilution ratios, the flow rate through the orifice may lead to different sizes of the sampling zones and a range of the residence time of the samples. However, in the experiments [159] it was found that the PSDF is insensitive to the dilution ratio. This might be explained by the surface reaction or the slow coagulation that can hardly affect the PSDF when the samples approach the orifice.

Further efforts are needed to develop a proper 1-D model that is suitable for this type of

Camacho et al. Combust. Flame (2015), figures are reprinted with permission.

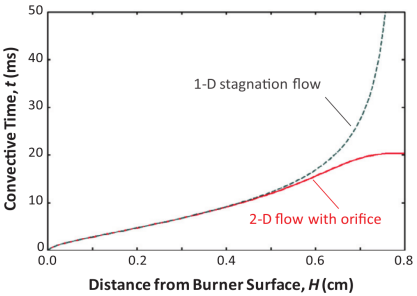

Figure 7.32: Comparison of the convective flow time obtained from the 1-D stagnation flame simulation and from the 2-D simulation with a orifice flow. Reprinted with permission [159].

experiments. The presented work yields two suggestions that can improve the comparison between the measurements and the model prediction. First, as mentioned, the modeling of the PSDF should take into account the convective flow through the orifice. Second, the 1-D pseudo stagnation flow model is valid along the centerline up to the last 2 mm (radius of the sampling zone), and this position can be considered to be the upstream limit for the comparison of measurement and simulation.

Camacho et al. Combust. Flame (2015), figures are reprinted with permission.

7.5 Effect of geometric configuration of the reactor on the flame [25]

This section was previously published in 'Proceedings of the Combustion Institute, O. M. Feroughi, L. Deng, S. Kluge, T. Dreier, H. Wiggers, I. Wlokas and C. Schulz, Experimental and numerical study of a HMDSO-seeded premixed laminar low-pressure flame for SiO_2 nanoparticle synthesis (2016)' and figures are reprinted with permission. The author L. Deng implemented the detailed models for viscosity and thermal conductivity of the gas phase and diffusive transport of species and Kruis' model, ran all simulations, generated parts of the figures. The author O. M. Feroughi conducted the LIF measurements, wrote the paper and generated most parts of figures. The author S. Kluge conducted the PMS measurements. The authors T. Dreier, H. Wiggers, I. Wlokas and C. Schulz contributed guidance, corrections, discussions and proof-reading.

The simulation and the results for a premixed H_2/O_2/Ar flame doped with HMDSO in a low pressure reactor will be shown in this section. The configuration of the flame and the experimental approaches were introduced in section 6.5. Simulation of the investigated H_2/O_2/Ar flame doped with HMDSO requires the modeling of HMDSO combustion. Furthermore, the modeling of SiO_2 particle formation is necessary for the calculation of the particle size. For the current work, two reaction mechanisms (simple- and detailed mechanism) were used and will be discussed as follows.

Kinetic modeling

For both mechanisms, two major and separate steps need to be taken into account to address the formation of silica particles. The first step is the decomposition and the combustion of the silicon-containing precursor. For both mechanisms, this step is described by a one step reaction by assuming a fast pyrolysis followed by the oxidation of HMDSO towards SiO. The two mechanisms are distinguished in the second step, which is the formation of $SiO_{2(g)}$ (index g denotes the gas phase) and the nucleation of particles. In the detailed mechanism, the formation of $SiO_{2(g)}$ and the nucleation of particles are accounted for by a detailed SiO mechanism extracted from the mechanism proposed by Miller et al. [180]. This detailed SiO sub-mechanism excludes the reactions that contradict the experimental observations and optimizes the remaining reactions to resemble the late formation of silica particles. In the simple mechanism, the consumption of SiO and the formation of $SiO_{2(g)}$ are described by a one step reaction, where SiO reacts with H_2O. For the simple mechanism, the reaction rate of the two reactions were adjusted to successfully predict the relative SiO concentration profile of the flame doped with 200 ppm HMDSO. The simple mechanism was further validated against the experimental results of the flame doped with 1000 ppm and 2000 ppm HMDSO separately, and a satisfactory agreement was obtained.

In the present work, these two mechanisms are further added to the C1 reaction mechanism developed by Li et al. [181] to account for combustion of a premixed H_2/O_2 flame. In addition, the combustion of CH_3, that is generated from the decomposition of the HMDSO,

is included. The detailed reaction mechanism contains 93 reactions and is used for the 1-D simulation. For the 2-D simulations, the simple mechanism was reduced by employing the approach proposed by Sikalo et al. [55], leading to a 29-steps mechanism. The details about these two mechanism are given by Feroughi et al. [25]. Furthermore, the detailed mechanism proposed by Li et al. [32], consisting of 11 species and 25 reactions, was used for the 3-D simulations of the flame without the HMDSO.

Simulation

The flame without HMDSO was first investigated by 3-D simulations, where the geometry of the reactor housing was represented by a 3-D, symmetric section of the apparatus. The multiline NO LIF measurements were conducted at five different positions of the optical window, resulting in various geometric configurations. Therefore, five separate simulations using the corresponding numerical domains (each consists of 130,554 cells) were carried out. The inlet velocity at the burner surface and the optical windows was set according to the mass flow rate employed in the experiments. To consider the heat loss of the reactor housing, an isothermal boundary condition was applied on the outer wall of the reactor.

As mentioned, the reaction mechanism for the HMDSO combustion and the SiO_2 particle formation is computationally too expensive and here prohibitive for the 3-D simulation. Therefore, the flame doped with HMDSO is described by a 2-D simulation using an axisymmetric domain. The impact of the PMS sampling nozzle was not considered, as the sampling was conducted far downstream of the flame and only a small spatial shift of few nozzle diameters could be expected (shown in [12]).

The sub-mechanism considering $SiO_{2(g)}$ formation was validated indirectly by the means of the mean particle diameter measured by the PMS system. The particle dynamics were simulated employing the model proposed by Kruis et al. [67], with the extension of a nucleation term. Due to the high Schmidt number ($Sc > 1000$) and high Knudsen number ($Kn > 100$), particle diffusion and slip correction were neglected. Instead of extrapolated, measured temperature profiles, the simulated temperature was used as an input for the simulation of particle dynamics downstream the flame up to 360 mm.

Results and discussion

In the present work, the temperature was measured by multi-line NO-LIF thermometry. Figure 7.33 (left) shows a comparison of the computed and the measured temperature distribution. For the measurements, the temperature fields of the flame without precursor addition were measured as the illuminating laser sheet ($70{\times}50\ mm^2$) at five burner positions. Every two neighboring positions have a shift of 40 mm with an overlap of 5 mm. In the experiment, the burner head was shifted to different positions for the laser measurement. Therefore, notable discontinuities in the temperature field were caused by the modified geometric configurations. This effect was also captured by the simulations including the complete geometric features.

Feroughi et al. Proc. Combust. Inst. (2016), figures are reprinted with permission.

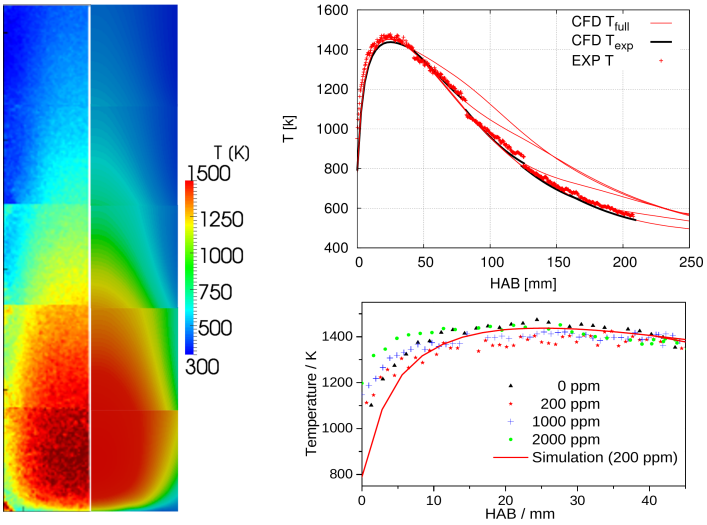

Figure 7.33: Comparison between the measured and the computed temperature of the investigated flame. Left: Temperature field (without HMDSO) of the reactor. Right top: temperature (without HMDSO) along the centerline as a function of HAB. Right bottom: enlarged zone form 0 to 45 mm HAB for the temperature of flame doped with varied HMDSO concentration. Reprinted with permission [25].

The temperature of the flame without the precursor addition along the centerline is plotted in Figure 7.33 (right top), where the temperature measurement and the simulation results are in good agreement. Also shown are the aforementioned significant discontinuities, in both measurements and simulations. Figure 7.33 (right bottom) presents the temperature along the centerline of the flames doped with the varied amount of the precursor concentrations for the HAB $0 \sim 50$ mm. A similar behavior is observed for all flames, the temperature of the gas phase increases to a maximum of around 1460 K at 20 mm HAB, afterward cooling takes place downstream of the flame. Only a slight influence of the different amount of precursor addition was found at the first 10 mm HAB, even the equivalence ratio increases with the increasing precursor concentrations ($\phi = 0.39$, 0.4, 0.42, and 0.455 for 0, 200, 1000, and 2000 ppm, respectively). Although the simulated temperature profile matches the temperature measurement well at HAB starting from 10 mm, a significant discrepancy appears in the vicinity of the burner surface, which might be induced by the uncertainty in the temperature boundary condition on the inlet. Therefore, the measured temperature of the flame with 200 ppm HMDSO at HAB<100 mm was used for the development of a reac-

tion mechanism for the HMDSO combustion. Encouraged by the agreement between the temperature measurement and the simulation at HAB>10 mm and the fact that particles grow staring from 150 mm HAB (see Figure 7.36), for the calculation regarding the particle dynamics the computed temperature was employed.

The 2-D simulated and the LIF measured, relative mole fractions of SiO along the center line for three different precursor concentrations are shown in Figure 7.34. These values are normalized to the maximal SiO mole fraction with 2000 ppm HMDSO. For all precursor concentrations, the SiO is formed in the region of 0-30 mm HAB. Further, the similar shape and peak value are predicted in the simulation and the measurement. Only for the case with 2000 ppm HMDSO, a double peak occurs in the measurement. This peak was also observed in other works using other silica precursors [182, 172, 183]. This effect is possibly induced by the precursor decomposition (1st peak) and the subsequent sublimation of SiO from the formed nanoparticles (2nd peak).

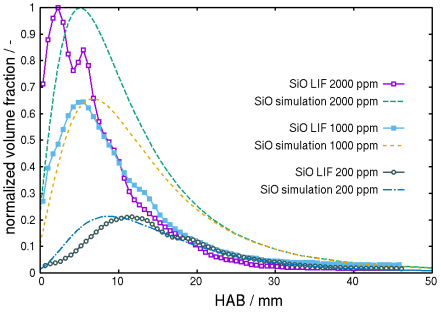

Figure 7.34: Dependence of relative SiO mole fraction on the HAB for varied precursor concentrations. Reprinted with permission [25].

In Figure 7.35, a comparison between two reaction mechanisms is shown, where the relative mole fractions of SiO and $SiO_{2(g)}$ were calculated using a 1-D Cantera premixed flame model employing the temperature profile (see red line in Figure 7.34) calculated from the 2-D Openfoam simulation. In addition, the LIF-measured SiO is displayed. All the data are normalized to show a qualitative comparison. For all HMDSO concentrations, a satisfactory agreement is achieved between the two mechanisms and between the measurements and the simulation results. It is interesting to notice that even if the detailed mechanism is used for the description of SiO consumption and SiO_2 formation, the simulation can still not predict the two-peak of the SiO mole fraction. This is most probably due to the simplification of the reaction path for the combustion of the precursor.

The robustness and satisfactory accuracy of the simple mechanism (see Figure 7.35) ensures its applicability for the CFD simulation. For the simulation of the particle dynamics, the detailed mechanism and the simple mechanism yield the same solution. This might be

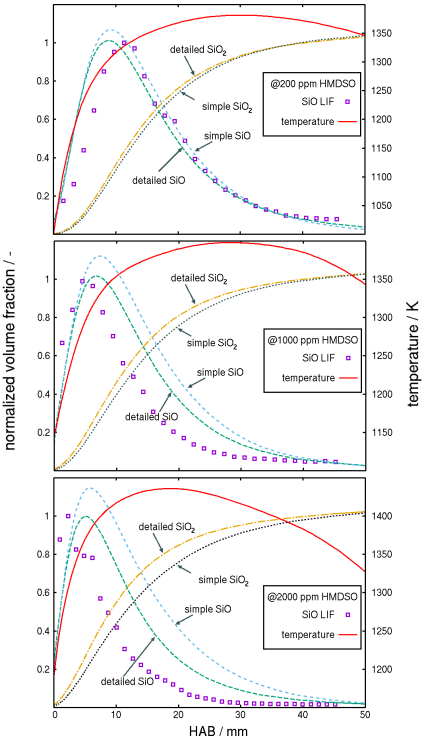

Figure 7.35: Comparison of mechanisms with different HMDSO concentrations, "detailed" and "simple" correspond respectively to the detailed and the simple mechanism. Reprinted with permission [25].

attributed to the fact that the nucleation of silica particle takes place far downstream of the flame (150 mm HAB) and the $SiO_{2(g)}$ mole fraction reaches the maximum already at about 25 mm HAB. Therefore, the particle formation could be insensitive to the small deviation in the kinetics. The PMS measured and the computed particle size are shown in Figure 7.36, where the particle increase in the size with increasing concentration of the precursor. A good agreement is achieved between the measurements and the simulation results.

A set of *in situ* and inline diagnostics including multi-line LIF thermometry, SiO-LIF and PMS for SiO_2 nanoparticle were employed for the investigation of HMDSO-doped premixed H_2/O_2 flat flames. The goal of this investigation was to provide as much as possible input

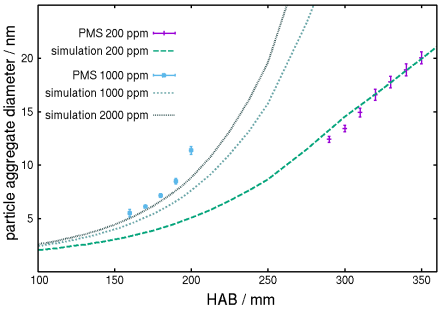

Figure 7.36: Comparison of PMS measured and computed particle size with different HMDSO concentration. Reprinted with permission [25].

information for the development of the kinetic modeling (SiO to $SiO_{2(g)}$), as well as indirect information (particle size) for validation. As a complementary tool, CFD simulations helped to understand the discontinuities of the measured temperatures and gave the temperature fields far downstream of the flame, where the reactor was not accessible for multi-line LIF thermometry due to geometric constraints. The proposed simple two-step reactions for the formation of silica particles was proven to be consistent with the detailed mechanism and showed a good agreement with the PMS measurements.

Feroughi et al. Proc. Combust. Inst. (2016), figures are reprinted with permission.

Chapter 8

Conclusion

The current thesis presents a variety of simulations of experiments that investigated flame structure, nanoparticle synthesis and soot particle formation individually. By the means of CFD simulation, the uncertainties in measurements induced by thermodynamic and gas dynamic effects or geometric constraints of the reactor were investigated; the errors in the measurements were quantified and corrected.

First, the impact of a probing nozzle on the examined one-dimensional laminar flames was explored. A conjugate heat transfer model within the solid nozzle was applied to overcome the uncertainty in the temperature boundary on the outer surface of the nozzle. The individual effects caused by heat transfer and by flow field distortion could be identified and distinguished. It was found that once the thermal steady state was attained, thermal distortion of the sampling nozzle became negligible and the fluid mechanic effect tended to be dominant: the deformation of the flame caused by the suction effect of the probe is the main mechanism that perturbed the flame. Further, the inhomogeneity arising from the perforated burner plate was investigated. Although a weak effect was observed for the stable species, a notable impact on the radicals like H and OH was found. Furthermore, a simulation work-flow with a combination of two- and three-dimensional CFD simulations and one-dimensional, detailed kinetics simulations was shown to be effective and accurate. The comparison of the simulation results with the experimental data demonstrated that CFD simulations enable a better interpretation of species concentration measurements in absence of temperature and flow field measurements. Furthermore, measurements at short distances from the burner surface demand a high level of homogeneity in the flow, as demonstrated by our simulations.

Similar probing effects were examined within the flame reactor at University Duisburg-Essen. As already addressed by the work of Weise et al. [149], the flow field within such a simple and straightforward reactor can be complex and needs to be carefully explored. Weise et al. [149] showed that the buoyancy force lifts the center of the flame upwards in the horizontally aligned reactors, and thus suggested a vertical alignment of the reactor. An interesting finding of the present work is that even in the vertically aligned reactor, buoyancy can modify the flow field far downstream. For the investigated experiments, the

measurements were conducted only at low HAB, and therefore the buoyancy effect could be neglected. However, care should be taken when this type of reactor is used for the investigation of nanoparticles or soot particles, as the same effect may strongly influence the experimental results. The sampling nozzle strongly affects the species concentration of the flame. The simulation results and the measurements were in good agreement, showing CFD simulation is able to complement the existing measurement techniques. In particular, the calibration of probes could be perhaps performed using predictions from simulations in absence of the temperature measurements.

In the third part of this thesis, the probing effect in context of nanoparticle synthesis was investigated. The focus of this work was on the investigation of the initial steps towards the formation of iron-oxide particles in flame reactors in Duisburg and in Tel Aviv. A set of sophisticated measurement techniques was applied, including laser-induced fluorescence for the measurement of spatial distribution of iron atoms in the Duisburg reactor and intracavity laser absorption spectrometry for FeO molecules in the Tel Aviv reactor. For both reactors, the molecular beam technique was combined with a particle mass spectrometry and a quartz crystal microbalance to measure spatially resolved the condensed matters in the flame. Furthermore, the spatial temperature distribution was measured by multiline NO-LIF thermometry and two-line OH-LIF in the Duisburg reactor and in the Tel Aviv reactor, respectively. Extensive experimental data in combination with simulation results yielded the comprehensive interpretation with respect to the process of initial early particle formation. Both, the measurements and the simulation results demonstrated that the initial decomposition of the precursor in the vicinity of the burner surface leads to the formation of early iron particles due to homogenous nucleation. At this stage, the FeO molecules were also formed. Once they passed the flame front, both iron particle and FeO molecules vanished, due to thermal decomposition. Further downstream of the flame, iron-oxide particles were formed and detected by the particle mass spectrometry. It seems that the formation of iron-oxide particles relies on molecules such as FeOOH and $Fe(OH)_2$, as iron and FeO molecules disappear at this position. A further finding is that at HAB $<$ 9mm, the probing nozzle can strongly distort the flame in temperature and species fields. However, for HAB $>$ 9mm, the probing effect becomes weak and hardly influences the flame. Moreover, the simulated condensed material ($Fe_{2\sim8}$) concentration was qualitatively compared to the QCM at the different probe positions. An overall satisfactory agreement suggested the capability of CFD simulation to predict the probing effect in the experimental measurements.

In the subsequent part of the thesis, the probing effect on a stagnation flame was studied by the means of 2-D axis symmetric simulation. The study focused on the effect from the sampling orifice on the assumption of one dimensional flame configuration, and further the influence on the measured particle size distribution. The computed temperature profiles were compared with the measurements for various stagnation plate positions. An overall good agreement suggested the robustness and reliability of the modeling methods for the investigated flame configuration. This encouraged the studies of soot particle size distribution in such a flame configuration. The sampling probe caused a sampling zone, likely a 0.2 cm radius half-sphere in front of the orifice, where the flow was highly accelerated while the

gas samples were drawn into the orifice. Despite a small sampling volume, the measured soot particles should be an average of the samples within that volume. Therefore, two suggestions were proposed to improve the comparison of measurement against 1-D simulation results. The 1-D stagnation flow model should address the finite convective velocity caused by the sampling orifice to preserve the real flow conditions through the probe. An alternative is to consider 0.2 cm ahead of the stagnation point as an upstream limit, which enabled a reasonable comparison between the measurements and the simulation results.

The final part of the thesis presented *in situ* and inline diagnostics combined with CFD simulations for the investigation of SiO_2 synthesis in the gas phase from a HMDSO (hexamethyldisiloxane) doped premixed H_2/O_2 flat flame. The temperature field was determined by multi-line LIF thermometry at different burner positions. As the shift of the burner head led to modified reactor geometries, the LIF-measured temperature distribution showed clear discontinuities. This effect was confirmed by a set of 3-D CFD simulations considering the complete reactor geometry. The addition of small amounts of HMDSO to the flame had a weak influence on the temperature. By applying the SiO-LIF technique, the concentration of SiO was measured for an increasing precursor concentration. The measured temperature profile and SiO concentration were valuable for the development and validation of a simple two-step kinetics schemes including combustion of HMDSO and formation of silica particles. Furthermore, the particle size was measured by the PMS and modeled by a simple monodisperse model. The good agreement showed the validity of the proposed two-step reaction and its consistency with the detailed reaction mechanism.

This thesis demonstrated that 2-D and 3-D CFD simulations can serve as a complementary tool for the analysis of experimental results when uncertainties caused by thermodynamic and fluid dynamic effects, as well as the constrains of the experimental configuration cannot be avoided in the laboratory. The presented framework was computationally expensive, especially compared to one-dimensional simulations. Therefore, a work flow was proposed to reconstruct 1-D flame models using the temperature and the velocity along streamlines calculated from the 2-D or 3-D simulation considering perturbations. In this approach, simplification errors caused by the reduced mechanism can be avoided by using detailed reaction mechanisms with reasonable computational cost. A further improvement of reaction mechanisms by iterative optimization and validated with data obtained by the means of molecular beam mass spectrometry will require significantly higher computational power. It is expected that in the near future, with always growing computational power, iterative 2-D simulations will support the development of more accurate reaction mechanisms themselves. Another improvement for the calculation of soot particle distribution in the stagnation flame can be realized by creating a new 1-D nanoparticle model taking into account the perturbed temperature and velocity profile. An accurate PSDF (particle size distribution function) is expected once the simulations consider the effects caused by the finite convective flow through the sampling orifice. As demonstrated in this thesis, the proposed framework is robust and reliable for future studies related to laminar flames and particle formation.

Bibliography

[1] *World Energy Outlook 2011 Factsheet, International Energy Agency*. Tech. rep. 2011.

[2] J. B. Donnet. *Carbon black: science and technology*. CRC Press, 1993.

[3] J. H. Park and T. S. Sudarshan. *Chemical vapor deposition*. Vol. 2. ASM international, 2001.

[4] C. Buzea, I. Pacheco, and K. Robbie. *Biointerphases* 2.4 (2007), pp. 17–71.

[5] T. Hyeon. *Chem. Commun.* 8 (2003), pp. 927–934.

[6] S. Mornet, S. Vasseur, F. Grasset, P. Veverka, G. Goglio, A. Demourgues, J. Portier, E. Pollert, and E. Duguet. *Prog. Solid State Chem.* 34.2 (2006), pp. 237–247.

[7] M. Takafuji, S. Ide, H. Ihara, and Z. Xu. *Chem. Mater.* 16.10 (2004), pp. 1977–1983.

[8] A. H. Lu, W. Schmidt, N. Matoussevitch, H. Bönnemann, B. Spliethoff, B. Tesche, E. Bill, W. Kiefer, and F. Schüth. *Angew. Chem.* 116.33 (2004), pp. 4403–4406.

[9] A. K. Gupta and M. Gupta. *Biomaterials* 26.13 (2005), pp. 1565–1573.

[10] A. Barchanski, U. Taylor, S. Klein, S. Petersen, D. Rath, and S. Barcikowski. *Reprod. Domest. Anim.* 46.s3 (2011), pp. 42–52.

[11] N. Petermann, N. Stein, G. Schierning, R. Theissmann, B. Stoib, M. S. Brandt, C. Hecht, C. Schulz, and H. Wiggers. *J. Phys. D Appl. Phys.* 44.17 (2011), p. 174034.

[12] S. Kluge, L. Deng, O. Feroughi, F. Schneider, M. Poliak, A. Fomin, V. Tsionsky, S. Cheskis, I. Wlokas, I. Rahinov, T. Dreier, A. Kempf, H. Wiggers, and C. Schulz. *CrystEngComm* (2015), pp. 1630–1639.

[13] O. P. Korobeinichev, V. M. Shvartsberg, A. G. Shmakov, D. A. Knyazkov, and I. V. Rybitskaya. *Proc. Combust. Inst.* 31.2 (2007), pp. 2741–2748.

[14] A. N. Hayhurst. *Combust. Explos. Shock Waves* 48.5 (2012), pp. 516–525.

[15] A. D. Abid, J. Camacho, D. A. Sheen, and H. Wang. *Energ. Fuel.* 23.9 (2009), pp. 4286–4294.

[16] K. Kohse-Höinghaus, P. Oßwald, T. A. Cool, T. Kasper, N. Hansen, F. Qi, C. K. Westbrook, and P. R. Westmoreland. *Angew. Chem. Int. Edit.* 49.21 (2010), pp. 3572–3597.

[17] S. Staude, C. Hecht, I. Wlokas, C. Schulz, and B. Atakan. *Z. Phys. Chem.* 223.4-5 (2009), pp. 639–649.

[18] M. Poliak, A. Fomin, V. Tsionsky, S. Cheskis, I. Wlokas, and I. Rahinov. *Phys. Chem. Ch. Ph.* 17.1 (2015), pp. 680–685.

[19] C. E. Willert and M. Gharib. *Exp. Fluids* 10.4 (1991), pp. 181–193.

[20] J. L. Kinsey. *Annu. Rev. Phys. Chem.* 28.1 (1977), pp. 349–372.

[21] A. C. Eckbreth. *Laser diagnostics for combustion temperature and species*. Vol. 3. CRC Press, 1996.

[22] L. Deng, A. Kempf, O. Hasemann, O. P. Korobeinichev, and I. Wlokas. *Combust. Flame* 162.5 (2015), pp. 1737–1747.

[23] A. T. Hartlieb, B. Atakan, and K. Kohse-Hoeinghaus. *Combust. Flame* 121.4 (2000), pp. 610–624.

[24] C. Weise, A. Faccinetto, S. Kluge, T. Kasper, H. Wiggers, C. Schulz, I. Wlokas, and A. Kempf. *Combust. Theor. Model.* (2013), pp. 504–521.

[25] O. M. Feroughi, L. Deng, S. Kluge, T. Dreier, H. Wiggers, I. Wlokas, and C. Schulz. *Proc. Combust. Inst.* 35.3 (2016), pp. 1540–7489.

[26] T. Poinsot and D. Veynante. *Theoretical and Numerical Combustion*. 3rd. Bordeaux, France: Aquaprint, 2012.

[27] R. J. Kee, M. E. Coltrin, and P. Glarborg. *Chemically reacting flow: theory and practice*. John Wiley & Sons, 2003.

[28] C. R. wilke. *J. Chem. Phys.* 18.4 (1950), pp. 517–519.

[29] R. B. Bird, W. E. Stewart, and E. N. Lightfoot. *Transport phenomena. 2nd*. John Wiley & Sons.

[30] M. S. Mathur and S. C. Saxena. *Appl. Sci. Res.* 17.2 (1967), pp. 155–168.

[31] A. Fick. *The London, Edinburgh, and Dublin Philosophical Magazine and Journal of Science* 10.63 (1855), pp. 30–39.

[32] J. Li, Z. Zhao, A. Kazakov, and F. L. Dryer. *Int. J. Chem. Kinet.* 36.10 (2004), pp. 566–575.

[33] U. Burke, K. P. Somers, P. OToole, C. M. Zinner, N. Marquet, G. Bourque, E. L. Petersen, W. K. Metcalfe, Z. Serinyel, and H. J. Curran. *Combust. Flame* 162.2 (2015), pp. 315–330.

[34] M. J. De Witt, D. J. Dooling, and L. J. Broadbelt. *Ind. & Chem. Research* 39 (2000).

[35] W. P. Jones and R. P. Lindstedt. *Combust. Flame* 73.3 (1988), pp. 233–249.

[36] B. Magnussen and B. Hjertager. *Proc. Combust. Inst.* 16.1 (1977), pp. 719–729.

[37] D. B. Spalding. *Proc. Combust. Inst.* 13.1 (1971), pp. 649–657.

[38] B. F. Magnussen and B. H. Hjertager. *Proc. Combust. Inst.* 16.1 (1977), pp. 719–729.

[39] J. W. Gibbs. *A method of geometrical representation of the thermodynamic properties of substances by means of surfaces*. Connecticut Academy of Arts and Sciences, 1873.

[40] W. R. Smith and R. W. Missen. *Chemical reaction equilibrium analysis: theory and algorithms*. John Wiley and Sons, 1982.

[41] J. M. Smith, H. C. Van Ness, and M. M. Abbott. *Introduction to chemical engineering thermodynamics*. McGraw-Hill, 1996.

[42] S. W. Benson. *Thermochemical kinetics*. Wiley, 1976.

[43] J. B. Pedley. *Thermochemical data of organic compounds*. Springer Science & Business Media, 2012.

[44] R. J. Kee, F. M. Rupley, and J. A. Miller. *Technical Report SAND87-8215, Sandia National Laboratories* 1 (1990).

[45] M. Chase and W. Davies. *J. Phys. Chem. Ref. Data* 1 (1985).

[46] S. M. Senkan. *Adv. Chem. Eng* 18 (1992), pp. 95–196.

[47] J. F. Griffiths. *Prog. Energy Combust. Sci.* 21.1 (1995), pp. 25–107.

[48] N. Peters and B. Rogg. *Reduced kinetic mechanisms for applications in combustion systems*. Vol. 15. Springer Science & Business Media, 2008.

[49] T. F. Lu and C. K. Law. *Prog. Energ. Combust.* 35.2 (2009), pp. 192–215.

[50] T. Turányi and A. S. Tomlin. *Analysis of kinetic reaction mechanisms*. Springer, 2014.

[51] H. Z. Zhang, E. G. Eddings, A. F. Sarofim, and C. K. Westbrook. *Energ. Fuel.* 21.4 (2007), pp. 1967–1976.

[52] A. S. Tomlin, M. J. Pilling, J. H. Merkin, J. Brindley, N. Burgess, and A. Gough. *Ind. Eng. Chem. Res.* 34.11 (1995), pp. 3749–3760.

[53] A. S. Tomlin, T. Turányi, and M. J. Pilling. *Compr. Chem. Kinet.* 35 (1997), pp. 293–437.

[54] T. Lu and C. K. Law. *Combus. Flame* 154.1 (2008), pp. 153–163.

[55] N. Sikalo, O. Hasemann, C. Schulz, A. Kempf, and I. Wlokas. *Int. J. Chem. Kinet.* 46.1 (2014), pp. 41–59.

[56] N. Sikalo, O. Hasemann, C. Schulz, A. Kempf, and I. Wlokas. *Int. J. Chem. Kinet.* 47.11 (2015), pp. 695–723.

[57] G. Y. Li, H. Rabitz, and J. Tóth. *Chem. Eng. Sci.* 49.3 (1994), pp. 343–361.

[58] A. S. Tomlin, G. Y. Li, H. Rabitz, and J. Tóth. *J. Chem. Phys.* 101.2 (1994), pp. 1188–1201.

[59] H. Huang, M. Fairweather, J. F. Griffiths, A. S. Tomlin, and R.B. Brad. *Proc. Combust. Inst.* 30.1 (2005), pp. 1309–1316.

[60] T. F. Lu and C. K. Law. *Combust. Flame* 148.3 (2007), pp. 117–126.

[61] D. L. Chapman and L. K. Underhill. *J. Chem. Soci., T.* 103 (1913), pp. 496–508.

[62] U. Maas and S. B. Pope. *Combust. Flame* 88.3 (1992), pp. 239–264.

[63] H. Bongers, J. A. Van Oijen, and L. P. H. De Goey. *Proc. Combust. Inst.* 29.1 (2002), pp. 1371–1378.

[64] T. Lu, Y. Ju, and C. K. Law. *Combust. Flame* 126.1 (2001), pp. 1445–1455.

[65] N. J. Brown, G. Li, and M. L. Koszykowski. *Int. J. Chem. Kinet.* 29.6 (1997), pp. 393–414.

[66] A. Prakash, A. P. Bapat, and M. R. Zachariah. *Aerosol Sci. Tech.* 37.11 (2003), pp. 892–898.

[67] F. E. Kruis, K. A. Kusters, S. E. Pratsinis, and B. Scarlett. *Aerosol Sci. Tech.* 19.4 (1993), pp. 514–526.

[68] S. K. Friedlander. *Smoke, Dust and Haze. Fundamentals of Aerosol Dynamics*. Oxford University Press, Inc., 2000.

[69] D. Kashchiev. *Nucleation*. Butterworth-Heinemann, 2000.

[70] T. T. Kodas and M. Hampden-Smith. *Aerosol Processing of Materials*. Wiley-VCH, 1999.

[71] J. W. Gibbs. *The collected works of J. Willard Gibbs*. Vol. 1. Yale University Press, 1957.

[72] M. Volmer. *Kinetik der phasenbildung*. T. Steinkopff, 1939.

[73] R. Becker and W. Döring. *Ann. Phys.* 416.8 (1935), pp. 719–752.

[74] A. Myerson. *Handbook of industrial crystallization*. Butterworth-Heinemann, 2002.

[75] W. Kauzmann. *Kinetic Theory of Gases*. Courier Corporation, 2012.

[76] J. H. Seinfeld and S. N. Pandis. *Atmospheric Chemistry and Physics: from Air Pollution to climate Change*. John Wiley & Sons, 2016.

[77] N. A. Fuchs. *The mechanics of aerosols*. Pagamon, 1964.

[78] S. Tsantilis, H. Briesen, and S. E. Pratsinis. *Aerosol Sci. Technol.* 34.3 (2001), pp. 237–246.

[79] M. A. Asoro, D. Kovar, Y. Shao-Horn, L. F. Allard, and P. J. Ferreira. *Nanotechnol.* 21.2 (2009), pp. 025701–025707.

[80] R. M. German. *Sintering Theory and Practice*. Solar-Terrestrial Physics, 1996, p. 568.

[81] W. Koch and S. K. Friedlander. *J. Colloid Interf. Sci.* 140.2 (1990), pp. 419–427.

[82] J. W. Wu and R. C. Flagan. *J. Colloid Interf. Sci.* 123.2 (1988), pp. 339–352.

[83] S. E. Pratsinis. *J. Colloid Interf. Sci.* 124.2 (1988), pp. 416–427.

[84] A. Bensberg, P. Roth, R. Brink, and H. Lange. *AIChE J.* 45.10 (1999), pp. 2097–2107.

[85] K. E. J. Lehtinen and M. R. Zachariah. *J. Colloid Interf. Sci.* 242.2 (2001), pp. 314–318.

[86] F. Gelbard, Y. Tambour, and J. H. Seinfeld. *J. Colloid Interf. Sci.* 76.2 (1980), pp. 541–556.

[87] P. E. Wagner. *Int. Conf. Colloid. Surf.* 2.10 (1976).

[88] Y. Xiong and S. E. Pratsinis. *J. Aerosol Sci.* 24.3 (1993), pp. 283–300.

[89] M. K. Akhtar, Y. Xiong, and S. E. Pratsinis. *AIChE J.* 37.10 (1991), pp. 1561–1570.

[90] S. E. Pratsinis and P. T. Spicer. *Chem. Eng. Sci.* 53.10 (1998), pp. 1861–1868.

[91] I. Wlokas, A. Faccinetto, B. Tribalet, C. Schulz, and A. Kempf. *Int. J. Chem. Kinet.* 45.8 (2013), pp. 487–498.

[92] M. C. Heine and S. E. Pratsinis. *J. Aerosol Sci.* 38.1 (2007), pp. 17–38.

[93] J. I. Jeong and M. Choi. *J. Aerosol Sci.* 32.5 (2001), pp. 565–582.

[94] A. Schild, A. Gutsch, H. Mühlenweg, and S. E. Pratsinis. *J. Nanopart. Res.* 1.2 (1999), pp. 305–315.

[95] A. J. Gröhn, S. E. Pratsinis, and K. Wegner. *Chem. Eng. J.* 191 (2012), pp. 491–502.

[96] C. Weise. PhD thesis. University of Duisburg-Essen, Nov. 2015.

[97] S. Tsantilis and S. E. Pratsinis. *Langmuir* 20.14 (2004), pp. 5933–5939.

[98] A. Kowalik and P. Roth. *Shock Waves* (2005), pp. 633–638.

[99] J. H. Ferziger and M. Peric. *Computational Methods for Fluid Dynamics*. 3rd ed. Springer Verlag, 2002.

[100] A. Harten. *J. Comput. Phys.* 49.3 (1983), pp. 357–393.

[101] B. P. Leonard. *Int. J. Num. Meth. Fluids* 8.10 (1988), pp. 1291–1318.

[102] P. H. Gaskell and A. K. C Lau. *Int. J. Num. Meth. Fluids* 8.6 (1988), pp. 617–641.

[103] P. K. Sweby. *SIAM J. Numer. Anal.* 21.5 (1984), pp. 995–1011.

[104] H. Jasak. PhD thesis. Imperial College of Science, Technology and Medicine, 1996.

[105] B. Van Leer. *J. Comp. Phys.* 14.4 (1974), pp. 361–370.

[106] P. L. Roe. *Ann. Rev. Fluid Mech.* 18.1 (1986), pp. 337–365.

[107] J. P. Boris and D. L. Book. *J. Comput. Phys.* 11.1 (1973), pp. 38–69.

[108] B. Cockburn, C. W. Shu, C.s Johnson, and E. Tadmor. *Advanced numerical approximation of nonlinear hyperbolic equations*. Springer, 1998.

[109] H. Rusche. PhD thesis. Imperial College London (University of London), 2003.

[110] S. Patankar. *Numerical heat transfer and fluid flow*. CRC Press, 1980.

[111] R. I. Issa. *J. Comput. Phys.* 62 (1986), pp. 40–65.

[112] C. I. Christov and R. S. Marinova. *J. Comput. Technol.* 6.4 (2001), pp. 92–119.

[113] K. H. Karlsen, K. A. Lie, J. R. Natvig, H. F. Nordhaug, and H. K. Dahle. *J. Comput. Phys.* 173.2 (2001), pp. 636–663.

[114] P. Csomós and I. Faragó. *Math. Comput. Model.* 48.7 (2008), pp. 1090–1106.

[115] E. Hairer and G. Wanner. *J. Comput. Appl. Math.* 111.1 (1999), pp. 93–111.

[116] G. Strang. *SIAM J. Numer. Anal.* 5.3 (1968), pp. 506–517.

[117] G. I. Marchuk. *Methods of splitting*. Nauka, Moscow, 1988.

[118] V. Novaresio, M. Garcìa-Camprubì, S. Izquierdo, P. Asinari, and N. Fueyo. *Comput. Phys. Commun.* 183 (2012), pp. 125–146.

[119] D. Goodwin. *Cantera: An object-oriented software toolkit for chemical kinetics, thermodynamics, and transport processes*. `http://code.google.com/p/cantera`. 2009.

[120] P. T. Spicer, O. Chaoul, S. Tsantilis, and S. E. Pratsinis. *J. Aerosol Sci.* 33.1 (2002), pp. 17–34.

[121] M. P. Burke, M. Chaos, Y. Ju, F. L. Dryer, and S. J. Klippenstein. *Int. J. Chem. Kinet.* 44.7 (2012), pp. 444–474.

[122] M. O'Conaire, H. J. Curran, J. M. Simmie, W. J. Pitz, and C. K. Westbrook. *Int. J. Chem. Kin.* 36.1 (2004), pp. 603–622.

[123] G. P. Smith, D. M. Golden, M. Frenklach, N. M. Moriarty, B. Eiteneer, Goldenberg M., C. T. Bowman, R. K. Hanson, S. Song, W. C. Gardiner, Jr., V. V. Lissianski, and Z. Qin. *GRI-MECH 3.0*. `http://www.me.berkeley.edu/gri_mech`. 2012.

[124] M. Frenklach and A. Kazakov. *Reduced Reaction Sets based on GRI-Mech 1.2*.

[125] V. V. Toro, A. V. Mokhov, H. B. Levinsky, and M. D. Smooke. *Proc. Combust. Inst.* 30.1 (2005), pp. 485–492.

[126] A. N. Hayhurst and N. R. Telford. *Proc. Roy. Soc. Lond. A* 322.1551 (1971), pp. 483–507.

[127] J. C. Biordi, C. P. Lazzara, and J. F. Papp. *Combust. Flame* 23.1 (1974), pp. 73–82.

[128] A. N. Hayhurst and D. B. Kittelson. *Combust. Flame* 28 (1977), pp. 137–143.

[129] A. N. Hayhurst, J. M. Goodings, and S. G. Taylor. *Combust. Flame* 161 (2014), pp. 3249–3262.

[130] N. A. Burdett and A. N. Hayhurst. *J. Chem. Soc. Faraday Trans I* 78 (1982), pp. 2997–3007.

[131] N. A. Burdett and A. N. Hayhurst. *Proc. Roy. Soc. Lond. A* 355 (1977), pp. 377–405.

[132] A. N. Hayhurst and S. G. Taylor. *Phys. Chem. Chem. Phys.* 4 (2002), pp. 561–570.

[133] N. A. Burdett and A. N. Hayhurst. *Combust. Flame* 34 (1979), pp. 119–134.

[134] A. N. Hayhurst, D. B. Kittelson, and N. R. Telford. *Combust. Flame* 28 (1977), pp. 123–135.

[135] P. Rosen. Silver Spring MD Applied Physics Lab., 1954.

[136] O. I. Smith. *Combust. Flame* 40 (1981), pp. 187–199.

[137] A. C. Yi and E. L. Knuth. *Combust. Flame* 63.3 (1986), pp. 369–379.

[138] O. P. Korobeinichev, A. G. Tereshchenko, I. D. Emelyanov, A. L. Rudnitskii, S. Yu. Fedorov, L. V. Kuibida, and V. V. Lotov. *Combust. Explos. Shock Waves* 21.5 (1985), pp. 524–530.

[139] U. Struckmeier, P. Oßwald, T. Kasper, L. Böhling, M. Heusing, M. Köhler, A. Brockhinke, and K. Kohse-Hoeinghaus. *Z. Phys. Chem.* 223 (2009), pp. 503–537.

[140] P. A. Skovorodko, A. G. Tereshchenko, O. P. Korobeinichev, D. A. Knyazkov, and A. G. Shmakov. *Combust. Theor. Model.* 17 (2012), pp. 1–24.

[141] A. M. Kempf, H. Forkel, J. Y. Chen, A. Sadiki, and J. Janicka. *Proc. Combust. Inst.* 28 (2000), pp. 35–40.

[142] O. T. Stein, B. Böhm, A. Dreizler, and A. M. Kempf. *Flow Turbul. Combust.* 87 (2011), pp. 425–447.

[143] M. Rieth, F. Proch, O. T. Stein, M. W. A. Pettit, and A. Kempf. *Comput. Fluids* 99 (2014), pp. 172–181.

[144] L. M. T. Somers and L. P. H. DeGoey. *Combust. Sci. Technol.* 108.1-3 (1995), pp. 121–132.

[145] K. J. Bosschaart and L. P. H. De Goey. *Combust. Flame* 132.1 (2003), pp. 170–180.

[146] A. A. Konnov, R. Riemeijer, V. N. Kornilov, and L. P. H. de Goey. *Exp. Therm. Fluid Sci.* 47 (2013), pp. 213–223.

[147] O. P. Korobeinichev, A. G. Shmakov, I. V. Rybitskaya, T. A. Bolshova, A. A. Chernov, D. A. Knyazkov, and A. A. Konnov. *Kinet. Catal.* 50.2 (2009), pp. 156–161.

[148] D. A. Knyazkov, O. P. Korobeinichev, A. G. Shmakov, I. V. Rybitskaya, T. A. Bolshova, A. A. Chernov, and A. A. Konnov. Proc. European Combust. Meeting, 2009.

[149] C. Weise, A. Faccinetto, S. Kluge, T. Kasper, H. Wiggers, C. Schulz, I. Wlokas, and A. Kempf. *Combust. Theor. Model.* 17.3 (2013), pp. 504–521.

[150] A. H. Lu, E. L. Salabas, and F. Schüth. *Angew. Chem., Int. Ed.* 46.8 (2007), pp. 1222–1244.

[151] H. K. Kammler, L Mädler, and S. E. Pratsinis. *Chem. Eng. Technol.* 24.6 (2001), pp. 583–596.

[152] S. E. Pratsinis. *Prog. Energ. Combust.* 24.3 (1998), pp. 197–219.

[153] C. Janzen and P. Roth. *Combust. Flame* 125.3 (2001), pp. 1150–1161.

[154] M. R. Zachariah, M. I. Aquino, R. D. Shull, and E. B. Steel. *Nanostruct. Mater.* 5.4 (1995), pp. 383–392.

[155] K. Buyukhatipoglu and A. M. Clyne. *J. Nanopart. Res.* 12.4 (2010), pp. 1495–1508.

[156] B. M. Kumfer, K. Shinoda, J. Balachandran, and I. M. Kennedy. *J. Aerosol Sci.* 41.3 (2010), pp. 257–265.

[157] O. M. Feroughi, S. Hardt, I. Wlokas, T. Hülser, H. Wiggers, T. Dreier, and C. Schulz. *Proc. Combust. Inst.* 35.2 (2015), pp. 2299–2306.

[158] J. Z. Wen, C. F. Goldsmith, R. W. Ashcraft, and W. H. Green. *J. Phys. Chem. C* 111.15 (2007), pp. 5677–5688.

[159] J. Camacho, C. Liu, C. Gu, H. Lin, Z. Huang, Q. Tang, X. You, C. Saggese, Y. Li, H. Jung, L. Deng, I. Wlokas, and H. Wang. *Combust. Flame* 162.10 (2015), pp. 3810–3822.

[160] J. Camacho, S. Lieb, and H. Wang. *Proc. Combust. Inst.* 34.1 (2013), pp. 1853–1860.

[161] A. D. Abid, J. Camacho, D. A. Sheen, and H. Wang. *Combust. Flame* 156.10 (2009), pp. 1862–1870.

[162] E. D. Tolmachoff, A. D. Abid, D. J. Phares, C. S. Campbell, and H. Wang. *Proc. of the Combust. Inst.* 32.2 (2009), pp. 1839–1845.

[163] A. E. Lutz, R. J. Kee, J. F. Grcar, and F. M. Rupley. *OPPDIF: A Fortran program for computing opposed-flow diffusion flames*. Tech. rep. Sandia National Labs., Livermore, CA (United States), 1997.

[164] C. R. Shaddix. *Correcting thermocouple measurements for radiation loss: a critical review*. Tech. rep. Sandia National Labs., Livermore, CA (US), 1999.

[165] R. E. Walkup and S. I. Raider. *Appl. Phys. Lett.* 53.10 (1988), pp. 888–890.

[166] P. van de Weijer and B. H. Zwerver. *Chem. Phys. Lett.* 163.1 (1989), pp. 48–54.

[167] A. J. Hynes. *Chem. Phys. Lett.* 181.2-3 (1991), pp. 237–244.

[168] D. G. Goodwin, D. L. Capewell, and P. H. Paul. *MRS Proc.* Vol. 388. 1995, pp. 33–39.

[169] I. Drira, A. Spielfiedel, S. Edwards, and N. Feautrier. *J. Quant. Spectrosc. Ra.* 60.1 (1998), pp. 1–8.

[170] R. W. Field, A. Lagerqvist, and I. Renhorn. *J. Chem. Phys.* 66.2 (1977), pp. 868–869.

[171] S. R. Langhoff and J. O. Arnold. *J. Chem. Phys.* 70.2 (1979), pp. 852–863.

[172] N. G. Glumac. *Combust. Flame* 124.4 (2001), pp. 702–711.

[173] P. Roth. *Proc. Combust. Inst.* 31.2 (2007), pp. 1773–1788.

[174] H. Cremer. *Chemie-Ing.Technik* 44.1-2 (1972), pp. 8–15.

[175] G. T. Linteris and V. I. Babushok. *Proc. Combust. Inst.* 32.2 (2009), pp. 2535–2542.

[176] A. Fomin, M. Poliak, I. Rahinov, V. Tsionsky, and S. Cheskis. *Combust. Flame* 160.10 (2013), pp. 2131–2140.

[177] H. Wang, X. Q. You, A. V. Joshi, S. G. Davis, A. Laskin, F. Egolfopoulos, and C. K. Law. *USC Mech Version II. High-Temperature Combustion Reaction Model of H2/CO/C1-C4 Compounds*. `http://ignis.usc.edu/USC_Mech_II.htm`. 2007.

[178] Z. Luo, C. S. Yoo, E. S. Richardson, J. H. Chen, C. K. Law, and T. Lu. *Combust. Flame* 159.1 (2012), pp. 265–274.

[179] R. J. Kee, J. Warnatz, and J. A. Miller. *NTIS, Springfield* (1983).

[180] T. A. Miller, M. S. Wooldridge, and J. W. Bozzelli. *Combust. flame* 137.1 (2004), pp. 73–92.

[181] J. Li, Z. Zhao, A. Kazakov, M. Chaos, F. L. Dryer, and J. J. Scire. *Int. J. Chem. Kin.* 39.3 (2007), pp. 109–136.

[182] M. R. Zachariah and D. R. F. Burgess. *J. Aerosol Sci.* 25.3 (1994), pp. 487–497.

[183] S. L. Chung and J. L. Katz. *Combust. Flame* 61.3 (1985), pp. 271–284.